PHD

MODELLING ASPHALTENE FOULING IN CRUDE OIL PROCESSES

Hamed, Mohamed

Award date:
2021

Awarding institution:
University of Bath

MODELLING ASPHALTENE FOULING IN CRUDE OIL PROCESSES

Mohamed Abdelrahman Hamed

A thesis submitted for the degree of Doctor of Philosophy

University of Bath

Department of Chemical Engineering

2020

Declaration of Authorship

I am the author of this thesis, and the work described therein was carried out by myself personally except where I have indicated via references or other forms of acknowledgement.

Signature:

Date:

ABSTRACT

Fouling is a long-standing technical and economical challenge for processing industries. At the very least, surface fouling reduces thermal efficiency, increases usage of fuel, and increases the emissions of carbon dioxide. There are many existing techniques for dealing with the fouling problem. On the other hand, there is limited information about the fouling techniques, and limited ways of predicting the crude oil fouling phenomena mathematically.

There are lots of research suggesting different techniques and mechanisms that provide good explanation to the fouling phenomena. However, these mechanisms have their limitations such as limited amount of data to support these mechanisms. A numerical model which used a combination of fouling threshold modeling and computational fluid dynamics, were used in this thesis to predict the fouling correctly. The fouling threshold model combines both fouling deposition and removal factors where the deposition depends on the operation condition and fluid properties while the removal depends on system shear rate.

A huge task was conducted before model application which was crude oil and asphaltenes foulant properties estimation as function of temperature and pressure. Based on the accuracy of properties estimation the model can succeed.

The model was tested using two sets of data. The first set contained fouling rates from the Exxon mobile works of Ebert and Panchal. The second set contained fouling deposition thickness and heat exchanger cleaning schedule from a local refinery in the state of Kuwait. The results showed that the combined numerical model explained the fouling satisfactory in terms of fouling thickness and fouling rates hence it was used to reproduce these data sets successfully as well as providing

extra information about the temperature and velocity profile, and most importantly fouling thickness profiles along the length of tube side in the heat exchanger.

It remains necessary for research and test experiments to be carried out so that mathematical models of the fouling process can be formulated. In this way, it is possible to find out how fouling affects an individual heat exchanger and hence the network in which it resides.

Acknowledgments

I would like to express my sincere gratitude to my thesis supervisors Prof. John Chew, Prof. Semali Perera, and Prof. Barry Crittenden for their supervision, support, and encouragement.

The author is indebted to the contributions from the Research Administration General facilities Kuwait University who provided the funding necessary to carry out part of this work. This work was funded and supported by the Research Administration of Kuwait University under Projects GE01/07 and GE02/08. The authors would also like to acknowledge Project no. PE 02/08, from where some of the viscosity data were used. General facility science projects GS01/01 and GS01/03 for asphaltene characterization, general facility engineering project GE03/08 for asphaltene onset tests.

I wish to acknowledge the assistance and daily supervision of Dr Osama Al-Omair and Dr. Amal Elkilani (Kuwait University-Petroleum and Chemical Engineering Departments, respectively).

I would like to thank my wife, Afrah, and daughter, Khadija, for their support and patience while I conducted this research. And my father, my brother, and my sister in law for always pushing me and believing in me.

Nomenclature

Roman

$\frac{dR_f}{dt}$	Fouling rate	$m^2.K.w^{-1}.hr^{-1}$
Cp	*H*eat capacity	$j.kg^{-1}.K^{-1}$
D_a	Asphaltenes diffusivity in the bulk	$m^2.s^{-1}$
G	Reciprocal wall distance	m^{-1}
I	Turbulent intensity	
J_a	Asphaltene diffusive mass flux	$kg.m^{-2}.s^{-1}$
k	Turbulent Kinetic energy	$m^2.s^{-1}$ or $j.kg^{-1}$
k_a	Thermal conductivity of asphaltenes	$w.m^{-1}.K^{-1}$
M	Molecular weight	
N_a	Asphaltene mass flux	$kg.m^{-2}.s^{-1}$
P	Pressure	pa
P_c	Critical pressure	pa
Q	Heat input	$j.s^{-1}$
r	Cylindrical coordinates distance from the axis	m
R_a	Asphaltenes disappearance from bulk reaction rate	$kg.m^{-3}.s^{-1}$
R_g	Universal gas constant	$j.mol^{-1}.K^{-1}$
SG	Specific gravity	
T	Time	s
T	Temperature	C
T_c	*C*ritical temperature	K
U	Bulk velocity	$m.s^{-1}$
x_a	Asphaltenes mass fraction	
z	Cylindrical coordinates axis	m

Greek

Θ	Covered surface fraction	
ρ	Density	$kg.m^{-3}$
∇	Gradient	m^{-1}

θ	Cylindrical coordinates between the axis and the line segment	M
τ	Sheer stress	pa
μ	Dynamic viscosity	pa.s
ω	Dissipation Rate	s^{-1}
β_0^*	Turbulent model constant	
σ	Turbulent transport coefficient	
ε	Error	

Acronyms

ACO	Asphaltene-coacervation onset
AEAE	2-(2-amino-ethylamino) ethanol
AEoS	association equation of state
AMO	Asphaltene-micellization onset
ANN	Artificial Neural Network
APO	Asphaltene precipitation onset
ARDO	Asphaltene and resin-deposition onset
ARFO	Asphaltene and resin-flocculation onset
ASTM	American Society for Testing and Materials
BPD	barrels per day
C:H	carbon to hydrogen ratio
CDU	crude distillation unit
CENPES	Petrobras R&D Center
CFD	Computational Fluid Dynamics
CPA	cubic-plus-association
CPT	crude to preheat train
DA	duelist algorithm
DBSA	dodecyl benzene sulfonic acid
DO	deasphalted oil
DR	dodecyl resorcinol
EORC	Eagle Oil Refining Company
EoS	equations of state
FDG	fluid dynamic gauging

GA	genetic algorithms
GC	gas chromatography
GDP	gross domestic product
HEN	heat exchanger network
HPLC	high-performance liquid chromatography
ICA	imperialist competitive algorithm
IR	infrared spectroscopy
KNPC	Kuwait National petroleum company
MDF	multifunctional development factor
MINLP	Mixed-Integer Nonlinear Programming
MS	mass spectrometry
MSE	mean square error
NMR	nuclear magnetic resonance
NP	Nonylphenol
PDPF	post desalter and pre-flash drum
PHT	Pre-heat train
PIBSA	poly-iso-butenyl succinic anhydride
PR	Peng Robinson equations of state
PSO	particle swarm optimization
PVT	Pressure volume and temperature
SARA	saturates, aromatics, resins, and asphaltenes
SCP	Saturates-cloud point
SPP	Saturates-pour point
SRK	Soave-Redlich-Kwong equation of state
TLC	thin layer chromatography
USSR	Union of Soviet Socialist Republics
UV	Ultraviolet
VLE	Vapor-liquid equilibrium
PEMEX	Petróleos Mexicanos
EOR	Enhanced Oil Recovery
API	American Petroleum Institute

TBP	True Boiling Point
THF	Tetrahydrofuran
GPC	Gel Permeation Chromatography
MAPE	Mean absolute percentage error
SD	standard deviation
MAA	Mina Al-Ahmadi

\

Table of Contents

List of Figures

List of Tables

Chapter 1: Introduction

The increasing demand for energy opened the market for heavy crude oil, which is not popular among environmentalists, socialists, and policy makers. Heavy crudes contain small amounts of light cuts such as gases, gasoline, and kerosene; on the other hand, they are rich in atmospheric and vacuum residues. The two cuts require complicated upgrading processes to be able to generate commercially useful products [1]. Although heavy hydrocarbons have higher energy output during the combustion process. Processing of heavy crude oil is technically and economically challenging due to various reasons, such as high density and high viscosity, which increase the pumping power required for the process and the larger heat capacities which require more energy to heat the crude. Figure 1.1 shows the main process in a typical petroleum refining facility. The major issue in any chemical process is the energy demand. Some of the required energy is demanded for the pumping process or utility fluids. The major part of the energy demanded is for heating the process fluid in heat exchangers, such as the pre-heating train, in order to reach the required process temperature. The major issue in heat exchanger and other process flow systems is the accumulation of unwanted materials on solid surfaces. This accumulation process is called the fouling process.

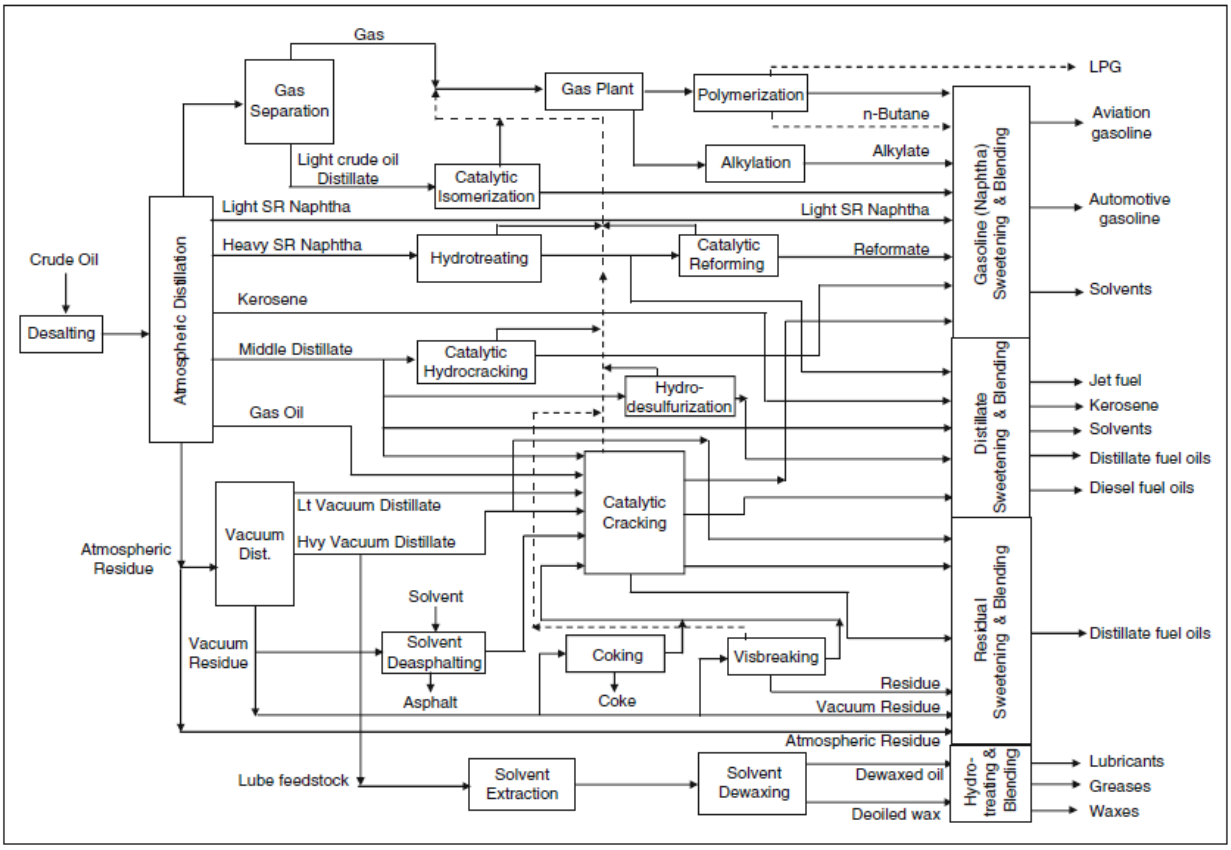

Figure 1.1: The Modern Refinery [1].

Fouling occurs in many petroleum processes such as drilling, completion, acid stimulation, and hydraulic fracturing activities can also induce precipitation in the near-wellbore region, heat exchanger, fractionations, etc. The fouling process is a significant issue in the processing of heavy crude oils, especially the ones that contain a high amount of foulants such as asphaltenes, resins, and waxes. It occurs due to many reasons such as pressure, temperature, and composition changes. The most important factors for improvement of the oil-recovery processes are a pressure drop and the mixing of oil with additives [2]. This research focuses on asphaltene precipitation during the pre-heating stage for crude oil before it is fed to the petroleum refinery. Modeling of asphaltene fouling is the ultimate goal of this thesis, to apply it for oil blends to hinder fouling during refinery processes.

1.1 Concern

With technology moving forward in the treatment of heavy and extra heavy crudes, a better understanding of this phenomenon is in great need. It is reported that asphaltene is the primary precipitate in crude oil processes and hence the main component of fouling. The cost of fouling in refineries of industrialized courtiers has been estimated at around $1.3 billion per year [3]. This cost is mainly to recover the heat loses by injecting more fuel in pre-heater and loses in production hours due to shutdowns and cleaning/maintenance of the pre-heaters.

1.2 Problem Statement

Fouling is a tough technical and economic challenge for processing industries. At the very least, surface fouling reduces thermal efficiency and increases the use of fuel, which increases the emissions of carbon dioxide. There are many existing techniques for dealing with this problem. These techniques range from the usage of chemicals or mechanical devices, the modification of operating conditions, and retrofitting heat exchangers such that fouling is prevented from starting. Since each processing application is different, it remains necessary for research and test experiments to be carried out so that mathematical models of the fouling process can be formulated. In this way, it is possible to find out how fouling affects an individual heat exchanger and hence the network in which it resides.

1.3 Importance of Modeling and Simulation

In this research, a “model” uses a mathematical representation for a real object, process, or phenomenon. It helps to understand the behavior of what is represented. On the other hand, simulation applies the mathematical model (or in some cases a computer model such as neural networks) to describe the system based on different sets of inputs. Modeling and simulation are a

simplified representation of reality. The process of modeling and simulation is needed because it is difficult or not feasible to perform experimental work on some systems, due to many factors such as high temperature and pressure. In addition, sometimes this kind of data does not accurately predict any operation outside the boundaries of the data through extrapolation or also interpolating among the data. In the study targeted by this thesis, a material/species balance is one of the significant parts of the model. It is challenging to check for asphaltene concentration in every stage in the heating process and at different location of the process. The same problem applies to momentum and energy/heat balance, which will provide velocity and temperature profiles, respectively.

The model will help in the process of repetitive computations with different sets of inputs (operation conditions and feed properties). The model can be adjusted to simulate the dynamic portions of the system such as startup, shutdown, and change in operating conditions. Modeling helps to generate data points for different scenarios without the need to do extra experimental work. The process of successful modeling must contain some assumptions. These assumptions must be made carefully to avoid inaccuracy. With minimal assumptions and careful selection, the inaccuracies will be within an acceptable range.

Heat exchangers are the workhorses of most chemical, petrochemical, food processing, and power generating processes. The size of the heat exchanger market was approximately a total of $12.7 billion in 2012, with an increase of 3-5% annually [4]. This huge size puts manufacturers under increasing pressure to produce heat exchangers that are more efficient in heat recovery and use of material, while at the same time being faced with fluids that are increasingly difficult to process. One significant problem directly related to these requirements is the deposition of unwanted materials on the heat transfer surfaces. This is known as the fouling of heat exchangers [5, 6].

Conservative studies have estimated that heat exchanger fouling leads to additional costs in industrialized countries in the order of 0.25% of gross domestic product (GDP), as well as causing around 2.5% of the total equivalent anthropogenic emissions of carbon dioxide [7, 8].

1.4 Limitations

The major problem with asphaltene is that it is not a component with known chemical composition and physical properties. Asphaltene is a set of different complicated hydrocarbons found with a high concentration in the heavy cuts of the crude oils. For this reason, it is tough to work on asphaltene in the laboratory, in mathematical modeling or computer modeling. Asphaltenes consist primarily of carbon, hydrogen, nitrogen, oxygen, and sulfur, as well as trace amounts of vanadium and nickel. The carbon to hydrogen ratio (C:H) is approximately 1:1.2, depending on the asphaltene source [9]. These combinations of different chemical compositions will not give constant properties but instead will provide a range of properties. Moreover, the process of modeling and simulation will offer a range of outputs such as the rate of asphaltene fouling and fouling thickness progression over time.

1.5 Aim and Objectives

This thesis study aims to generate a model that can describe and simulate the precipitation of asphaltenes in the pre-heaters of crude oil distillation units. The model it can be used to predict the asphaltene precipitation for a specific set of operating conditions. The model can simulate different processes and predict the fouling rates while changing feed streams to reach a set of properties such as specific gravity, viscosity and if possible chemical composition by mixing different feed sources. This will help predict the physical fouling and optimize the periods between pre-heaters shutdowns for maintenance and cleaning.

To fulfill the above objectives of this work, the following sub-objective steps are followed:

1. Elaborate and update literature review to pinpoint the gaps in modeling asphaltene fouling
2. Collect experimental data for various crudes with measured physical properties
3. Estimate the required properties that are needed in modeling and not available for the crudes under study
4. Generate and test the asphaltene modeling and highlight the limitations
5. Apply and solve the proposed model in this work on a typical case
6. Test the proposed model on a real plant case.

1.6 Structure of Thesis

As a conclusion of the above section, this thesis will contain six chapters. The first chapter is this introductory chapter. The second chapter will list the research literature that focuses on the area of asphaltene fouling in processes and how they are dealt with. The third chapter is the main chapter which will describe the mathematical model, the boundary conditions, and the package used to solve it. The fourth chapter will contain the experimental determination of crudes and asphaltene properties that will help in the modeling section. Chapter four will include generated correlations for available and unavailable properties, at various operating conditions, of the crudes under study for the sake of model application. The fifth chapter shows the output of the model. The main output is the fouling rate of asphaltene in crude at inside the process. After the success of the model's solution of a problem in a pilot heat exchanger, the model will be applied in a real case in a refinery. The last chapter, chapter six, will present conclusions and recommendations and ideas for potential future researches.

Chapter 2: Literature Review

The primary purpose of this thesis is to study the complicated physical phenomena of asphaltenes. In this chapter, previous research on this topic will be discussed, summarized, and reviewed. The first part of this chapter focuses research conducted to describe the chemical structure of asphaltenes. The second part discusses how researchers decided to model the phenomenon of asphaltenes fouling or fouling in crude oil in general. The second part will categorize and separate the modeling techniques and list the strong points significant weakness of each model.

2.1 Asphaltene in Crude Oil and Characterizations

A variety of substances of diverse chemical natures are mixed together in nature to create what is known as the petroleum fluids. These substances include paraffinic, naphthenic, and aromatic hydrocarbons and polar poly-aromatic materials that contain nitrogen, oxygen, and sulfur. Crude oil is a mixture of all these compounds, and its concentration varies according to the source. Thus, some crude oils have higher proportions of the lower-boiling substances, whereas others have higher percentages of the heavy, polar, nonvolatile end of the crude, referred to as asphaltene and resin [2].

Asphaltene is lyophilic for aromatics, in which they form highly scattered colloidal solutions. Specifically, asphaltenes of low molecular weight are lyophobic for paraffin like pentanes and petroleum crudes. A considerable number of researchers have worked on the characterization of asphaltene. Asphaltene is composed of carbon, hydrogen, nitrogen, oxygen, and sulfur, as well as trace amounts of metals such as vanadium and nickel. The carbon to hydrogen (C:H) ratio is approximately 1 to 1.2, depending on its source. One of the common descriptions of asphaltene is

the n-heptane (C_7H_{16})-insoluble, toluene ($C_6H_5CH_3$)-soluble. Asphaltene has a molecular weight that ranges from 400 to 1500, but the average and maximum values are difficult to determine due to the aggregation of the molecules in solution [9].

The primary challenge of researching asphaltene is the lack of information about its nature and behavior. This lack of knowledge is due to the complicated chemical structure of this component. Another problem is the adsorption of some other materials on the asphaltene and the inability to separate those materials, for example, polar resins. These complications lead to limited knowledge of asphaltenes' physical and chemical properties.

Evdokimov [10] applied bifurcated correlations of the properties on data from recovered crude oil at very low pressure with no gas content (dead oil) samples from the database of the oil of the former Union of Soviet Socialist Republics (USSR), as well as published data by other authors. The use of dead-oil (unpressurized/gas free crude oil) was due to the difficulties in sampling and analyzing the live-oils (pressurized/gas-rich crude oil) in reservoirs or the lab. The data obtained from dead oil, however, can be of great benefit. These data were tested using asphaltene-based correlations to estimate crude oil properties such as densities, viscosities and pour points. The relation between those properties and the asphaltene content was far away from a linear relationship. Some "persistent anomalous deviations" of the physical properties were found with a sample that had asphaltene content in the range of 2 - 2.5 weight%. Evdokimov's study [10] suggested that there are two types of crude oil in the world. The bifurcated correlations with asphaltenes also were observed for saturates, aromatics, and resins and for sulfur, vanadium, and nickel. The relationships show definite traces of biodegradation and source types. However, a review of various oil-alteration processes shows that an apparent subdivision of crudes into two classes is most probably due to deasphalting via a natural geo-chromatography of oils in the course

of migration, resulting in selective removal of a well-defined polar asphaltene fraction, distinguished by its low solubility.

Roenningsen and Skjevrak [11] used the SARA (saturates, aromatics, resins, and asphaltenes) analysis and UV absorbance chromatograms concepts to categorize the crude oil components into four groups based on differences in solubility and polarity. Knowledge of correlations of crude oil's properties with these major chemical groups is integral to both upstream and downstream operations. This knowledge was beneficial in studies related to reservoir evaluation, migration and maturity, degradation processes, processing, and environmental effects.

Silva et al. [12] presented state of the art research in the characterization of heavy crude oil mixtures. The characterization can be done by different techniques, such as gas chromatography (GC), high-performance liquid chromatography (HPLC), thin layer chromatography (TLC), infrared spectroscopy (IR), Raman spectroscopy, nuclear magnetic resonance (NMR) spectroscopy and mass spectrometry (MS). Nuclear magnetic resonance spectroscopy is the technique of choice due to its capability to provide information on the chemical nature of individual types of hydrogen and carbon atoms in different and complex mixtures of crude oils. The progress made in the interpretation of the NMR spectra with the development of new NMR techniques and separate multivariate data analyses could give relevant information about the identification and characterization of hydrocarbons and their physical and chemical properties. These signs of progress can improve the refining industries operation as a result of the better knowledge of the crude composition that is fed into the refining process, as well as in the prediction of better-operating conditions to obtain refined products with desired specifications and in quantities desirable for meeting the market demands. The improvement in the refining operation conditions is reflected in economic benefits.

Al-Sahhaf et al. tested the use of simple additives such as deasphalted oil (DO) or resin (R) which were obtained from Kuwaiti crude to obstruct the asphaltene precipitation from such crude when n-heptane is added [13]. The obstructing effect of toluene (T) and selected surfactants (substances which tend to reduce the surface tension of a liquid in which they are dissolved) was also tested. The surfactants tested were nonylphenol (NP), dodecyl benzene sulfonic acid (DBSA), and dodecyl resorcinol (DR). The delay in asphaltene precipitation with addition of inhibitor is found to be in the order: DR > DBSA > NP > R > T > DO. These results show that simple additives such as toluene and DO and resin are not as effective as surfactants. The effect of toluene and DO is only noticeable on the delay of asphaltene precipitation when their mass fraction in the oil is more than 60%. The strong delay effect of the surfactants is explained by the interaction between the acidic part of the surfactant and the asphaltene. The mechanism of inhibition was explained regarding the micellization model of Victorov and Firoozabadi [14]. The onset point for asphaltene precipitation with n-heptane addition was measured in the presence of different amounts of inhibitor. It is possible to predict the amount of inhibitor required for reaching a certain onset point using the micellization.

Table 2.1 summarize the finding in this section about different characteristics of asphaltenes and its properties. Figure 2.1 describes a hypothetical asphaltenes molecular structure based on the findings of the literature.

Table 2.1: Summary of Asphaltene in Crude Oil and Characterizations research

Reference	Samples (Where were they obtained)	Research carried out and technique used	Main findings
Podgorski et. al [9]	A heptane-deasphalted distillate cut (523−593 °C) from a North American heavy crude oil	High-performance liquid chromatography (HPLC)	Asphaltene has a range of molecular weights from 400 to 1500
Evdokimov [10]	Recovered (dead) crudes from a new database of the oils of the former USSR[15]	Correlation based research	deviations of bulk properties in oils with 2–2.5 wt.% asphaltenes.
Roenningsen and Skjevrak [11]	North Sea Oils	SARA analysis	There was good agreement between the elution order of aromatics relative to n-alkanes on a nonpolar GC stationary phase and the boiling order during TBP distillation.
Silva et al. [12]	Multiple locations (A review paper)	Gas chromatography High performance liquid chromatography (HPLC) Thin layer chromatography (TLC) Infrared spectroscopy (IR)	NMR was chosen as the main technique to be used in crude oil refining industries that want to characterize the method that describe the crude oil fractions and the obtained refined products

		Raman spectroscopy Mass spectrometry (MS) Nuclear magnetic resonance spectroscopy (NMR)	
Al-Sahhaf et. al[13]	Kuwaiti crude	Addition of inhibitor DR, DBSA, NP, R, T, DO	The retardation of asphaltene precipitation with addition of inhibitor is found to be in the order: DR > DBSA > NP > R > T > DO

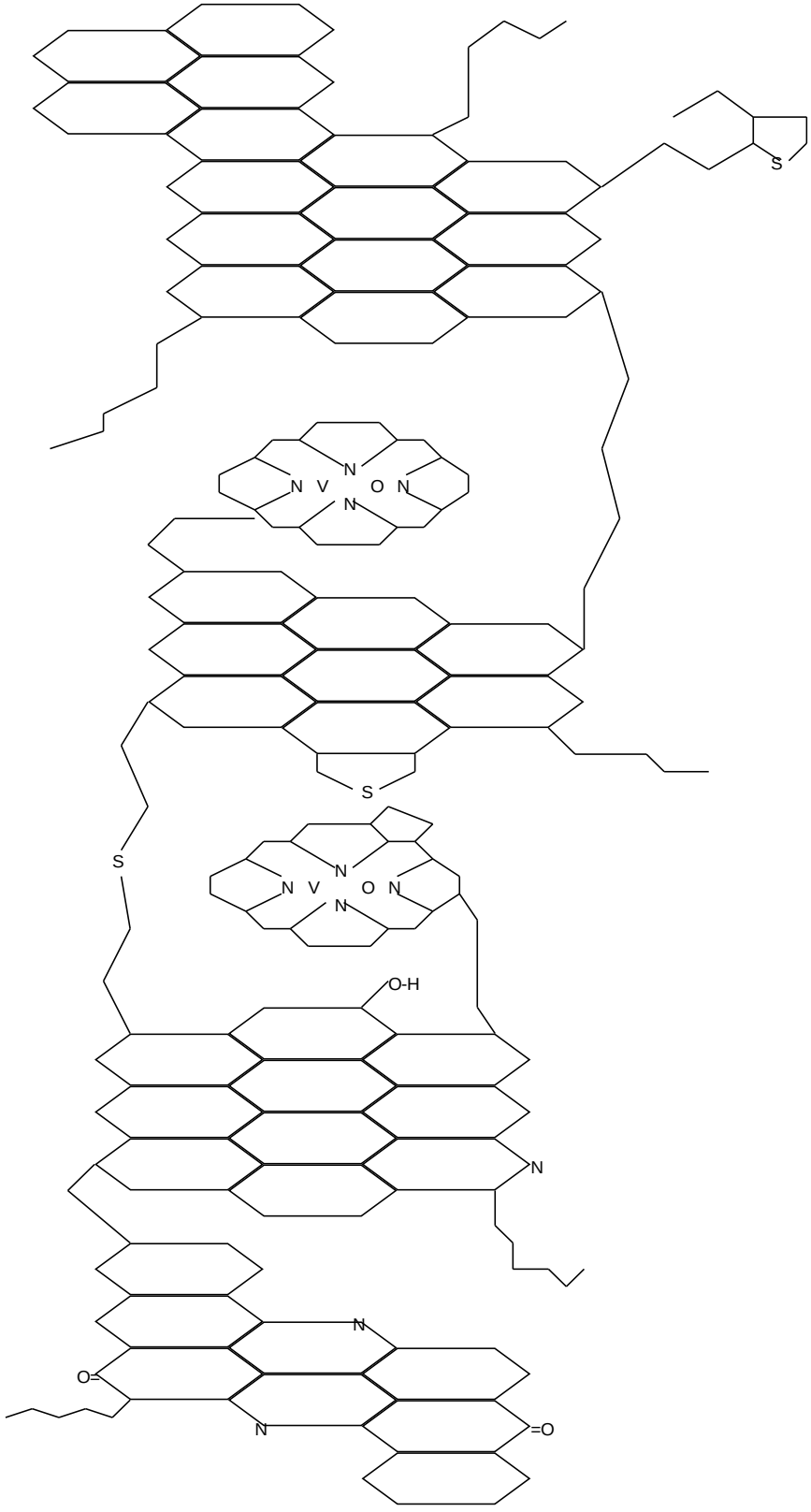

Figure 2.1: Hypothetical asphaltene molecule and its interaction with metalloporphyrins[1]

2.2 Asphaltene Fouling

The asphaltene precipitation phenomenon is wrapped in great mystery because of the lack of asphaltene precipitation data available in the literature. The occurrence of precipitation in both underground petroleum reservoirs and production facilities is undesirable. Therefore, information regarding the optimum conditions for precipitation of asphaltenes is needed to deal with this phenomenon and avoid problems of plugging in processing facilities. Because the issue of asphaltene deposition can start at any point along the crude production process where the equilibrium of the stabilizing asphaltenes has been upset, modeling can estimate the destabilizing forces that most often cause the deposition problem. Through modeling, there are many approaches to an understanding of the phenomena of fouling of asphaltenes in the crude-oil industries. Those different approaches are discussed in this section and subsections to show the advantages and disadvantages of each approach.

Asphaltene deposition in the gaseous flow is investigated to understand the problem of fouling in wellbores in oil fields and petroleum industries. The fouling problem leads to operational challenges and a decrease in production. These asphaltenes particulates are entrained in the flowing fluid from the reservoir or generated in the wellbore flow. The asphaltene precipitation is a function of pressure, temperature, and fluid composition. The presence of asphaltene in crude oil, the accurate prediction of those solid particle depositions is necessary to design production facilities and to optimize operational performance [16].

It can be assumed that there are seven different points of phase transition of the separations process of heavy organics (saturates, resins and asphaltenes) from crude oil fluids:

1. Saturates-cloud point (SCP)

2. Saturates-pour point (SPP)
3. Asphaltene precipitation onset (APO)
4. Asphaltene and resin-flocculation (colloid formation) onset (ARFO)
5. Asphaltene and resin-deposition onset (ARDO)
6. Asphaltene-micellization onset (AMO)
7. Asphaltene-coacervation onset (ACO)

The existing experiments for the determination of the onsets of asphaltene phase separations/ transitions have been analyzed by many researchers. It is clear that these point measurement techniques are helpful for various applications, and of course, they can be used to measure the onset of different phase separations due to changes in the conditions of a petroleum fluid under consideration [17].

Many other methods are proposed for determining the onsets of asphaltene phase separations/ transitions experimentally [18-22]. In general, methods for determining the onsets of asphaltene may be classified according to the procedure utilized to detect the onsets. In the following, we discuss a couple of these methods.

Measurements of electrical conductivity as a function of the precipitating agent have been proposed for the detection of the onset of asphaltene fouling [19]. By adding precipitating solvent to oil, the mobility of conducting species increases to a maximum at which the onset of asphaltene deposition occurs. These results show that the deposition of asphaltenes is strongly related to the charge transport mechanism.

The light transmission [20] method is based on the detection of changes in transmitted light intensity as a function of deposited fluffy mass formed by the aggregation of fine suspended foulant materials (a floc) concentration in the crude oil mixture.

Gravimetric analysis [21] also allows for the detection of the onset and amount of asphaltene deposition. This technique is commonly used together with visual methods to verify results obtained by measurements of electrical conductivity and light transmission. The conditions of some oils (like heavy oils and dead oils) are such that one or more of their onset points have already passed.

Shirdel et. al [16] discussed the mechanisms for solid particle deposition, including particle momentum and mass transfer as well as particle re-entrainment. Afterward, important particulate deposition models were described and compared using different sets of experimental approaches such as precipitation of iron particles in the gaseous flow. The results showed that the deposition models agreed with experimental data. They are also acceptable for predicting asphaltene precipitation in crude oils as well as other particle precipitation in gaseous flow streams. Different approaches were reviewed for fouling modeling in turbulent flows (gaseous and liquids). Two different methods were described, the standard stopping distance treatment and stochastic modeling. The consistency of the derivations of the models was checked and compared against two sets of experiments. A good agreement was reached for the conditions that the models are trained. In addition, the comparison showed that the described models are applicable for asphaltene precipitation in crude oil flows. It was also observed that increasing the flow velocity and decreasing the tubing surface temperature decrease the precipitation rate significantly [16]. From these findings, it was concluded that in the wellbore system, where velocity increases due to expansion and temperature drop due to a thermal gradient from bottom-hole to the surface, the

transport coefficient decreases remarkably. Moreover, since the relaxation time for the asphaltene particles is favorable in the Beal (1970), Escobedo and Mansoori (1995) and Cleaver and Yates (1975) [23-25] models. These models are appropriate for calculating asphaltene deposition. Furthermore, since the Beal (1970) and Escobedo and Mansoori (1995) models are more general for a wide range of relaxation times, these models are recommended for use in comprehensive wellbore asphaltene deposition modeling.

The surface roughness issue has been tackled by Herz et al.[26] Rough surfaces have a significant impact on the precipitation and the deposition of calcium sulfate on a stainless steel tube. It was showed that the fouling layer on a rough surface sticks more than on a smooth surface. It is also harder to remove and requires shorter periods between maintenance to clean the heater pipes.

Mozdianfard and Behranvand [27] investigated the effect of fouling in pre-heaters on crude distillation units in a 30-years-old oil refinery in Esfahan. Their primary objective was to study the change and behavior of the fouling in the pre-heaters with time. It was concluded that the increase in fouling heat resistance with time caused a reduction in operating pressure and an increase in the operating temperature. The most significant fouling was found in the post-desalter and pre-flash drum heat exchanger. They also studied different kinds of tubing materials that affect the fouling phenomena [27].

Figure 2.2 shows the simplified heat exchanger diagram in the Esfahan refinery. It was found that the most rapid fouling rate was observed at E-155A-B. The tube fouling had 80% mineral content including $CaSO_4$, indicative of inefficient desalter performance and possible two-phase fluid formation inside the tubes. The primary objective of installing E-251A-B to reduce ISO.F. temperature in the shell of E-155A-B had little effect on the fouling extent of these exchangers,

but improved by about 5°C the inlet temperature to the furnace. In E-155C, the last pre-desalter unit exchanger, corrosion was the primary fouling mechanism. As far as the constituent of foulant was concerned in the exchanger set of E-155A-C, organic contents were reduced as the temperature of the shell side fluid declined, while asphaltenes content was increased at the same time. The inorganic substances of crude-oil heating-fluid foulants are mainly iron oxide. The organic and asphaltenes content from the samples at the outer surfaces of tubes and the inner shell surfaces were different, suggesting that different fouling mechanisms were at work at these positions. Belmar-Beiny et al. [28] observed a much shorter induction period in a plate heat exchanger than in a tubular heat exchanger. They considered that this was due to the higher turbulence in the former. Belmar-Beiny and Fryer [29] analyzed the first layer of deposit which was thought to be formed during the induction period and found that it was made of proteinaceous materials rather than minerals. Geddert et al. [30] investigated the effects of surface coatings and attempted to correlate the induction with the surface roughness and surface tension but did not reach any quantitative conclusion.

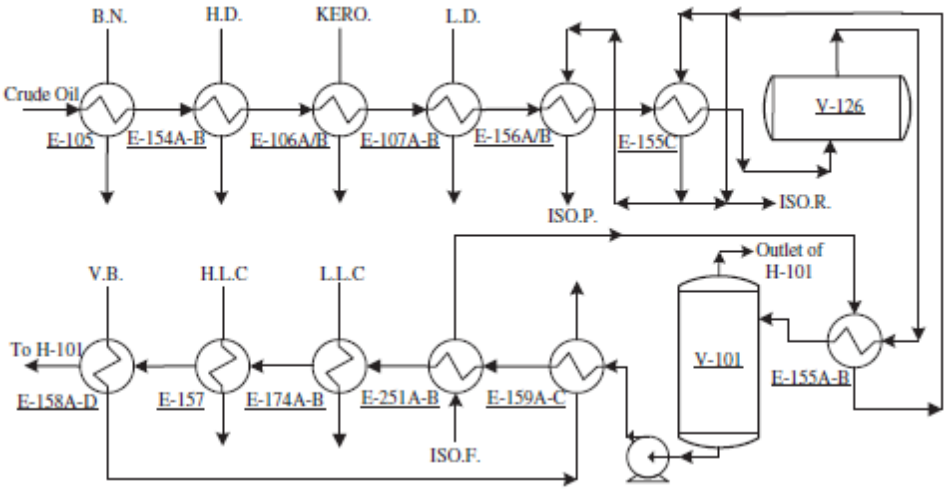

Figure 2.2: Simplified flow diagram of crude oil preheat train at Esfahan refinery. A/B and A-B stands for parallel and series arrangements of exchangers, respectively.

Augustin et al. [31] examined the effect of surface treatments on protein fouling and described the influence of wall temperature on the induction period. Despite many observations and investigations of induction phenomena, this period in a fouling process has not been studied in a substantially quantitative manner, and this is undoubtedly the case for crude oil fouling. The main reason for this can be attributed not only to the complexity of the fouling behavior in the induction period but also to the fact that no additional experimental information can be gained when the induction period occurs, since it appears as a steady state phenomenon in which no useful experimental data can be collected.

Vahdat Azad et al. [32] proposed a graphical modeling method to minimize the precipitation and increase the time needed to do the required maintenance/cleaning of heat exchanger networks (HENs). In this method the time schedules and places of replacing high fouling rate streams with those of low fouling rate are determined, thereby giving more opportunity for fouling formation to the network.

Nasr et al. [33] proposed a new model for crude oil fouling in the preheat train of crude distillation units (CDU). The experimental data of Australian light crude oil were used. The operation condition range was 200, and 260°C for the surface temperature of the tube and 0.25–0.4 m/s were used for the fluid inlet-velocity. The estimated value of energy depends on the surface temprature. A model was proposed considering fouling formation and removal in relation to chemical reaction and tube-wall shear stress. The strong aspects of this model are independent of Prandtl number and thermal fouling removal. Finally, using this model, the fouling rate of Australian light crude oil was estimated and threshold graphs were created to identify fouling and no fouling formation zones. It was revealed that among the models to predict the fouling formation, one considering

deposition and removal of the fouling layer has great importance. Fortunately, the proposed model has this advantage.

To use the model and also to calculate the activation energy, the fouling rate should be available in at least three different film temperatures. As shown, the model can predict the fouling rate for various crudes and in different conditions better than other models. By proposing a model, the threshold curves can be drawn, and a designer can identify quickly whether a heat exchanger is located in a fouling zone or not. In addition, this curve distinguishes if a heat exchanger is located in a fouling region and how it can be expelled from this zone. For instance, in Figure 2.2, a heat exchanger with tube side velocity, u = 4.25 (m/s) and T_f = 420 K, is located below the threshold curve (that is in a no-fouling zone). By increasing the film temperature to T_f = 440 K, the exchanger moves to above the threshold curve (that is in a fouling region). Now, it is necessary to increase the velocity to exit from the fouling zone.

Crude oil distillation in petroleum refineries involves a heat exchanger network to heat the crude using hot side streams and pump around. This energy integration reduces the furnace load as well as the cold utility consumption, diminishing fuel costs and carbon emissions. During the operation, the effectiveness of the heat exchangers decreases due to fouling. Preheat trains composed of multiple parallel branches were investigated through an alternative operating policy based on the optimization of stream splits, aiming to manipulate the flow rates according to the fouling status of the existent heat exchangers. The execution of the proposed approach can be illustrated by three examples: two networks from the literature and one real network from a Brazilian refinery [34].

Three examples illustrate the potential economic gains from the proposed procedure with different features:

- Example 1 involves three heat exchangers where one exchanger is clean, and the others are dirty after a long time online.
- Example 2 presents the optimization of stream splits in the context of a cleaning schedule of a train with 14 heat exchangers
- Example 3 is a crude preheat train from a Brazilian refinery composed of 35 heat exchangers distributed along five branches.

The reductions of the fraction of furnace energy requirement due to fouling in each case were 46%, 5.7%, and 12.5%, respectively. These results indicate an enormous economic benefit because of the vast quantities of crude oil processed in a refinery

It is necessary to point out that the application of the proposed procedure demands a careful analysis of the impact of the stream split optimization on fluid velocities in the heat exchangers [35]. Ishiyama et al. [36] presented an example where an unbalanced flow distribution in two heat exchangers operating in parallel implied a considerable decrease in the total heat load in the future. This problem can be handled in the proposed procedure through the insertion of constraints on the split fractions. The unconstrained nature of the optimization problem can be easily kept, through the introduction of these constraints using a penalty term in the objective function.

In relation to the refinery hardware, the proposed procedure would involve the installation of a control system in the preheat train with the capability to maintain the flow rate distribution according to the set-points related to the optimal split fractions identified. Additional analysis should also be conducted to check eventual pump power limitations.

Asphaltenes have the largest molecular weight and the most polarizable components in the crude oil mixture. The phase behavior of these kinds of components is essential in crude oil processing

because of their potential to create fouling in production equipment. Foretelling flow assurance issues caused by asphaltenes requires the ability to model their phase behavior as a function of their composition and of the temperature and pressure of the system. Panuganti et al. presented a detailed procedure to characterize crude oil and develop the asphaltenes phase diagram, through the perturbed chain form of the statistical associating fluid theory (PC-SAFT). They also demonstrated that the procedure could model the asphaltene thermodynamic phase behavior more efficiently than using a cubic equation of state that is used widely in the industry[37]. The results obtained with the proposed characterization method are very close to the experimental data for both the bubble point and asphaltene precipitation rates and onset points. A wide range of temperatures, pressures, and gas injection percentages have been tested. The concept of lower asphaltene onset pressure is also explained, and a new representation of the asphaltenes phase diagram is presented.

PC-SAFT is a highly promising equation of state (EoS) for modeling asphaltene precipitation. With this work, we have demonstrated a brief methodology to characterize crude oils using PC-SAFT EoS and subsequently modeled asphaltene phase behavior in crude oils. This EoS work describes a methodology by which several similar components can be lumped together as one fraction, thus drastically decreasing the computational expense in performing these thermodynamic calculations. PC-SAFT parameters can then be calculated for each of these fractions based on the correlations provided. A systematic methodology to implement the PC-SAFT parameter estimation is also explained, which will facilitate easy use of this EoS to model other crude oils. Phase behavior calculations were performed for different crude oils in the presence of different amounts of injected gas, and the results were compared against similar calculations performed with a cubic EoS. It was observed that in the case of PC-SAFT, a single

set of parameters was sufficient to describe the phase behavior of the oil with various gas injection amounts. However, for a cubic EoS, one set of parameters failed to explain the experimental observations for other gas injection amounts sufficiently.

The asphaltene phase behavior curves were plotted on the pressure-temperature and pressure-composition axis. These curves were then combined to show the pressure depletion in a wellbore on an asphaltene phase envelope and to explain the lower asphaltene onset pressure. Based on the predicted asphaltene phase envelope, the amount of precipitated asphaltene was computed. Such modeling is essential for an asphaltene deposition simulator and solvent de-asphalters.

Little information is available about how fast the flocculated asphaltene particles create a fouling layer across the production wells from the flowing oil. The mechanisms of fouling of flocculated asphaltene particles from oil were studied under forced convection conditions using an accurate thermal approach [38]. The effects of oil velocity, composition, and temperature on the rate of asphaltene fouling were investigated. It was found that the deposition mechanism is dominant through the first few weeks and the depletion of the fouling is almost negligible. The rate of asphaltene fouling increases with increasing asphaltene composition and temperature while it decreases with increasing oil velocity. After clearing of the effects of operating conditions on the deposition process, the results of the experiments were used to create a mechanistic model to estimate the rate of asphaltene fouling formation under forced convection. The predictions of the model for the deposition rate of asphaltene are compared with measured data. Quantitative and qualitative correspondence between measured and predicted asphaltene deposition rates is reasonable. From the perspective of oil reservoir management, understanding the mechanisms and determining the rate of asphaltene deposition across the production wells has a high priority. Asphaltene deposition on well-tubing surface reduces the production of oil considerably. The

present study shows that oil velocity, bulk and surface temperatures, and flocculated asphaltene concentration have the primary influence on the deposition process. The deposition rate is increased as flocculated asphaltene concentration and surface temperature are increased. The deposition rate is inversely proportional to the oil velocity and decreases as the oil velocity is increased. The experimental results were used to develop a mechanistic model for the prediction of the rate of asphaltene deposition. Considering the complexity of the deposition process, the quantitative agreement between measured and predicted values is good [38].

The technique of fluid dynamic gauging has been demonstrated experimentally to function successfully in duct flows (laminar, transitional and turbulent), in agreement with the experimental results of Tuladhar et al. (2003) [39].

A novel method for on-line thermal resistance prediction of fouling in shell and tube heat exchangers can be applied under the condition of the availability of pressure, temperature, mass flow rate and thermophysical properties of both heat-exchanging media data[40]. The calculation sequence in the novel method is reliable and shows a good estimation of the fouling's thermal resistance even if the operating conditions are not steady. The process was validated using data retrieved from the operation parameter records of a heat exchanger network connected with a crude distillation unit (CDU) rated 800 tons/hour. The presented method for determination of the thermal resistance of fouling and its influence on the performance of industrial heat exchangers assumes the use of measurement data acquired during periods of normal plant operation without any special requirements on the stability of mass flow rates of process media. The data should be filtered to ensure high reliability of the industrial applications of the method, averaged and reconciled. In the determination of thermal resistance of fouling in a shell and tube heat exchanger, a multicell model of exchanger operation is employed. For both heat-exchanging liquids, the surface film

conductances are expressed by well-known empirical equations in which coefficients are regarded as variables. Their values are determined, together with the value of the thermal resistance of fouling, using the least-squares approach. The proposed method was thoroughly tested on the example of industrial shell and tube exchangers coupled with a crude distillation unit. The necessary database was extracted from the operation records covering two years of continuous plant operation. The critical calculation algorithms proved robust and insensitive to irregularities in the database caused by multiple short periods of interruption to data supply.

As discussed above a detailed literature review regarding asphaltene fouling is documented. The following subsections will discuss different kinds of fouling models showing their strength and weakness. The fouling models in the literature can be catigozied as follow:

1. Fouling Threshold Model
2. Solubility Models
3. Artificial Neural Network (ANN) Models
4. Equation of State Models
5. Experimentally Correlated Models
6. CFD Models

2.2.1 Fouling Threshold Model

Ebert and Panchal identified the presence of a threshold below which chemical reaction fouling by crude oil does not occur on heat transfer surfaces [3]. Knudsen et al. demonstrated this threshold phenomenon [41]. This phenomenon is essential for the design and operation of heat exchangers in refinery pre-heat trains used for the processing of crudes. The research shows that the consideration of the fouling threshold condition can be incorporated into the design procedures for shell-and-tube heat exchangers. The cost of improperly designed units, based on the conventional

use of ‘fouling factors,’ is demonstrated [42]. It becomes possible to select heat exchanger designs or configurations such that fouling is minimized when given a valid means of predicting fouling threshold conditions. In some situations, this means total mitigation. The interaction between the exchanger design and subsequent fouling rates is significant, and the potential cost penalties are high. A consideration of fouling behavior should, therefore, be an essential aspect of design. The methods described here require more information to extend the techniques to cover shell-side fouling, heat transfer augmentation and integrated pressure drop/network considerations.

Fouling threshold models for crude oil present a physically acceptable outline for studying fouling problems in refinery pre-heat trains [43]. The primary issue is that complete data sets of fouling thresholds in crude oil are scarce. Polley et al. [42, 43]worked on modeling (correlation) of the data set obtained by Knudsen et al. [41] for threshold fouling experiments conducted on a pilot plant. The threshold fouling equation proposed previously by Ebert and Panchal and extended by Panchal et al. [44] has been modified following a critique of some of its underlying assumptions. The research on developing threshold fouling equations was based on measured fouling rates, extrapolated to yield operating conditions that theoretically reach the no fouling point. In 2002, Polley et al. [43] attempted to model measured physical parameters that can help to reach an obvious fouling point. The validity of such a model to describe threshold fouling conditions in refinery pre-heat exchangers is discussed.

The significance of the crude oil fouling in heat exchangers is the main effect of reduced heat recovery and the pressure drop according to Yeap et al. [45]. They tried to reach a better understanding of these phenomena by applying different models to existing data from an industrial application. It was found that the ‘fouling threshold’ concept for modeling is the best way to describe fouling phenomena in the tube side because it considers both thermal and hydraulic

effects. The ‘fouling threshold’ model of crude oil fouling rates in the tube side provides a quantitative structure for including fouling reflections in the design and operation of refinery heat exchanger systems. The thermal understanding of the fouling phenomena was extended to add the hydraulic properties of fouling since it is a significant issue when it comes to model fluids in motion. Validation using the laboratory, pilot plant, and refinery data sets indicated that the modified Epstein model [46] is the strongest because it can be applied when the mass transfer occurs. For reaction fouling systems, the model made by Polley et al. [42, 43] is more applicable; all the models, however, feature significant uncertainty which must be considered in the analysis and pre-design stages. The hydraulic modeling results presented [45] indicate that the block approximation relating fouling resistance and fouling thickness is acceptable as long as the surface roughness doesn’t change. Hydraulic modeling also offers some insight into why thermal and pressure drop effects of fouling can be challenging to interpret. The simulations of individual heat exchanger performance for the case study illustrate that some designs are more robust towards fouling effects than others.

The results of Knudsen et al. [41] demonstrate the existence of a fouling threshold that was assumed by Ebert and Panchal [44], for the crude oil that was tested. The Ebert–Panchal model did not provide a good prediction of the conditions for the onset of fouling observed in these tests, mainly because it featured a much higher sensitivity to velocity than was observed. The Ebert–Panchal Model had been modified easily to yield a model that fit the data of Knudsen et al.[41]. There was no validation for the assumption that a model for the prediction of the onset of fouling can also be applied for the prediction of fouling rates once deposition has started. However, this simple model does provide reasonable predictions of subsequent fouling rates for the data presented by Knudsen et al. [41] By adjusting the activation energy parameter, the model also

provides good predictions for data from other studies. More research needs to be done to establish a reliable model for the onset of fouling and prediction of subsequent fouling rates. More systematic studies are required. Full reporting of crude physical properties is also necessary.

The concept of a thermal 'fouling threshold,' which was first introduced by Ebert and Panchal [47], was revisited alongside models of hydraulic effects of fouling to create a graphical tool, modified temperature field graphs, to assess chronic chemical reaction fouling effects in refinery heat exchangers. Fouling data were collected from the pilot plant and refinery operation and compared with two published threshold fouling models and a model based on the Epstein deposition model [46]. The model based on the Epstein deposition model showed the most agreement because it can accommodate fouling that is mass transfer based as well as reaction-controlled fouling. The hydraulic analysis indicated that the simple plate approximation for fouling layers gave a relation between heat transfer and pressure drop effects, on the other hand, roughness contributions are not significant. Where roughness effects (or tube blockage) are essential, the relationship between thermal and hydraulic performance is not straightforward. A case study, based on the network described by Panchal and Huang-Fu[48], is used to illustrate the thermo-hydraulic effects of fouling and the application of the modified temperature field plot.

The existing threshold fouling models predict that there will be an increase in initial fouling rates with an increase in bulk temperature. This is applicable for some crude oils in different conditions but also has limited application since some literature data do not agree with this finding.

2.2.2 Solubility Models

Another idea of explaining the phenomena of asphaltene precipitation is to describe them as solubility models (solid, colloidal, and micellization). The first important approach to modeling

asphaltene precipitation is the solubility model of Hirschberg et al. [49] Vapor-liquid equilibrium (VLE) calculations were first applied. The liquid was then divided into four components: asphaltene, resin, deasphalted oil, and solvent. The fugacities, molar volumes, and solubility parameters of oil, resin, and asphaltene were included in the model to estimate asphaltene precipitation. This approach matched experimental data with a limited degree of success.

The simplest model for precipitated asphaltene is the single-component solid model. The precipitated asphaltene was treated as a single component modeled as a solid phase, while oil and gas phases are modeled with cubic equations of state (EoSs). The solid model can require many experimental parameters and excessive tuning to match experimental data.

The first solubility model used to describe asphaltene precipitation was developed by Leontaritis and Mansoori [50]. In this model, a VLE calculation is first performed using an EoS to estimate the liquid composition in which asphaltene can flocculate. Then, the critical chemical potential, which is calculated using the Flory-Huggins theory [51, 52] is used to predict the onset of precipitation. The colloidal model is more applicable to situations in which dissociation of the asphaltene occurs [53].

A thermodynamic micellization model was used to describe asphaltene precipitation from Kuwaiti crude oil by Fahim et al. 2001 [53]. The main idea used for this model is based on asphaltene and resin formation then destruction after adding an alkane. An aggregate of asphaltene is surrounded by resin molecules that constitute the micellar phase. The asphaltene and resin that are not in the aggregate are dissolved in the bulk phase. Asphaltenes critical properties were predicted using the group contribution method, resin, and oil. The Peng-Robinson equation of state was used to predict the onset point and to perform flash calculations. The onset point and the amount of asphaltene

precipitated were measured. A variety of alkanes such as hexane, heptane, octane, and decane with varying volumes and temperatures were used to dissolve asphaltenes and resins. The model also was validated using high-pressure data. The model could describe the experimental data with a mean square error of 0.57%.

In the micellization models, the asphaltenes are assumed to aggregate, forming a micelle core, with resin molecules adsorbed on the surface of the core to stabilize the micelle. Victorov and Firrozabadi [14] formulated this model through aggregation equilibrium and the standard free energy of micellization. The polydispersity of asphaltene aggregates was considered by Victorov and Smirnova [54]. Their approach was then revised and combined with a more detailed description of the precipitated phase. Concentration is determined in this approach by the minimization of the Gibbs free energy of the crude oil bulk phase and the precipitated phase. The results of the micellization model agree well with experimental data.

Solubility models are very powerful in explaining how asphaltenes behave in the curd oil and how it dissolves back into it during the plant operation which will help significantly to explain the removal stage of the fouling process. On the other hand, these models are at a major disadvantage in predicting the fouling accurately when changing the conditions around the bulk flow of crude oil are changing, such as when surface roughness changes during the fouling.

2.2.3 Artificial Neural Network (ANN) Models

Kashani et al. [55] developed an advanced artificial neural network (ANN) for the purpose of fouling monitoring and prediction in crude oil pre-heaters. Such an online package is fed real data whenever it is ready from the monitored pre-heating network. This process steadily increases the efficiency of the ANN by improving the accuracy of the predicted fouling behaviors. The process

that was being monitored is an industrial shell and tube heat exchanger network for a crude oil distillation unit at a Tehran oil refinery. The special focus of this investigation was on the development of an optimum structure for the neural network model to avoid the overfitting problem and greatly enhance the generalization ability.

Moreover, it is believed that the present modeling approach, using a moving window neural network which was optimized with the method as mentioned earlier, can be widely applied to the online monitoring and long-term prediction of crude oil fouling in the industrial preheat exchangers that have a complex nature and time-varying process dynamics. The results showed that the suggested model can estimate the fouling, using only measurable online variables, two days in advance with an error of about 8%. Furthermore, the prediction ability can be extended to about ten days with an error of about 11%. As most chemical processes experience the fouling problem in their heat exchangers, the proposed monitoring scheme is expected to have broad applicability in the industry for operators and process engineers. It can also be applied to monitoring similar time-varying phenomena[55].

The approach of using artificial neural network (ANN) modeling to predict crude oil fouling in the preheat train of crude distillation units has been widely used. Amounts from the ANN models have been tested with appropriate sets of experimental data to compute overall mean relative error. The value of error was computed for three different threshold fouling models. The error of the ANN model was 26.2%, whereas the lowest error obtained for threshold fouling models was 47.9%. To identify the relative importance of the regulatory variables, a sensitivity analysis has also been applied. "This analysis showed that the influence of crude velocity and tube diameter on the fouling rate is higher than tube surface temperature" according to Aminian and Shahhosseini [56].

While the results obtained in Mena-Cervantes et al. [57] work for the specific experimental data that are reported by Panchal[3, 47, 48], Polley [42, 43, 45] and Nasr[33], the principles of the ANN modeling and sensitivity analysis are readily applicable to other situations.

Zahedi et al. [58] used the ANN approach for estimation of asphaltene precipitation. The Levenberg–Marquardt (LM) algorithm is the most suitable method to give an appropriate number of neurons in the hidden layer, which results in the minimum error. ANN's results showed the best performance for the prediction of asphaltenes fouling. The required data were collected and after filtering were used for the training of ANN. Its generalization ability checked the performance of the best-obtained network in predicting one-third of the testing data. The model predictions had a maximum mean square error (MSE) of 0.2787. The results showed the ANN's ability to predict the data. The ANN model was compared with the Flory–Huggins and the modified Flory–Huggins thermodynamic models. The comparison confirmed that ANN has a better performance [58].

ANN is a fancy way of regression and curve fitting. Its strength is that it can take so many input factors at the same time (such as flow patterns, velocity, composition, temperature, etc.) and give a proper prediction of fouling. The major disadvantage of ANN is that it needs an enormous amount of data to train the computer package to come up with a proper regression formula. Such amount of data is very hare to find and, as mentioned before, very expensive to obtain. Also, the regression formula is very powerful with interpolation but if the model inputs are outside the range of the training data, the prediction will be very far from reality.

2.2.4 Equation of State Models

Asphaltene fouling occurs when the thermodynamic operating conditions, such as temperature, pressure, and oil composition of crude oil change [59]. Therefore, modeling asphaltenes' phase

behavior using the transport model using either measure or calculated/correlated thermodynamic properties may help to control its fouling. The cubic-plus-association (CPA) [59] equation of state was used to model asphaltene precipitation in live crude oil. The concept of this equation was based on a combination of a physical part and an association term. The physical interaction in the mixture was considered in the physical part, and the chemical interaction and hydrogen bonding in the mixture was considered in the association part. The CPA equation of state was successfully applied to several mixtures of water, alcohols, glycols, organic acids, and hydrocarbons. The nature of asphaltene is associative, which means that its bond with itself is stronger than its bond with the crude oil mixture. This bond leads to form aggregation and then precipitation and fouling. The CPA equation can predict the phase behavior of asphaltene in crude oil. The cubic-plus-association equation of state was validated by experimental data of three live oils and the results of two other models. The results showed that the CPA equation of state could predict asphaltene precipitation with reasonable accuracy. For all samples used in the study, the absolute deviations from experimental points for the CPA model were less than 0.55 (or 55%) [59].

Another thermodynamic model that was used to predict asphaltenes phase behavior was the association equation of state (AEoS) model, which predicts asphaltene fouling in crude oil. Not only a physical term was used but a chemical term was also added by the AEoS to this model to explore the chemical nature of asphaltenes [60]. The results of this model were compared to experimental data of three live oils and the results of other models. The results showed the greater accuracy of the model in predicting the phase behavior of asphaltenes and other heavy components. Two equations of state (Peng Robinson (PR) and Soave-Redlich-Kwong (SRK)) were used, and the results showed that the model with the PR equation of state was more accurate than the SRK.

EoS are very powerful for explaining fluid behavior from the thermodynamic point of view. However, asphaltenes do not behave as a fluid during fouling. This fact is a major disadvantage for the EOS model.

2.2.5 Experimentally Correlated Models

Alcazar-Vara and Buenrostro-Gonzalez [61] worked on the rheological and thermodynamic characterization of the wax deposition phenomenon using three Mexican crude oils. The effect of wax and asphaltenes contents on wax precipitation and rheological properties of crude oils are evaluated and discussed. Wax formation temperature was measured by using differential scanning calorimetry, rheometry, and densitometry. The wax precipitation curves were found by using Fourier transform based infrared spectroscopy. Pour point temperatures were estimated according to the ASTM-D97 method[62], gelation temperatures were determined by rheological experiments which were performed using a controlled-stress rheometer.

Waxes of the crude oils were isolated and identified by gas chromatography/mass spectrometry and differential scanning calorimetry.

The methods used in Alcazar-Vara and Buenrostro-Gonzalez work for the wax appearance temperature measurement showed to be highly dependent on the crude oil composition. Results showed that the asphaltenes impact the liquid-solid equilibrium significantly and the rheological behavior of the crude oils under study, whereas the wax melting temperature was a key factor for evaluating the propensity of crude oils to present wax precipitation problems.

The first stage of the fouling process is called the induction period, in which the fouling rate is minimal (unnoticeable). A simple lumped parameter model based on fractional surface coverage has been developed to correlate experimental data in the induction period [63]. The primary

assumption here is that the fouling happens in layers. Covering the first layer (right on the pipe surface) occurs at the rate ($d\theta/dt$) (uncovered surface ($1-\theta$). It is further assumed that the foulant on the surface behaves as an attraction source for more fouling to occur. The fouling rate assumed to be first order with a rate constant k_1. Taking into consideration the removal rate during the flow process, it would also be first order with the constant k_2. This gives the equation 2.1.

$$\frac{d\theta}{dt} = k_1\theta(1-\theta) - k_2\theta \qquad (2.1)$$

This model enables describing the fouling process from the start of the induction period up to the steady fouling rate stage using one equation. The model was validated using data for crude oil fouling, calcium sulfate fouling, and whey protein fouling. The proposed term $t_{0.5}$, which is the time to reach 50% of the maximum surface coverage, θ_{max}, provides a practical measure of the length of the induction period. The model shows the effect of the surface temperature on the length of the induction period for the crude oil fouling systems. The model also describes in a semiquantitative manner the influence of velocity on the induction time. More research must be carried out on the effect of velocity because its effect is much more complicated than that of surface temperature. The influences of other relevant factors, such as the adhesive surface level and surface roughness, are also challenging to incorporate quantitatively in the model. Further research, therefore, needs to be focused on incorporating in the model parameters k_1 and k_2 as many as possible of the physical and chemical properties that influence deposition, attachment, and removal in specific applications.

Trejoa et.al [64] worked on asphaltenes of Maya and Isthmus crude oils in Mexico and studied the precipitating, fractionation and characterization. Isolation of asphaltenes was performed as per the ASTM D3279 [65] method requirements, which uses n-heptane for solvent precipitation.

Asphaltenes were separated into three parts by Soxhlet extraction with a binary solvent system of toluene and n-heptane. Carbon, hydrogen, oxygen, nitrogen, sulfur, and nickel and vanadium contents were determined in asphaltenes and in their fractions using atomic absorption and elemental analysis. vapor pressure osmometry (VPO) aggregate mass and nuclear magnetic resonance measurements were performed for crude samples. Important diversity in properties of unfractionated asphaltenes and asphaltenes fractions were observed. Some of these diversities were attributed to impurities in the unfractionated asphaltenes [64].

Trejoa et al. found that the amount of deposited asphaltenes has a linear relation with a binary toluene/n-heptane solvent volumetric ratio, which contradicts some literature reports [66]. Characterization results indicate that the least soluble asphaltene fraction has more complex structures than the other fractions. The aromaticity factor was not a useful parameter to show the differences in the structure of asphaltenes fractions. The number of aromatic carbons was suggested instead. The values of the average number of carbons per alkyl side chain of the fractions were higher than those found in the unfractionated asphaltenes. This finding was attributed to the impurities of the unfractionated sample, which contributed to reducing these values. It was corroborated that heteroatom contents in the unfractionated asphaltene behave as a sum of their fraction, which was also reported by others [67].

Biyanto et al. [68] chose a complex crude to preheat train (CPT) in a petroleum refinery to represent an industrial heat exchanger network experiencing excessive fouling and substantial economic losses due to fouling. Their study aimed to develop an optimum cleaning schedule. An improved optimization method for the cleaning schedule of the heat exchangers in the CPT was developed which considers the hydraulic impact of fouling through the additional pressure drops. The problem was very complicated and finding the global optimum was very difficult. Recent

stochastic methods were proposed and used to solve the complex problem without any simplifications or assumptions. Optimizations were conducted over an operating period of little less than 4 years following crude slate variations and operating conditions of the refinery. "The results show that ignoring the additional pumping cost in the objective function resulted in an optimal cleaning schedule that provides less savings (18.1% of maximum potential savings) in the net loss compared to the optimal cleaning schedule that utilizes the additional pumping cost in the objective function, which increases about 19.3% of maximum potential savings" according to Biyanto et al [68].

A second order asymptotic model was suggested to predict fouling. A single type of model was fitted to all heat exchangers which provided an easy assessment and comparison of fouling characteristics among the heat exchangers. All the physical and thermal properties needed for calculations and simulations were estimated using Aspen HYSYS software. Optimization of the cleaning schedule has been developed using some of the new stochastic algorithms, i.e., genetic algorithms (GA), particle swarm optimization (PSO), imperialist competitive algorithm (ICA), duelist algorithm (DA) optimization techniques to the solution of Mixed-Integer Nonlinear Programming (MINLP). A cleaning schedule optimization problem was formulated which includes the additional pumping cost as the objective function. The optimization problem, which is a MINLP problem, was solved using simple DA. The use of DA to solve the optimization problem did not involve any approximations or assumptions to simplify the problem. The proposed method could proceed for a small number of cleaning schedules in iteration and few iteration numbers and could achieve the maximum objective function value or global optimum. The simultaneous HEN optimizations of all heat exchangers were performed using the DA with objective functions with and without the additional pumping cost. It was observed that the

implementation of the optimal cleaning schedule with and without the additional pumping cost in the objective function resulted in a net savings increase of 19.3% and 18.1% of maximum potential savings during the 44 months of optimization, respectively.

Mozdianfard and Behranvand [27, 69] conducted an 8-year field study at the Eagle Oil Refining Company (EORC) refinery. This field study consisted of visual inspection and observation records, operational conditions data and fouling resistance analysis, as well as foulant chemical analysis. It was clear that post desalter and pre-flash drum (PDPF) heat exchangers experience severe irregular fouling [69]. This type of fouling affects more than 50% of its contents, which were sampled in two shutdowns at EORC, were inorganics, and consisted of ferrous compounds and calcium carbonate. Regarding EORC results and reported causes and remedies employed in the cases, a six-step mechanism based on that of Lambourn and Durrieu [70] was proposed, in which asphaltene interactions with water, salts, and iron sulfides lead to deposition of severe, tenacious and stable foulant on the tube surfaces of heat exchangers. Desalting and water injection, brine chloride hydrolysis and caustic injection, asphaltenes solubility dependence on temperature variation and its molecular structure as a surfactant agent as well as non-negligible shell-side fouling deposited off the vacuum gas oil have been identified as the useful factors discussed in detail. It should be considered that at PDPF exchangers, contrary to other preheaters, shell-side fouling is not negligible and merits specific investigations to be carried out which could commence with the fact that PDPF exchangers' shell-side fluid is often vacuumed gas oil and most n-paraffins responsible for gel formation at low temperatures are reported to lie within this asphaltene-free fraction of crude oil.

Optimization of the cleaning schedules of heat exchangers in crude preheat trains in refineries is a major issue [71]. The optimization method is based on a heuristic scheme composed of a set of

movements according to a strong rationale. Each evaluation of the objective requires the simulation of the behavior of the crude in preheat train during the investigated time. The optimization method can be employed using two alternatives: basic and recursive heuristic algorithms. The recursive option can obtain better solutions but demands higher computational efforts.

The proposed optimization approach does not present nonconvergence problems and does not demand any special attention related to control-parameter tuning. The proposed approach was applied to three examples of cleaning schedule optimization problems from the literature. The solutions obtained present values of the objective function better than the best solution previously reported. The objective function includes energy and cleaning expenses, subject to cleaning and operating constraints. Because the optimization and simulation algorithms form two separate layers, any simulation code can be employed, even including more complex fouling rate models, to consider the impact of temperature and flow velocity variations (e.g., Eberte Panchal and its variants [33, 43, 44, 47]. A simulation algorithm is employed that demands only the solution of two linear systems of equations for each time point, thus excluding any problem related to nonlinear equations. The optimization scheme can be used through two algorithm alternatives: a basic heuristic algorithm and a recursive heuristic algorithm. The latter can obtain better solutions but requires higher computational efforts. Both alternatives are robust, without suffering from nonconvergence problems.

Additionally, there are no control parameters to be tuned, which simplifies their utilization. Although the greedy rationale of the optimization scheme does not guarantee global optimality, performance comparisons with the literature results indicate that the proposed algorithms could identify cleaning schedules with objective function values similar to those previously reported.

Among three CPT examples investigated from the literature, in one proposed optimization schemes identified a better solution than those previously reported, and the others showed the highest difference between the best solution found in the literature and the proposed primary and recursive heuristic algorithms was not superior to 2.0% and 1.3%, respectively. In practical terms, the differences among the algorithms' performances were almost irrelevant when considering the uncertainty in the fouling rate models. Therefore, it is possible to conclude that the proposed algorithms are competitive alternatives for the optimization of heat exchanger cleaning schedules. According to this scenario, at this moment, the presented optimization scheme is being integrated as a plugin of the software Fouling TR, created in the Petrobras R&D Center (CENPES) for fouling monitoring of the company CPTs [72]. This computational routine will be integrated with another code responsible for fouling rate modeling [73], and this combine then will create a complete tool for fouling analysis and mitigation.

The process of asphaltene precipitation has a substantial effect on oil flow during primary oil production and oil recovery processes in the petroleum refineries. PVT properties of bottom hole live oil (e.g., resin to asphaltene ratio, onset pressure, bubble point pressure, reservoir temperature, asphaltene content, and gas to oil ratio) were used to generate a modified scaling model to account for asphaltene precipitation under pressure[74]. In the scaling model, the resin to asphaltene ratio in bottom hole live oil was included as an additional parameter. To examine the performance of the scaling model, the asphaltene precipitation experimental data at different pressures were correlated using PC-SAFT, Solid and Flory–Huggins as well as the scaling models. The results show that the scaling model predicts asphaltene precipitation more accurately than the PC-SAFT, Solid and Flory–Huggins models. Statistical analysis showed that the modified scaling model is highly dependent on the resin to asphaltene ratio and also the gas–oil ratio.

A modified scaling model based on PVT properties such as the resin to asphaltene ratio and gas-to-oil ratio was developed to account for asphaltene precipitation weight percent during pressure depletion and gas injection conditions, and the model was verified using the experimental data obtained in this work and those found in the literature. Also, a set of experiments was conducted using the bottom hole live oil sample under a pressure-depletion condition at high pressure, high-temperature equilibrium cell. The performance of the proposed scaling model in correlating the experimental asphaltene weight percent was compared with the data obtained using the PC-SAFT, Flory–Huggins and Solid models.

It is shown that the proposed model based on PVT properties can correlate more accurately the experimental data of asphaltene precipitation in comparison to those obtained by the other studied models with deviations less than 1%. Hence, PVT properties such as the resin-to-asphaltene ratio of bottom hole live oil has an essential role in asphaltene precipitation in the oil reservoir and should be included as a parameter in the scaling equation.

One of the main advantages of the scaling equation is the correlation of asphaltene precipitation experimental data under pressure depletion and gas injection conditions without involving asphaltene critical properties. The properties used in the scaling model are the resin-to-asphaltene ratio, onset pressure, bubble point pressure, reservoir temperature, and the asphaltene content gas-to-oil ratio, while the thermodynamic models are based on the complex properties of asphaltene such as the interaction coefficient, critical properties, acentric factor, solubility parameter and molecular weight of asphaltenes, which are not accurately specified. Sensitivity analysis showed that the proposed scaling model is highly sensitive to the properties of the resin-to-asphaltenes ratio and the gas–oil ratio of bottom hole live oil.

An experimental study was conducted to enhance heat-transfer coefficients when High-flux tubes were used in preference to plain tubes while boiling pentane.

The study involved two experimental facilities

- A single-tube pool boiler
- A 241 tube, 17 row by 17 column, thin slab reboiler.
- The pool boiling results show that the High-flux tubes produce heat-transfer coefficients that are up to five times larger than their plain tube counterparts. In flow boiling the enhancement is 3–6 times. High-flux tube performance is shown to deteriorate when small degrees of subcooling are present in the liquid [75].

Experimental models are very powerful to explain particular case. Their major disadvantage is that most of the designed experiments are just an approximation of reality, and their data are not real-time plant data. The most reliable kind of experimental data are the data collected from pilot plants with real data is very difficult and expensive to obtain.

2.2.6 Computational Fluid Dynamics (CFD) Models

Yang et al. [76] made three significant assumptions for modeling the fouling change with time. The first assumption is that the fouling gradually covers the surface. This assumption means the fouling will be created as layers above each other. The second assumption is that the rate of change of the surface coverage is directly proportional to the free area on the surface (faster fouling on the cleaner surfaces). The third assumption is that the fouling already on the surface acts as "seed" attracting other fouling materials to create the fouling layer. These three assumptions make it possible to model the rate of fouling deposition with a first order linear differential equation (equation 2.1).

This model makes it possible to describe the fouling process from the start of the induction period up to the steady fouling rate stage using a single and straightforward mathematical expression.

A conceptual method based on the computational fluid dynamic (CFD) technique for studying the fouling rate in crude oil pre-heaters was presented by Bayat et al. [77]. They simplified the complex mixture of the crude oil into three pseudo-components. The first component presented the crude oil, the second component presented asphaltene, and the third component presented the salts. Binary diffusion coefficients were used to describe the behavior of different species and the CFD was used to predict the fouling at the given operating conditions (pressure and temperature).

A two-dimensional CFD model was used along the axis of the pipe under study. It was assumed that the components of the fouling were asphaltene, coke, and salt characterized by their thermo-physical properties. It was found that the molecular diffusion coefficients were significant for such an application and accordingly the binary diffusion coefficients were put into five groups. This method gave an acceptable probability fouling rate to the asphaltene, salts, and coke, which are the main components of the fouling in the crude oil pre-heating network. The model was validated against a set of industrial data of a shell-and-tube heat exchanger. Simulation results showed that the CFD model predicted the fouling rate in both induction and developing periods of fouling. Besides, the CFD model has three distinguishing new features compared to the conventional threshold fouling models. It can consider the effects of chemical components, shell-side HTC, and turbulent flow on the crude oil fouling rate. Hence, the developed CFD model is expected to help evaluate crude oil fouling rates under new operating conditions.

Fouling in the tube side in crude oil preheat trains generates lots of issues such as increasing the pressure drop and pumping costs. Wang et al. [78] presented a method to estimate the optimum

crude oil velocity to reduce fouling rates in the heat exchanger tubes sides this leads to better heat transfer rates and a reduction in pressure drop. A “simulated annealing algorithm” is presented to describe an optimum point between heat transfer, pressure drops and fouling by changing fluid inlet velocity. Crude oil heating system data were used to verify the application of the system. Results showed that total annual cost is reduced by 6.4%, indicating that a better performance can be obtained by velocity re-distribution using the proposed method. Fluid flow velocity was used to correlate heat transfer, pressure drop, and fouling. To consider the unsteady nature of fouling rates, the entire time zone is divided into many time intervals, and the fouling rate is used to correlate adjacent time intervals. The results indicated that velocity could be correlated with the fouling rate, heat duty of heat exchangers, and heat capacity. The reason is that for the exchangers prone to fouling, higher velocity is required for mitigating fouling. For the exchangers with a large duty, higher velocity is required to exchange more heat. For hot streams with a significant heat capacity flow rate, the temperature drop is small after increasing the duty, resulting in a small reduction in the heat transfer driving force. It has also been found that the velocities of some heat exchangers are reduced after optimization. The reason is that those heat exchangers are not sensitive to velocity, and pressure drop can be reduced in those heat exchangers to save pump power. Because of the interaction between heat exchangers, the duties of some heat exchangers are reduced after optimization, but the energy saving for the network is increased. By redistributing velocity, the total annual cost for the case drops from $11,470.71k to $10,741.74k, about 6.4% reduction in total annual cost [78].

Maya crude oil fouling shows a direct dependence of its initial fouling rate on surface temperature but a rather complex dependency on velocity inside the tubes. The initial fouling rate decreased with the increase of the inlet velocity to a certain point where fouling disappeared. This finding

shows that surface shear stress is an essential factor. CFD simulation of fluid flow on the tube side revealed a heterogeneous distribution of surface shear stress. To compare the significance of this situation in the bare tube, a similar velocity concept was presented on the basis that at a given average velocity the fluid flow results in the same average wall shear stress regardless of the tube's shape. Using a similar velocity concept, the fouling data obtained using both a bare tube and a tube fitted with inserts can be correlated using a single model. Moreover, the fouling threshold conditions below which fouling is negligible can be predicted for both situations [79].

Fouling models that have been developed for simple round tubes cannot be applied directly to more complex geometries, including heat transfer inserts, non-round channels, etc., because the wall shear stress plays a crucial role not only in the fouling process itself but also in the determination of the threshold conditions below which fouling does not take place. Given the practical difficulty in measuring the wall shear stress experimentally in the case of complex geometries, CFD provides a relatively simple alternative provided that the simulated results can be validated using experimental data. In their work, the concept of equal velocity is developed such that a fouling model developed for bare round tubes can be extended for use with more complex geometries. It has been demonstrated, for example, that Yeap's model[45] can be adapted successfully to correlate the data of Maya crude oil fouling in both a bare round tube and a tube fitted with a hiTRAN® insert [80, 81] Moreover, the fouling threshold conditions for both cases can be predicted successfully, auguring well for the development of successful strategies to mitigate the high energy consuming fouling problem [45, 81].

Experimental and computational fluid dynamic (CFD) studies were performed for the technique of fluid dynamic gauging (FDG) in duct flows. Experiments were performed using a stainless-steel gauging nozzle located on the centerline of a Perspex duct of the square cross-section. Water was

used as a test fluid. Fluid inlet speed ranged between 0.0077 and 0.74m/s in the duct. CFD was used to simulate FDG in an imposed flow for steady state, incompressible, and laminar flows. Experimental data highly agreed with simulation results supporting the validity of both the experiments and the assumptions for the simulation. CFD simulations predicted the shear stresses below the lip of the nozzle and proved the practical working range of the pressure head ($0.1 < h/dt < 0.25$). This finding is a significant accomplishment which proved that CFD could be used to model the FDG flow accurately. This is also valuable for future work in this area, namely fouling in food, crude oil and cross-flow membrane systems [82].

The novelty of this work was the use of computational fluid dynamics simulating FDG in a duct flow system for steady, incompressible, and laminar flows. The numerical results, as judged by the value of the nozzle discharge coefficient, agreed with the experimental results of the their study to within 6%, and with the experimental results of Tuladhar et al. [39] to approximately 6%, thereby supporting the validity of both the experiments and the assumptions behind the numerical model. Application of this knowledge to the study of the stresses associated with deformation of a soft solid foulant yielded credible results: this information is not readily quantified using other techniques owing to the timescales and fragility of material [83].

A simple batch stirred cell has been used to investigate crude oil fouling on a plain test probe and a similar probe fitted with thin wires. The test results together with CFD simulation show that the wires on the probe surface promote turbulence and increase surface shear stresses; hence, under identical operating conditions, the fouling rate on the surface of the probe fitted with the wires was found to be significantly lower than on the surface. The fouling resistance data showed more distributed over time, which provides further evidence that the turbulence and added shear stress, and also even the associated circumferential shear stress distribution, were creating a more

substantial random removal of the fouling from the surface. With the help of the concept of equivalent Reynolds number, the fouling rate data become compatible regardless of the topologies of the test surfaces, such that fouling test results generated using a specific device, e.g., the batch stirred cell, can be applied to other types of heated surface.

CFD modeling techinques give the ability to analyze different problems whose experiments are very difficult and expensive, which is the exact case of asphaltenes fouling. The CFD techniques offer the capacity for studying a system under conditions over its limits, which solves the problem for obtaining more and more data to do proper regression, interpolation and extrapolation. CFD uses real physics phenomena (e.g. the transport model for this research) which makes CFD very flexible and can have a high level of details that can be added or removed based on the proper assumptions. This, of course, will give more accurate description of the case under study. This flexibility of details makes the CFD approach an accurate prediction of fouling. The disadvantage of CFD is that it takes too much time for simulation, and it needs a strong machine to simulate. This time issue can be solved with the proper assumptions to simplify the mathematics behind the model.

2.3 Retardation of fouling

Shell-and-tube heat exchangers are generally designed by a homogeneous and constant fouling resistance that is specified in advance by the heat exchanger operators. The design process is then one of identifying the best exchanger design that achieves the thermal duty within the specified pressure drop constraints. It has been that this approach can be extended to the design of heat exchangers where the design fouling resistance depends on velocity. Butterworth [84] briefly reviews the main findings of the previous studies and goes on to treat the case where the fouling

also depends on the local temperatures. The Ebert-Panchal form of a fouling rate equation is used to evaluate this fouling dependence [47]. Rational ways of separating the design from the operation are proposed [84]. Introducing the effect of temperature on fouling into the design of heat exchangers is shown to be quite complicated because the final, design-fouling resistance depends on the history of operation of the exchanger. Three methods are considered for overcoming this problem. The first is to creat the design using the fouling threshold to ensure a clean exchanger. The second is to use asymptotic fouling resistance, which can be done but may not be fully compatible with the Ebert–Panchal method used in the current calculations.

Nevertheless, it would be a sensible way to proceed with the design in those cases where the right equation exists to predict asymptotic fouling. The third method is to analyze the fouling buildup using an assumed operational history. The calculations involved in this consume quite a bit of time, but a simple hypothesis is shown to work remarkably well. In this hypothesis, they assumed that the fouling rate over the operating period is equal to that at the end. There is some justification for this hypothesis.

As the aggregation of asphaltene causes fouling and deposition, exact identification of the molecular and aggregate structure and aggregation technique is essential to prevent asphaltene fouling. Their research literature presents four models for the formation techniques of asphaltene aggregates [85]:

1. Micellar/colloidal
2. Polymeric
3. Solubility
4. Modified Yen models

The modified Yen model shows more consistency with the latest research which has adopted the idea of “island molecular structure” or “small nano-aggregates” for asphaltene. Experimental studies have showen that the dominant mechanism of aggregate formation depends on asphaltene structure, intermolecular forces, and the solubility definition of asphaltene.

Research further indicates that methods used in experimental studies provide valuable information on the molecular structure, formation mechanism, morphology, and size of asphaltene aggregates. The results show the following:

1. The asphaltene molecular structure is determined to be in the form of poly-aromatic rings and aliphatic chains with different heteroatom functional groups.
2. The asphaltene molecular architecture depends on the type of oil and solvent used to separate the asphaltene.
3. The molecular architecture, different fundamental forces (e.g., the Pi interaction between aromatic sheets, hydrogen bonds, heteroatom type, and electron transfer), and the solubility definition of asphaltene are the most critical factors in the asphaltene aggregate formation mechanism.

A single model cannot explain all observations because of constraints in each model. In comparison with other models, the modified Yen model shows better predictions of experimental results. Yen model provides a complete definition for asphaltene nano and cluster aggregation from asphaltene molecules with the island structure [85].

Mena-Cervantes et. al [57] developed a novel multifunctional stabilizer of asphaltenes for the control of fouling in different stages of the petroleum industry. Stabilizers were obtained from the reaction between poly-iso-butenyl succinic anhydride (PIBSA), 2-(2-amino-ethylamino) ethanol

(AEAE) and an R-substituted aldehyde, resulting in three 2-R-(poly-iso-butylene-succinimidyl) oxazolidines as prototypes of multifunctional Asphaltenes stabilizers, where R is –H (P1), $–C_5H_{11}$ (P2) or –ortho(OH)C_6H_4 (P3). Compounds P1-3 were characterized by FTIR, 1H, 13C, and 2D NMR spectroscopies, and assessed in four different types of evaluations: (i) Asphaltenes dispersion by UV–vis, (ii) displacement of Asphaltenes onset precipitation, at ambient conditions, (iii) inhibition of electric field induced deposition of Asphaltenes, and (iv) displacement of Asphaltenes onset precipitation, at reservoir conditions. All the latter individual efficiencies were included in a multifunctional development factor (MDF) results of in 0.626 for P1, 0.326 for P2, and 0.679 for P3, where the higher value corresponded to the highest efficiency. For comparison purposes, two commercial stabilizers of Asphaltenes were also evaluated, resulting in MDF of 0.012 and 0.162, being P1-3 better multifunctional chemicals. The best novel prototype was selected for industrial evaluation by considering technical and economic criteria. Thus, the P1 compound was chosen as an active component of DAIM commercial chemical and was successfully assessed on an industrial scale in a production well of Petróleos Mexicanos (PEMEX) to control Asphaltenes fouling. The continuous injection of DAIM produced essential advantages to the oil productivity, such as the decrease of the frequency of cleaning operations from 11 to 4 times in a one-year testing period and the reduction of production rate decreased from -1.48 to -0.032 m3/day.

2.4 Fouling Cost Effects

Improving cleaning schedules for refinery preheat trains requires a strong fouling model, and the capability to handle the thermal and hydraulic effects of fouling. Typically, PHT are responsible of 50% of all fouling costs in the whole refinery. For a refinery with treatment capacity of 100,000 barrels per day that cost could reach up to 25.7 million USD per year. That cost is distributed

between maintenance manpower (1%), extra needed fuel in the furnace (21%), and the loss due to throughput reduction (78%). Successful modeling of the fouling process will enable refineries around the world to reduce all the cost aspects. Lots of case studies performed cost analysis and some of them were successful to reduce the cost of fouling by 70% through modeling and targeting these three aspects of cost. [3,31,41,44-45,47,83]

2.5 Summary of Literature Review

The first section of this chapter makes it very handy to do experiments to come up with proper physical and chemical properties for crude oils and asphaltenes and to be able to use these properties in the modeling process. This will be explained more in chapter 4.

The second section shows many approaches to the understanding of what is happening in the system. Different modeling techniques were used to reach such an understanding. Due to the non-availability of enough data, lots of these models are limited to certain kind of crudes or only limited to explain a certain mechanism of fouling. Some model explains the fouling in one direction such as deposition only but cannot explain the fouling removal. CFD is the most powerful in explaining the macro scheme of events. Threshold models are better in explaining the micro scheme of events. The most proper approach for work is to combine the CFD approach with a threshold model. This will enable the package to simulate the bulk motion of the fluid in the tube side of the heat exchanger and the threshold model will serve as a boundary condition for the asphaltenes fouling phenomena. This will be explained more in chapter 3.

The last section of the literature is an application of the use of a model or an experiment to reach optimum operating conditions to reduce or prevent the fouling.

Chapter 3: Numerical Model

This chapter outlines the numerical setup of the phenomenon of Asphaltenes fouling in the tube side of the heat exchangers in the preheating network. Regularly, the problem for the heat exchanger is usually about heat and momentum transport. However, for the case of fouling, it is essential to consider a species balance to be able to model and acceptably simulate the problem. For this research, the model would be in cylindrical coordinates system where z it the axial length of the tube, r is the radius of the tube, and θ is the radial direction of the tube which means the problem in hand will be axis-symmetrical, and this will make the computation of the problem faster.

Conventionally in pre-heat train (PHT), crude oil (process fluid) is in the tube side of the shell and tube heat exchanger, and the utility fluid (hot fluid) is on the shell side. Utility fluids are refined products from different units in the refinery with elevated temperature. This process provides up to 60-70% of the energy needed in PHT [71]. Another important criterion of those refined products is that the asphaltenes content is very low.

Figure 3.1 shows a simplified schematic of the fouling problem in the tube side of shell and tube heat-exchanger. The Transport Model is applied for the tube side fluid (crude oil). The Model describes the heat and momentum balance for crude oil as well as the formation rate of fouling layer inside the tube.

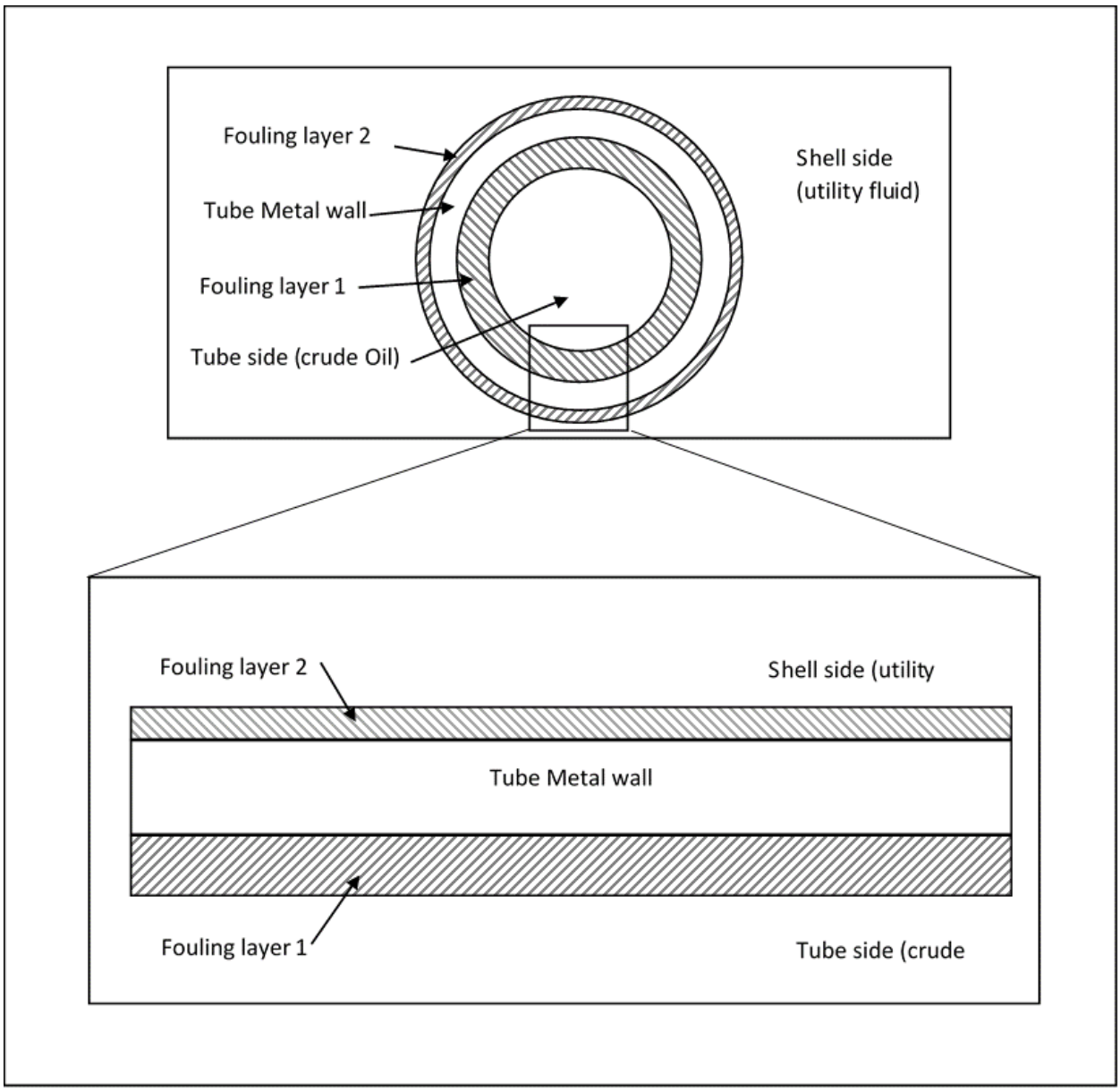

Figure 3.1: simplified schematic of the heat-exchanger tube during fouling

3.1 Species Transport (Asphaltenes Balance)

Mass balance is based on the physical concept of conservation of mass. The concentration difference for species between two regions is the main driving force for the movement of that

species from a high concentration region to a low concentration region. The mass balance used in this work is based on Fick's law of diffusion with the addition of advection $\rho(\vec{u}.\nabla)\omega_a$ [86-89].

$$\rho\frac{\partial\chi_a}{\partial t}+\nabla.\vec{j}_a+\rho(\vec{u}.\nabla)\chi_a=R_a \tag{3.1}$$

Assumptions:

- density and diffusivity are functions of temperature (chapter 4)
- velocity is only in the pipe axial direction (u_r=u_θ=0)
- axial symmetry (concentration changes in the z and r directions only $\frac{d\chi_a}{d\theta}=0$)

$$\vec{N}_a=\vec{j}_a+\rho\vec{u}\chi_a \tag{3.2}$$

$$\vec{j}_a=-\left(\rho D_a^f\left(\frac{1}{r}\frac{\partial r\chi_a}{\partial r}\hat{r}+\frac{\partial\chi_a}{\partial z}\hat{z}\right)+\rho\chi_a D_a^f\frac{\frac{1}{r}\frac{\partial rM_n}{\partial r}\hat{r}+\frac{\partial M_n}{\partial z}\hat{z}}{M_n}+D_a^T\frac{\frac{1}{r}\frac{\partial rT}{\partial r}\hat{r}+\frac{\partial T}{\partial z}\hat{z}}{T}\right) \tag{3.3}$$

$$M_n=\left(\sum_i\frac{\chi_i}{M_i}\right)^{-1} \tag{3.4}$$

$$assume: M_n=const, D_a^T=0$$

$$\vec{j}_a=-\rho D_a^f\frac{1}{r}\frac{\partial r\chi_a}{\partial r}\hat{r}-\rho D_a^f\frac{\partial\chi_a}{\partial z}\hat{z} \tag{3.5}$$

$$\rho\frac{\partial\chi_a}{\partial t}+\nabla.\left(-\rho D_a^f\frac{1}{r}\frac{\partial r\chi_a}{\partial r}\hat{r}-\rho D_a^f\frac{\partial\chi_a}{\partial z}\hat{z}\right)+\rho(\vec{u}.\nabla)\chi_a=R_a \tag{3.6}$$

$$\rho \frac{\partial \chi_a}{\partial t} + \frac{1}{r}\frac{\partial}{\partial r}\left(-\rho D_a^f \frac{\partial r \chi_a}{\partial r}\right) + \frac{\partial}{\partial z}\left(-\rho D_a^f \frac{\partial \chi_a}{\partial z}\right) + \rho u_z \frac{\partial \chi_a}{\partial z} = R_a \quad (3.7)$$

Where

- z is the axial direction
- r is the radial direction
- t is time
- j is mass flux due to diffusion
- N_a overall mass flux (diffusion and advection)
- χ_a is weight fraction of Asphaltenes (the boundary conditions of χ_a can be obtained from SARA analysis)
- u is bulk velocity
- ρ crude density (a function of temperature)
- D_A asphaltenes diffusion coefficient (a function of temperature, composition, flow, and asphaltenes in crude diffusion (d_a))
- R_a is the rate of disappearance/precipitation of Asphaltenes (a function of temperature) which can be estimated as the rate of reaction
- M is the molecular weight

The primary boundary conditions used to solve this equation is to relate the fouling rate models to the overall mass flux in the radial direction (eq. 3.8)

$$N_{ar} = k_a \rho_a \frac{dR_f}{dt} \quad (3.8)$$

Where

- N_{ar} is the mass flux in the radial direction
- k_a is the thermal conductivity of asphaltenes
- ρ_a is the density of asphaltenes
- $\frac{dR_f}{dt}$ fouling rate model

The importance of the mass balance is that it enables the user to monitor the concentration of Asphaltenes in the system. It is predicted to see a reduction of the concentration of the asphaltenes in the system with time. This reduction means that Asphaltenes are precipitating on the inner walls of the pipe creating fouling and adding to the heat resistance.

3.2 Conservation of Momentum

The primary objective of the momentum balance is to describe the velocity and pressure profiles in the tube side and calculate shear rate and shear stress and any other factors the fouling model and the mass balance requires. The velocity profile is essential for the species and energy balances as well. The driving force for fluids to movement is the difference in pressure (head pressure) [86-89].

Assumptions:

- flow is turbulent
- density and viscosity are functions of temperature
- velocity is only in the pipe axial direction (u_z)
- axial symmetry (velocity changes in the z and r directions only $\frac{du_z}{d\theta} = 0$)

The turbulence parameters in the model is estimated using the STT k-ω interface model [90]. This interface model solves the Navier-Stokes equations for the conservation of momentum and the continuity equation for conservation of mass. The selection of this model is subject to change due to the ability of the data and information in the future. The STT k-ω model [91, 92] generates Equation 3.9 into the following format:

$$\rho\frac{\partial\vec{u}}{\partial t}+\rho\left(\vec{u}.\nabla\right)\vec{u}=\nabla.\left[-p\tau+\left(\mu+\mu_T\right)\left(\nabla\vec{u}\right)^T-\frac{2}{3}\left(\mu+\mu_T\right)\left(\nabla.\vec{u}\right)\tau-\frac{2}{3}\rho k\tau\right] \tag{3.9}$$

Where

- z is the axial direction
- r is the radial direction
- t is time
- p is system pressure
- τ is shear stress
- u is velocity
- μ is the apparent model viscosity $\mu=\mu_{oil}+\mu_t$

  Where

  - μ_{oil} is the viscosity of the crude oil
  - μ_t is the turbulent dynamic viscosity equation 3.35

Where the velocity vector in the cylindrical system can be written as:

$$\vec{u} = u_r\hat{r} + u_\theta\hat{\theta} + u_z\hat{z} \tag{3.10}$$

In the tube flow the overall bulk motion is in the z direction ($u_\theta = u_r = 0$)

$$\vec{u} = u_z\hat{z} \tag{3.11}$$

The assumption of the axial symmetry that was made for the conservation of mass is still valid in the conservation of momentum $\frac{\partial u_z}{\partial \theta} = 0$ and accordingly the velocity gradient and gradient dot product will be:

$$\nabla\vec{u} = \frac{1}{r}\frac{\partial r u_z}{\partial r}\hat{r}\hat{z} + \frac{\partial u_z}{\partial z}\hat{z}\hat{z} \tag{3.12}$$

$$\nabla.\vec{u} = \frac{\partial u_z}{\partial z} \tag{3.13}$$

The shear tensor can be presented as follow

$$\tau^T = \begin{bmatrix} \tau_{rr}\hat{r}\hat{r} + \tau_{\theta r}\hat{\theta}\hat{r} + \tau_{zr}\hat{z}\hat{r} + \\ \tau_{r\theta}\hat{r}\hat{\theta} + \tau_{\theta\theta}\hat{\theta}\hat{\theta} + \tau_{z\theta}\hat{z}\hat{\theta} \\ +\tau_{rz}\hat{r}\hat{z} + \tau_{\theta z}\hat{\theta}\hat{z} + \tau_{zz}\hat{z}\hat{z} \end{bmatrix} \tag{3.14}$$

And due to the absence of bulk motion in r and θ direction and the axial symmetry ($u_\theta = u_r = 0, \frac{\partial}{\partial\theta} = 0$) equation 3.14 will transform into equation 3.15

$$\tau^T = \left[\tau_{rz}\hat{r}\hat{z} + \tau_{zz}\hat{z}\hat{z}\right] \tag{3.15}$$

Where:

$$\tau_{rz} = -\mu \frac{\partial u_z}{\partial r} \tag{3.16}$$

$$\tau_{zz} = -\mu \left[2 \frac{\partial u_z}{\partial z} \right] + \left(\frac{2}{3} \mu - \mu_T \right) \left(\frac{\partial u_z}{\partial z} \right) \tag{3.17}$$

Substituting equation 3.15, 3.16, and 3.17 into equation 3.9 will generate

$$\rho \frac{\partial u_z \hat{z}}{\partial t} + \rho \left(u_z \hat{z} . \frac{\partial}{\partial z} \hat{z} \right) u_z \hat{z} = \nabla . \begin{bmatrix} -p \left[\tau_{rz} \hat{r}\hat{z} + \tau_{zz} \hat{z}\hat{z} \right] + \left(\mu + \mu_T \right) \left(\frac{1}{r} \frac{\partial r u_z}{\partial r} \hat{r}\hat{z} + \frac{\partial u_z}{\partial z} \hat{z}\hat{z} \right)^T \\ -\frac{2}{3} \left(\mu + \mu_T \right) \left(\frac{\partial u_z}{\partial z} \right) \left[\tau_{rz} \hat{r}\hat{z} + \tau_{zz} \hat{z}\hat{z} \right] - \frac{2}{3} \rho k \left[\tau_{rz} \hat{r}\hat{z} + \tau_{zz} \hat{z}\hat{z} \right] \end{bmatrix} \tag{3.18}$$

Solving the vector products will result in:

$$\rho \frac{\partial u_z}{\partial t} \hat{z} + \rho u_z \frac{\partial u_z}{\partial z} \hat{z} = \nabla . \begin{bmatrix} -p\tau_{rz} \hat{r}\hat{z} - p\tau_{zz} \hat{z}\hat{z} + \frac{1}{r} \left(\mu + \mu_T \right) \frac{\partial r u_z}{\partial r} \hat{r}\hat{z} + \\ \left(\mu + \mu_T \right) \frac{\partial u_z}{\partial z} \hat{z}\hat{z} - \frac{2}{3} \left(\mu + \mu_T \right) \left(\frac{\partial u_z}{\partial z} \right) \tau_{rz} \hat{r}\hat{z} + \\ \frac{2}{3} \left(\mu + \mu_T \right) \left(\frac{\partial u_z}{\partial z} \right) \tau_{zz} \hat{z}\hat{z} - \frac{2}{3} \rho k \tau_{rz} \hat{r}\hat{z} + \frac{2}{3} \rho k \tau_{zz} \hat{z}\hat{z} \end{bmatrix} \tag{3.19}$$

Solving the gradient dot product will produce the final non-vector form (equations 3.20 and 3.21)

$$\rho \frac{\partial u_z}{\partial t} + \rho u_z \frac{\partial u_z}{\partial z} = \left(\frac{1}{r} \frac{\partial}{\partial r} r\hat{r} + \frac{\partial}{\partial z} \hat{z} \right) . \begin{bmatrix} -p\tau_{rz} \hat{r} - p\tau_{zz} \hat{z} + \frac{1}{r} \left(\mu + \mu_T \right) \frac{\partial r u_z}{\partial r} \hat{r} \\ + \left(\mu + \mu_T \right) \frac{\partial u_z}{\partial z} \hat{z} - \frac{2}{3} \left(\mu + \mu_T \right) \left(\frac{\partial u_z}{\partial z} \right) \tau_{rz} \hat{r} \\ + \frac{2}{3} \left(\mu + \mu_T \right) \left(\frac{\partial u_z}{\partial z} \right) \tau_{zz} \hat{z} - \frac{2}{3} \rho k \tau_{rz} \hat{r} + \frac{2}{3} \rho k \tau_{zz} \hat{z} \end{bmatrix} \tag{3.20}$$

$$\rho\frac{\partial u_z}{\partial t}+\rho u_z\frac{\partial u_z}{\partial z}=\begin{bmatrix}\frac{1}{r}\frac{\partial}{\partial r}\left(-rp\tau_{rz}\right)-\frac{\partial}{\partial z}\left(p\tau_{zz}\right)+\frac{1}{r}\frac{\partial}{\partial r}\left(r\frac{1}{r}\left(\mu+\mu_T\right)\frac{\partial ru_z}{\partial r}\right)\\+\frac{\partial}{\partial z}\left(\left(\mu+\mu_T\right)\frac{\partial u_z}{\partial z}\right)-\frac{1}{r}\frac{\partial}{\partial r}\left(r\frac{2}{3}\left(\mu+\mu_T\right)\left(\frac{\partial u_z}{\partial z}\right)\tau_{rz}\right)\\+\frac{\partial}{\partial z}\left(\frac{2}{3}\left(\mu+\mu_T\right)\left(\frac{\partial u_z}{\partial z}\right)\tau_{zz}\right)-\frac{1}{r}\frac{\partial}{\partial r}\left(r\frac{2}{3}\rho k\tau_{rz}\right)+\frac{\partial}{\partial z}\left(\frac{2}{3}\rho k\tau_{zz}\right)\end{bmatrix} \tag{3.21}$$

The next step is to solve equation 3.21 with the continuity equation 3.22

$$\frac{\partial\rho}{\partial t}+\nabla.\left(\rho\vec{u}\right)=0 \tag{3.22}$$

Considering the z direction bulk motion and the axial symmetry continuity equation can be presented as equation 3.23

$$\frac{\partial\rho}{\partial t}+\frac{\partial\rho u_z}{\partial z}=0 \tag{3.23}$$

For the STT k-ω model[90-92] the balance of kinetic energy can be written in the following vector format:

$$\rho\frac{\partial k}{\partial t}+\rho\left(\vec{u}.\nabla\right)k=\nabla.\left[\left(\mu+\mu_T\sigma_k\right)\nabla k\right]+P-\beta_0^*\rho\omega k \tag{3.24}$$

Solving the vector products and the gradient dot product will produce the final non-vector form for kinetic energy balance (equation 3.24)

$$\rho\frac{\partial k}{\partial t}+\rho u_z\frac{\partial k}{\partial z}=\nabla.\left[\left(\mu+\mu_T\sigma_k\right)\frac{1}{r}\frac{\partial rk}{\partial r}\hat{r}+\left(\mu+\mu_T\sigma_k\right)\frac{\partial k}{\partial z}\hat{z}\right]+P-\beta_0^*\rho\omega k \tag{3.25}$$

$$\rho\frac{\partial k}{\partial t}+\rho u_z\frac{\partial k}{\partial z}=\frac{1}{r}\frac{\partial}{\partial r}\left(r\left(\mu+\mu_T\sigma_k\right)\frac{1}{r}\frac{\partial rk}{\partial r}\right)+\frac{\partial}{\partial z}\left(\left(\mu+\mu_T\sigma_k\right)\frac{\partial k}{\partial z}\right)+P-\beta_0^*\rho\omega k \tag{3.26}$$

The balance of on rate of conversion of turbulence into heat by molecular viscosity (Dissipation Rate ω) can be written in the following vector format:

$$\rho\frac{\partial\omega}{\partial t}+\rho\left(\vec{u}.\nabla\right)\omega=\nabla.\left[\left(\mu+\mu_T\sigma_\omega\right)\nabla\omega\right]+\frac{\gamma}{\mu_T}\rho P-\beta\rho\omega^2+2\left(1-f_{v1}\right)\frac{\sigma_{\omega2}\rho}{\omega}\nabla k.\nabla\omega \tag{3.27}$$

Solving the vector products and the gradient dot product will produce the final non-vector form for kinetic energy balance (equation 3.27)

$$\rho\frac{\partial\omega}{\partial t}+\rho u_z\frac{\partial\omega}{\partial z}=\begin{bmatrix}\nabla.\left[\left(\mu+\mu_T\sigma_\omega\right)\frac{1}{r}\frac{\partial r\omega}{\partial r}\hat{r}+\left(\mu+\mu_T\sigma_\omega\right)\frac{\partial\omega}{\partial z}\hat{z}\right]+\frac{\gamma}{\mu_T}\rho P-\\ \beta\rho\omega^2+2\left(1-f_{v1}\right)\frac{\sigma_{\omega2}\rho}{\omega}\left(\frac{1}{r}\frac{\partial rk}{\partial r}\hat{r}+\frac{\partial k}{\partial z}\hat{z}\right).\left(\frac{1}{r}\frac{\partial r\omega}{\partial r}\hat{r}+\frac{\partial\omega}{\partial z}\hat{z}\right)\end{bmatrix} \tag{3.28}$$

$$\rho\frac{\partial\omega}{\partial t}+\rho u_z\frac{\partial\omega}{\partial z}=\begin{bmatrix}\frac{1}{r}\frac{\partial}{\partial r}\left(r\left(\mu+\mu_T\sigma_\omega\right)\frac{1}{r}\frac{\partial r\omega}{\partial r}\right)\\ +\frac{\partial}{\partial z}\left(\left(\mu+\mu_T\sigma_\omega\right)\frac{\partial\omega}{\partial z}\right)\end{bmatrix}+\frac{\gamma}{\mu_T}\rho P-\beta\rho\omega^2+2\left(1-f_{v1}\right)\frac{\sigma_{\omega2}\rho}{\omega}\left(\frac{1}{r^2}\frac{\partial rk}{\partial r}\frac{\partial r\omega}{\partial r}+\frac{\partial k}{\partial z}\frac{\partial\omega}{\partial z}\right) \tag{3.29}$$

Reciprocal wall distance is calculated from the following equations and it will be used to calculate the inertia in the following order

$$\nabla G.\nabla G+\sigma_\omega G\left(\nabla.\nabla G\right)=\left(1+2\sigma_\omega\right)G^4 \tag{3.30}$$

$$\left(\frac{1}{r}\frac{\partial rG}{\partial r}\hat{r}+\frac{\partial G}{\partial z}\hat{z}\right).\left(\frac{1}{r}\frac{\partial rG}{\partial r}\hat{r}+\frac{\partial G}{\partial z}\hat{z}\right)+\sigma_\omega G\left(\nabla.\left(\frac{1}{r}\frac{\partial rG}{\partial r}\hat{r}+\frac{\partial G}{\partial z}\hat{z}\right)\right)=\left(1+2\sigma_\omega\right)G^4 \tag{3.31}$$

$$\left(\frac{1}{r}\frac{\partial rG}{\partial r}\right)^2+\left(\frac{\partial G}{\partial z}\right)^2+\sigma_\omega G\left(\frac{1}{r}\frac{\partial}{\partial r}\left(r\frac{1}{r}\frac{\partial rG}{\partial r}\right)+\frac{\partial}{\partial z}\left(\frac{\partial G}{\partial z}\right)\right)=\left(1+2\sigma_\omega\right)G^4 \tag{3.32}$$

$$\left(\frac{1}{r}\frac{\partial rG}{\partial r}\right)^2+\left(\frac{\partial G}{\partial z}\right)^2+\sigma_\omega G\frac{1}{r}\frac{\partial^2 rG}{\partial r^2}+\frac{\partial^2 G}{\partial z^2}=\left(1+2\sigma_\omega\right)G^4 \tag{3.33}$$

$$I_\omega=\frac{1}{G}-\frac{I_{ref}}{2} \tag{3.34}$$

$$\mu_T=\rho\frac{k}{\omega} \tag{3.35}$$

$$P=\min\left(P_k,10\beta_0^*\rho\omega k\right) \tag{3.36}$$

$$P_k=\mu_T\left[\left[\frac{1}{r}\frac{\partial ru_z}{\partial r}\hat{r}\hat{z}+\frac{\partial u_z}{\partial z}\hat{z}\hat{z}\right]:2\left(\frac{1}{r}\frac{\partial ru_z}{\partial r}\hat{r}\hat{z}+\frac{\partial u_z}{\partial z}\hat{z}\hat{z}\right)-\frac{2}{3}\frac{\partial u_z}{\partial z}\right]-\frac{2}{3}\rho k\frac{\partial u_z}{\partial z} \tag{3.37}$$

$$\phi=f_{v1}\phi_1+\left(1-f_{v1}\right)\phi_2 \tag{3.38}$$

Where ϕ can be $\beta,\gamma,\sigma_k,\sigma_\omega$ and their values can be found in table 3.1

Table 3.1: Turbulence model parameters

Parameter	Value	Unit
a_1	3.1	Dimensionless
β_0^*	0.09	Dimensionless
β_1	0.075	Dimensionless
β_2	0.0828	Dimensionless
γ_1	5/9	Dimensionless
γ_2	0.44	Dimensionless
σ_{k1}	0.85	Dimensionless
σ_{k2}	1	Dimensionless
$\sigma_{\omega1}$	0.5	Dimensionless
$\sigma_{\omega2}$	0.856	Dimensionless

3.3 Conservation of Energy

Conservation of energy in the model produces an accurate temperature profile on the tube side. The importance of this profile is making it handy to estimate the fluid properties such as viscosity and density, which are important for momentum equations, as well as diffusivity and in the species conservation equations and fouling models. The heat/energy balance is known as the first law of thermodynamics, which states that energy cannot be created or destroyed; energy can just be transferred from one form to another. The driving force for heat transfer is the temperature difference. Heat moves from the high-temperature point to the low-temperature point [86-89].

Assumptions:

- density and thermal conductivity are functions of temperature
- velocity is only in the pipe axial direction (v_z)
- axial symmetry (Temperature changes in the z and r directions only $\frac{dT}{d\theta} = 0$)

Temperature balance can be written in the following vector form:

$$\rho C_p \frac{\partial T}{\partial t} + \rho C_p \vec{u}.\nabla T = \nabla.\left(k\nabla T\right) + Q_{in} \tag{3.39}$$

Where the temperature gradient will be

$$\nabla T = \frac{1}{r}\frac{\partial rT}{\partial r}\hat{r} + \frac{\partial T}{\partial z}\hat{z} \tag{3.40}$$

Substituting

$$\rho C_p \frac{\partial T}{\partial t} + \rho C_p \vec{u}.\left(\frac{1}{r}\frac{\partial rT}{\partial r}\hat{r} + \frac{\partial T}{\partial z}\hat{z}\right) = \nabla.\left(\frac{1}{r}k\frac{\partial rT}{\partial r}\hat{r} + k\frac{\partial T}{\partial z}\hat{z}\right) + Q_{in} \tag{3.41}$$

$$\rho C_p \frac{\partial T}{\partial t} + \rho C_p u_z \frac{\partial T}{\partial z} = \frac{1}{r}\frac{\partial}{\partial r}\left(k\frac{\partial rT}{\partial r}\right) + \frac{\partial}{\partial z}\left(k\frac{\partial T}{\partial z}\right) + Q_{in} \tag{3.42}$$

Where

- k is thermal conductivity function of temperature
- Q_{in} heat input
- T is temperature
- C_p heat capacity

The temperature profile is critical because all of the physical properties (μ, ρ, k, D_{ab}) in the model are sensitive to the temperature (temperature dependent). Hence, any change in temperature should be taken into consideration.

3.4 Boundary Conditions and Model Solution

The transport models (Species Transport, conservation of momentum, and conservation of energy) are solved simultaneously using computational fluid dynamic (CFD) packages in COMSOL. These packages are used to grid the sample tube side in the heat exchanger into meshes and apply the model with boundaries on each mesh resulting in temperature, velocity, and weight fraction of asphaltenes profiles. Fig. 3.2 shows a simplified schematic of the tube side in the heat exchanger with the coordinates (cylindrical system) and the model's boundary conditions. All balance equations are second order unsteady state two-dimensional differential equations. These facts

mean each equation needs an initial condition and four boundary conditions, two for each dimension.

For the Species Transport (Asphaltenes Balance), the initial condition is the initial Asphaltenes concentration which was measured by SARA analysis. The same condition is also the first boundary condition in the z-direction at z=0. At z=∞, $\delta w_a/\delta z$ equals zero. At r=0, $N_{ar} = k_a \rho_a \frac{dR_f}{dt}$

For the momentum balance, the initial condition is the inlet velocity of the crude in the tube. For the z-direction at z=0. The first boundary condition is the inlet velocity of the crude in the pipe. The second boundary condition is at z=∞ (very far end of the tube) where the velocity will be fully developed and $\delta V_z/\delta z$ is zero. For the r-direction, the first boundary condition is be $V_{z,max}$ at r=0 (middle of the tube) and the velocity at the surface is zero assuming no slip conditions due to the rough inner surface of the pipe.

For the energy balance at t=0 the temperature is the inlet temperature of the crude which is also the temperature at z=0. At z=∞, $\delta T/\delta z=0$. At the surface r=R, $\delta T/\delta r=f(t,z)$. where f(t,z) is going to be function of time and temperature due to change of the overall heat transfer coefficient because of the Asphalenes precipitation process. And at r=0, $\delta T/\delta r=0$.

3.5 Model Setup

3.5.1 Space Dimension

The space dimension that was selected for the problem is 2D axisymmetric; hence, all the changes in the tube are in z and r dimensions and no changes in the θ dimension. This is a problem where 3D geometry can be constructed by revolving a cross section about an axis, and no variations in

any variable occur when going around the axis of revolution an axisymmetric physics interface can be used.

The spatial coordinates are called r and z, where r is the radius and z is the length. The flow at the boundaries is given per unit length along the third dimension. Because this dimension is a revolution, all flow must be multiplied with αr, where α is the revolution angle (for example, 2π for a full turn). COMSOL provides this as an option during post processing. Figure 3.2 illustrates the 2D axisymmetric space dimension

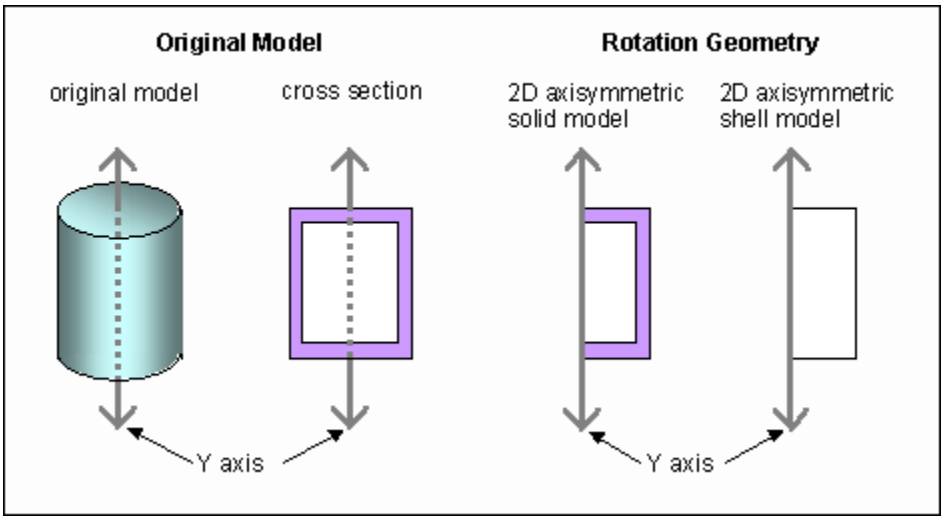

Figure 3.2: 2D axisymmetric space dimension

3.5.2 Physics

3.5.2.1 Non-isothermal flow

This physics describes fluid flows with temperatures that are not constant. When a fluid is subjected to a temperature change, its material properties, such as density, viscosity, thermal conductivity, heat capacity, and diffusivity change too.

In some situations, these changes are large enough to have a substantial influence on the flow field. And, because the fluid transports heat, the temperature field is, in turn, affected by changes in the flow field. This two-way coupling between fluid flow and heat transfer is a phenomenon that is prevalent in heat exchangers, chemical reactors, atmospheric flows, and processes in which components are cooled.

3.5.2.2 Transport of Concentrated Specie

The Transport of Concentrated Species interface is used to study gaseous and liquid mixtures where the species concentrations are of the same order of magnitude and none of the species can be identified as a solvent. In this case, properties of the mixture depend on the composition, and the molecular and ionic interaction between all species need to be considered. The physics interface includes models for multicomponent diffusion, where the diffusive driving force of each species depends on the mixture composition, temperature, and pressure.

The physics interface solves for the mass fractions of all participating species. Transport through convection, diffusion, and migration in an electric field can be included.

The default transport mechanism is the convection and diffusion node, which is dynamic and derived from the transport mechanism activated in this physics interface.

3.5.3 Geometry

Under a geometry node, the geometry sequence for the model physics are created. The geometry that was selected for this package is a simple rectangle to present the tube where the flow of crude oil takes place. Figure 3.3 shows the build of the selected geometry where the length of the selected tube is 10 m and the radius is 0.05 m.

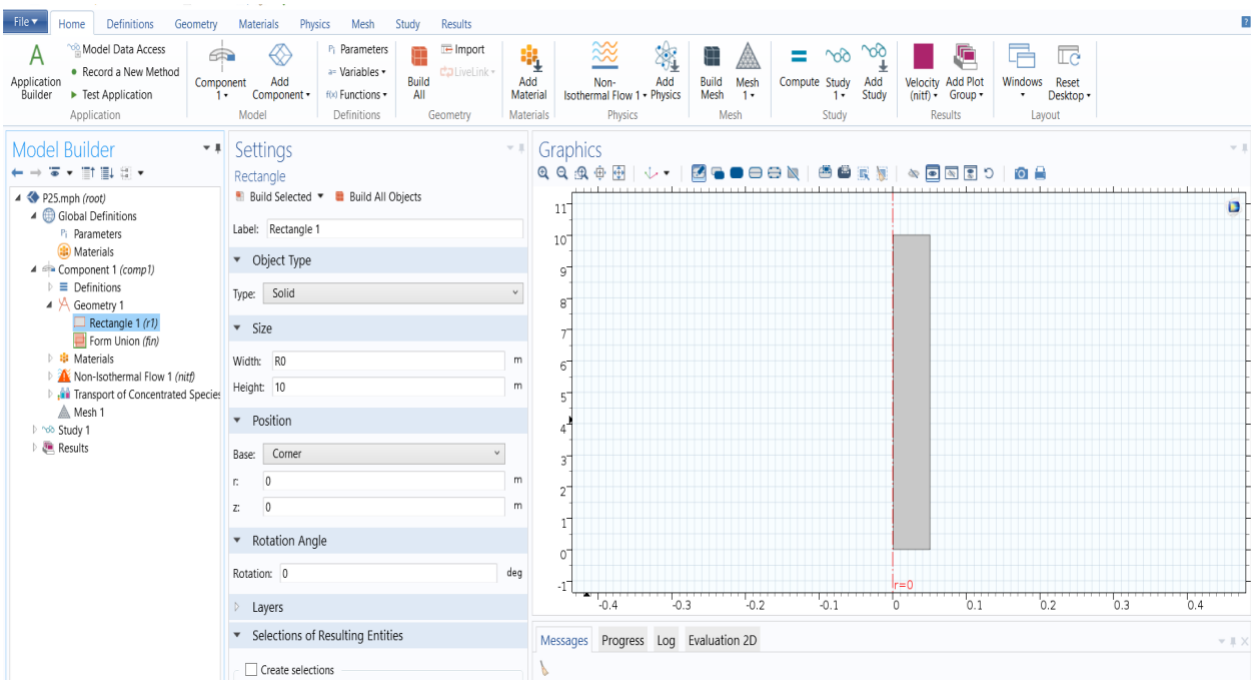

Figure 3.3: Model Geometry.

3.5.4 Material

The material column lists the current materials in the component using the materials' node labels from the model tree according to the settings defined in Displaying Node Names, Tags, and Types in the Model Builder. To simplify things for the model, two materials were added in the package: crude oil and asphaltenes. The properties of each material were added as a dependent that will be described in chapter 4.

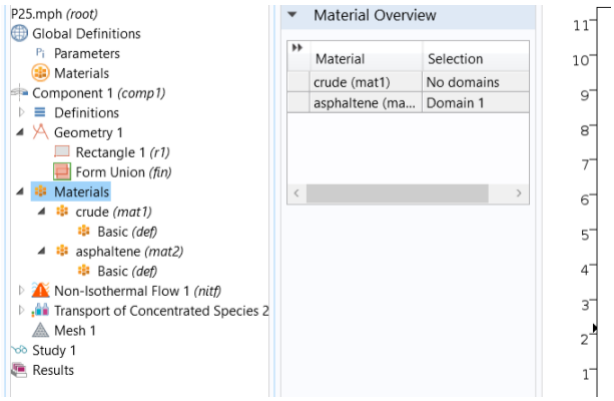

Figure 3.4: Material selection and construction.

3.5.5 Mesh

Upon adding new component to the package, COMSOL sets the default mesh in the sequence mesh. The selected mesh was set to be very coarse to save the computation time and depends on the selected physics of the problem as shown in Figure 3.5. The selected geometry that was selected to start testing the model was set to be the inside of a 10 m long tube with a diameter of 10 cm (0.1) m. The total points to be solved in the mesh was 116362 points distributed along the z axis and the r axis as show in tables 3.2 and 3.3, respectively.

Table 3.2 Mesh frequancy distribution in the z axis

	Frequency	Percent	Cumulative Percent
z=0	44	0.04	0.04
0<z<1	11593	9.96	10.00
1<z<2	11592	9.96	19.96
2<z<3	11643	10.01	29.97
3<z<4	11633	10.00	39.97
4<z<5	11591	9.96	49.93
5<z<6	11663	10.02	59.95
6<z<7	11639	10.00	69.95
7<z<8	11597	9.97	79.92
8<z<9	11649	10.01	89.93
9<z<10	11674	10.03	99.96
z=10	44	0.04	100.00

Table 3.3 Mesh frequancy distribution in the r axis

	Frequency	Valid Percent	Cumulative Percent
0	2176	1.87	1.87
0.00<r<0.01	3204	2.75	4.62
0.01<r<0.02	4341	3.73	8.35
0.02<r<0.03	8368	7.19	15.55
0.03<r<0.04	29141	25.04	40.59
0.04<r<0.05	67719	58.20	98.79
0.05	1409	1.21	100.00

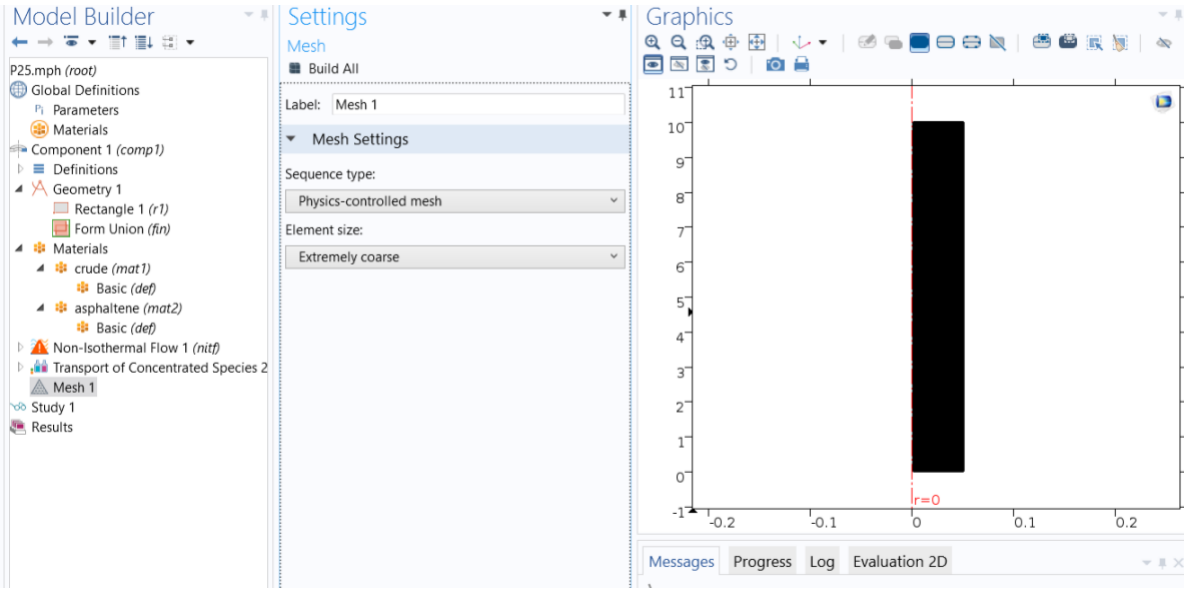

Figure 3.5: Mesh selection.

3.6 Targeted Output of the Model

The primary objective of the model is to show the asphaltenes concentration profile in the tube side of the heat exchanger. It is predicted that the model shows a rate of Asphaltenes concentration

reduction. This reduction is going to describe the rate of Asphaltenes precipitation. Other outputs of the model are the velocity and temperature profile such as shown in figure 3.6.

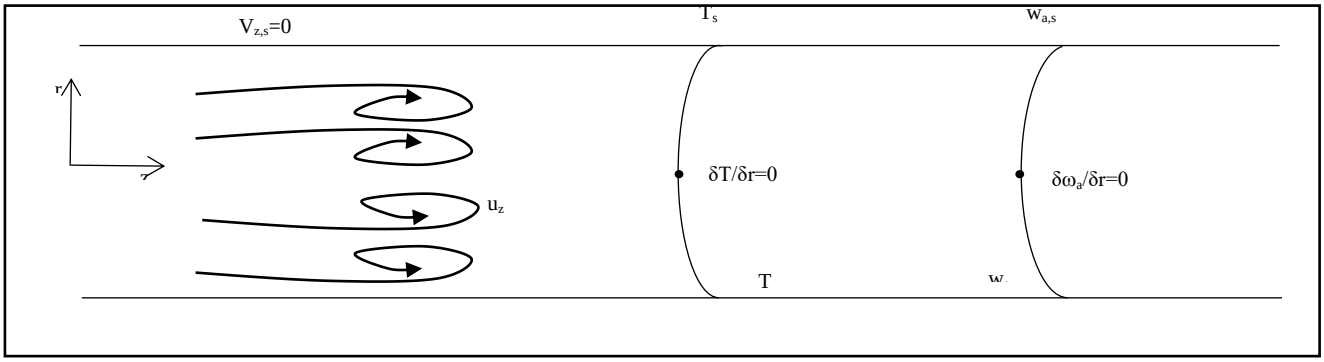

Figure 3.6: Simplified schematic of the tube side in the heat exchanger with the coordinates (cylindrical system) and the models boundary conditions

3.7 Requirements to be prepared for model application

In Chapter 4 all the physical properties of the model will be derived in detail.

Chapter 4: Physical Properties Calculation and Estimation

This chapter focuses on the physical properties of asphaltenes and crude oil that are needed for the model. Physical properties will be derived in detail. Experimental methods that were performed to obtain the properties will be explained and discussed in section 4.2 and 4.3. In section 4.4 will discuss the correlation obtained to calculate viscosity and density for momentum balance [93]. Section 4.5 will discuss the asphaltenes properties which will be needed such as density and thermal conductivity which are needed for energy transfer and species balance. Section 4.6 will represent an approach to estimate the diffusivity of the asphaltene in oil system. Finally, section 4.7 will explain by a case study a method to estimate the thermal conductivity of crude oil.

4.1 Introduction

Crude oil is classified based on different properties, such as molecular weight, viscosity, density, and API gravity. Heavy crude oil is crude oil with API gravity less than 20. Taking reliable viscosity and density measurements is difficult, especially for oil. These properties must be evaluated precisely for input to the numerical simulations. Determining the viscosity and the density of dead oil is more straight-forward using empirical correlations at temperatures other than the reservoir temperatures [94]. These dead oil data can be used as the starting seed point for live oil viscosity and density predictions. The live oil data is rare due to the difficulty and high costs of viscosity and density measurements at reservoir conditions.

Additionally, viscosity and density are essential parameters required for numerical simulations to determine the economics of the Enhanced Oil Recovery (EOR) project. Consequently, a correlation must estimate these values under different temperatures [95]. The viscosity of crude

oil depends on many things, one of them is the source chemical composition [96]. Therefore, developing a representative viscosity model to include different regions of the world seems to be a very challenging task.

This chapter contains the crude samples preparation for properties measurements such as true boiling point, density, and viscosity. About 30 different Kuwaiti crudes were tested, (samples' details are shown in Appendix A) some properties were measured in Kuwait University laboratories, others were collected from the source where crudes came from. Other properties are estimated based on critical pressure and temperature for crudes and asphaltenes. Almost all crudes had SARA analysis (Saturates, aromatics, resins, and asphaltene) in which the weight percentage of asphaltene was known for each crude. Elemental analysis, for crudes and asphaltene, is done to estimate properties.

4.2 Experimental Methodology for Properties Determination

4.2.1 Sample Preparation

Samples of dry heavy crude oil from Kuwait Oil company were collected in specially designed 2.5-L glass stoppered bottles and were stored at below 20°C. The crude oil samples were mixed with an emulsion breaker (commercial-grade Nalco demulsifier), centrifuged (100 rpm) to remove the traces of necessary sediments and water (BS&W), and finally, the samples were maintained in an oven at 40°C. Before the analysis, each sample was shaken vigorously using open-air platform shakers to achieve homogeneity. As soon as the bottles were opened, the water contents of the samples were measured with a Metrohm KF (model 832-Thermoprep), and the moisture content range was measured to be between 1×10^{-3} and 5×10^{-3} $g\cdot g^{-1}$.

4.2.2 Density and Viscosity Measurements

After the crude samples were prepared as discussed in section 4.2.1, the dynamic viscosity, μ, of 30 dead crude oil samples in the temperature range from 20 °C to 160 °C was determined using an electromagnetic viscometer (Figure 4.1). The viscometer consists of two coils that move the piston back and forth magnetically with a constant force. Proprietary circuitry analyzes the piston's two-way travel time to measure the absolute viscosity. The instrument was calibrated by measuring in triplicates the three reference samples, N600, N2000, and N4000, supplied by Canon Instruments. The calibration was done for the temperature range of interest with reproducibility of ±0.95%. The estimated uncertainty of the dynamic viscosity for all the measured ranges was not more than 9×10^{-3} mPa·s at a 95% confidence interval.

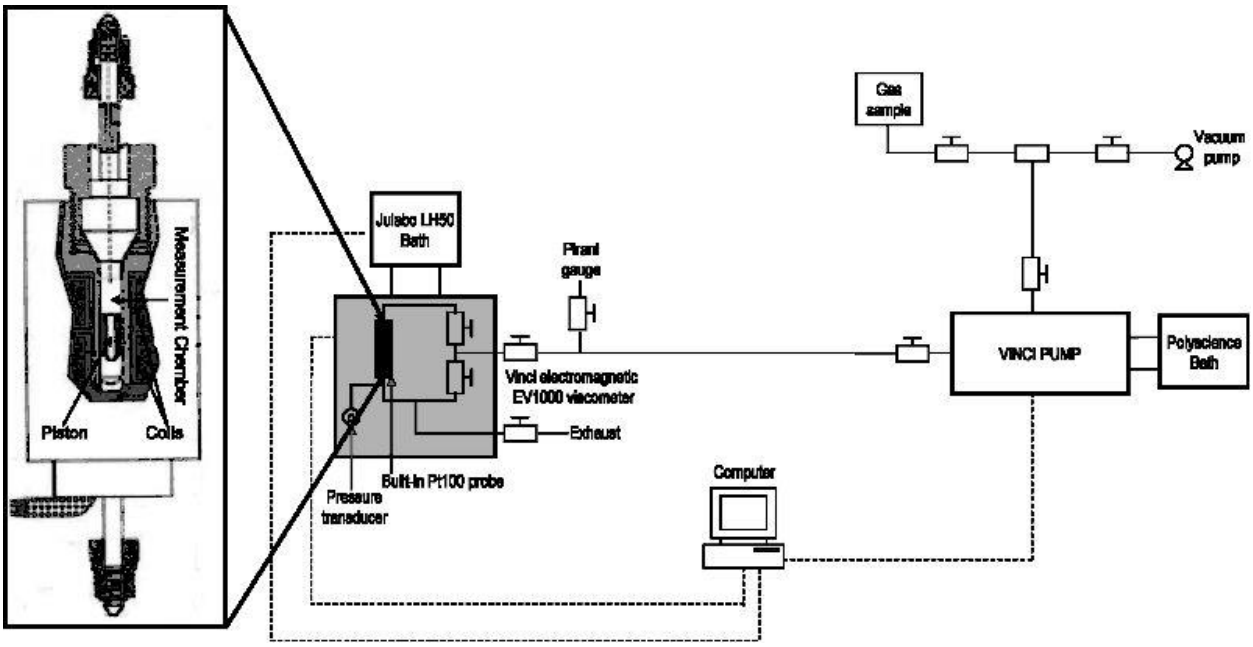

Figure 4.1: Electromagnetic Viscometer (EV 1000) [97]

The densities of crude oil samples were measured at temperature intervals between 20 and 160 °C using an oscillating U-tube densitometer; the oscillation period (τ) in the vibrating U-tube of the densitometer was converted to density (ρ) using equation 4.1 [93, 97].

$$\rho = A\tau^2 - B \tag{4.1}$$

The apparatus constants (A and B) were determined by using the density of dry air and ultrapure water at the temperature of interest. The temperature of the measuring cell is controlled using two integrated measuring sensors (Pt100) with a temperature reproducibility of ±10-2 °C. The calibration was done at the temperatures of interest by using ultra-pure water. Triplicate density measurements were performed for all the samples. The results were averaged, and the estimated uncertainty of the measurements was within 0.5 $kg \cdot m^{-3}$. Specific gravity for liquid oils is defined as:

$$SG_{liq} = \frac{\rho_{liq}}{\rho_{water}} \tag{4.2}$$

Where ρ_{liq} is oil density and ρ_{water} is water density.

Both densities of oil and water are at some standard temperature and pressure. These standard conditions for the specific gravity of petroleum liquids are 1 atm (14.7 psi) and 15.6 °C (60 °F). Since under the same conditions, most petroleum fractions are lighter than water $SG \leq 1$

Another parameter for oil density is API gravity defined as:

$$API = \frac{141.5}{SG} - 131.5 \tag{4.3}$$

Heavy oils have low API, and light oils have high API gravities.

Before each test, all instruments were calibrated according to the manufacturer's specifications. As per the test procedures, triplicate measurements were performed, and the average was used. Descriptive statistics of the tested samples (API, temperature, viscosity, and density) are shown in Table 4.1.

Table 4.1 Descriptive statistics of the 376 experimental data points of the 30 samples.

	API $_{60°F}$	T (°C)	μ (cP)	ρ (g/cm^3)
Mean	16.1	81	281.2	0.9
Standard Error	0.1	4.1	52.9	0.0
Standard Deviation	1.8	79	$1.0x10^3$	0.03
Sample Variance	3.4	6366	$1.0x10^6$	$1.0x10^{-3}$
Minimum	11.7	20	1.7	0.8
Maximum	18.8	160	$1.1x10^4$	1.0

4.2.3 True Boiling Point (TBP) Determination

Ten dead oil samples out of the 30 samples under study were selected that covered the entire range of API values. The TBP distillation was carried out in the AUTODEST 800 Fisher GmbH backed column, equivalent to 15-trays according to ASTM D 2892 for the test exposed to the atmosphere and according to ASTM D 5236 for the test under vacuum. The TBP distillation was performed at a pressure drop ranging from 760 to 2 mmHg with a reflux ratio of 1:5. The specific gravity at 60°F, API gravity, dynamic viscosity, and true boiling point for each fraction were measured as shown in Tables 4.2 and 4.3.

Table 4.2: TBP distillation range (average TPB) of 10 crude oil samples according to ASTM D2892 and ASTM D5236.

Sample	5%	12%	20%	32%	40%	50%	61%	69%	80%	90%	Residue
	Distillation Temperature, °C										
Average	117	154	204	257	297	354	440	500	553	642	687

Table 4.3: Average properties of the different pseudo-components of 10 crude oil samples.

	API60°F	Tb (°C)	SG
average	16.6	374.9	0.95

4.3 Asphaltene Content

4.3.1 SARA analysis

Asphaltenes were extracted from each bitumen as Unwashed asphaltenes contain resins and non-asphaltenic solids that co-precipitate with the asphaltenes. Asphaltenes free of resins and other solids were desired so that properties of "pure" asphaltenes could be measured. To obtain resin-free asphaltenes; the unwashed asphaltenes were washed with n-heptane in a Soxhlet apparatus. To obtain solids-free asphaltenes; the Soxhlet-treated asphaltenes were dissolved in toluene, and the solution was filtered through Whatman #2 filter paper. The filtrate was evaporated until only dry "solids-free" asphaltenes remained. Note that a small number of fine solids were likely to remain in the "solids-free" asphaltenes. Saturates, aromatics and resins were extracted according to ASTM D2007M. With this method, asphaltenes were first extracted from the bitumen with n-pentane. The de-asphalted oil (maltenes) is mixed with n-pentane and introduced into a liquid chromatography apparatus consisting of an upper column containing Attapulgus clay and a lower column containing silica gel. The resins are adsorb on the clay, the aromatics are adsorb on the

silica gel, and the saturates pass through. The columns are then separated, and the resins are desorbed with a mixture of toluene and acetone while the aromatics are desorbed with a mixture of n-pentane and toluene. The SARA analysis and solids-free asphaltene content of the four bitumen/heavy oils are reported in Table 4.4.

As discussed later in section 4.5, the asphaltene density and solubility parameter correlated to the molar mass of asphaltene monomers since asphaltenes are assumed to consist of aggregates of monomers.

Table 4.4: Typical SARA analysis of selected crudes

	Asphalt	Resin	Aromatics	Saturates
Mean wt%	11.81	24.58	43.42	19.19
Minimum wt%	1.74	8.67	8.67	8.67
Maximum wt%	25.49	36.07	60.08	44.13
Number of samples	44			

4.3.2 Elemental Analysis

Elemental analysis (Carbon wt%, Hydrogen wt%, Nitrogen wt%, Sulfur wt% and Oxygen wt%) for asphaltene was performed on a Vario MICRO cube manufactured by Elementar, Germany, calibrated with a suitable standard (e.g. sulfamethazine and acetanilide) according to ASTM D5291 method (General Facility Laboratory at College of Engineering Project GE03/08). Infrared spectra (KBr disc) were recorded on Nicolet is10 (FT-IR) by mixing with dry KBr, and the spectra were acquired relative to a pure KBr reference. Gel Relative Molar Mass was measured for asphaltene using Gel Permeation Chromatography (GPC) on Waters 600 system with 410

Refractive Index detector manufactured by Waters, USA, at where the asphaltene sample was calibrated with polystyrene using tetrahydrofuran (THF) as a mobile solvent. ESIMS spectra were carried out using the Thermo LCQ Fleet –Ion trap LCMS, with spray voltage 5.40 kV and Capillary temperature of 350°C with a capillary voltage of 11V.

To calculate the density of the asphaltene sample; different weights of asphaltene were dissolved in toluene. GC-MS DFS; Thermo, Germany was served in the analysis of the contained hydrocarbons in C7+ crude oil. Gas Chromatograph used for the analysis is Trace GC Ultra equipped with TR-5 (Thermo) – Capillary column (Length: 30 m; Internal Diameter: 0.25 mm; Film Thickness: 0.25 um). Helium is used as a carrier gas with a flow rate of 0.8ml/min. Injector Temperature kept constant at 280ºC. Column Ramp: Initial Temp - 60ºC (Hold time: 1min); Ramp1: 1 ºC/min till 80 ºC (Hold time: 3min); Ramp2: 10 ºC/min till 250 ºC (Hold time: 5 min); Transfer Line Temperature was 280 ºC. Mass Spectrometer Conditions: Mode: Electron Impact Ionization; Electron Energy (70.1 eV), Emission Current (1 mA), Source Temperature (175 °C), Filament Current (2.80 A), Scan Range (50 – 600 Da), Mass Analyzer: Magnetic Sector and Mass Detector: Electron Multiplier. Table 4.5 and Table 4.6 lists a typical elemental analysis of asphaltene and typical crude composition analysis, respectively, for selected crudes.

Table 4.5: Typical elemental analysis of asphaltene [98]

Carbon	Sample 1	Sample 2
Carbon	85.8 wt %	89.0 wt %
hydrogen	9.2 wt %	5.8 wt %
Sulfur	4.2 wt %	3.8 wt %
Nitrogen	0.95 wt %	1.30 wt %
Molecular weight	1763- 1790 wt %	959- 980 wt %

Table 4.6: Typical Crude Composition Analysis

Component	Wt%	Component	Wt%
C1	0.00	C14	1.59
C2	0.00	C15	1.75
C3	0.00	C16	1.36
C4	0.01	C17	1.15
C5	0.03	C18	1.04
C6	0.01	C19	0.92
C7	0.05	C20	0.71
C8	0.15	C21	0.58
C9	0.57	C22	0.57
C10	1.08	C23	0.44
C11	1.63	C24	0.35
C12	1.87	C25	0.33
C13	2.09	C26+	81.72
MwC26+	451.7		
SGC26+	0.98		
Bulk Mol.	330.7		
SG	0.94		

4.4 Properties for Momentum Balance

The experimental data of the viscosity and the density of 30 dead heavy oil samples with different API values were measured in the temperature range of 20 °C to 160 °C. These values were subjected to a simple statistical analysis to assess the distribution of the data points (Table 4.1). The correlation coefficients were estimated to determine and to evaluate the strength of the dependence between each of these two variables. The correlation coefficient for viscosity–density is positive, whereas the coefficient for viscosity-temperature is negative (Table 4.7). Thus, the viscosity is directly proportional to density and inversely proportional to temperature, with a high correlation between the data. The ASTM indicates that dead oil viscosity is labeled according to its standard API at 15.5 °C. The API value is the first parameter for any model, and the second parameter is the value of the measured temperature. According to literature reviews, most of the models are based on an intermediate parameter or sometimes two parameters, the API and

temperature, to calculate the viscosity [94, 99, 100]. Therefore, the real physical property was selected as the intermediate parameter, such as density, and the density was modeled using API and temperature. The goal was to create models in the following formats for the density and viscosity predictions.

$$\rho_{oil} = f\left(T, API_{@60^oF}\right) \tag{4.4}$$

$$\mu_{oil} = f\left(T, \rho_{oil}\right) \tag{4.5}$$

Table 4.7: Correlation factors between API, T, μ and ρ.

Designation	API 60°F	T	μ	ρ
API 60°F	1			
T	0.90	1		
μ	-0.24	-0.90	1	
ρ	-0.75	-0.93	0.85	1

4.4.1 Empirical Correlations for Density

The first challenge was to develop a unified model of a set of parameters for the entire range of dead crude oil density with only one equation. Curve fitting by regression methods of the experimental density data concerning the standard ^{o}API gravity and temperature was applied. The results were acceptable and well fit by an equation of the following form:

$$\rho_{od} = \bar{a} + \bar{b}\left(API_{60^oF/60^oF}\right) + \bar{c}\left(T\right), \tag{4.6}$$

The values of $\bar{a}, \bar{b}\ and\ \bar{c}$ are 1.072, -0.00653, and -0.000664, respectively, with a regression coefficient (R^2) of 0.98. Statistical analyses were conducted randomly for 376 data points of the 30 dead crude oil samples. The results based on these numbers were divided between training and

testing parts in a ratio of 3:1. Training and testing data were selected by assigning a random number to each data point and then selecting 75% of the points with highest random numbers for training and the remaining 25% of the points with the lowest random numbers for testing

Fluid densities have been estimated using the Standing and Katz [101] method, with n correction factors. The correction factor $\Delta\rho_p$ is the change in density due to the effect of pressure on the oil, and $\Delta\rho_T$ is the change in density due to the thermal expansion of oils as described in Equation 4.7 [96, 102].

$$\rho = \rho_{sc} + \Delta\rho_p + \Delta\rho_T \tag{4.7}$$

$$\Delta\rho_p = \left[0.167 + (16.181)10^{0.0425\rho_{sc}}\right]\left(\frac{P}{1000}\right) \tag{4.8}$$

$$\Delta\rho_T = \left[0.013 + 152.4\left(\rho_{sc} + \Delta\rho_p\right)^{-2.45}\right]x\left(T - 520\right) - \left[8.1\left(10^{-6}\right) - (90.06)x10^{-0.764\left(\rho_{sc} + \Delta\rho_p\right)}\right]\left(T - 520\right)^2 \tag{4.9}$$

where ρ, P, T, and ρ_{sc} are density, pressure, temperature, and density at standard conditions of crude oil, respectively, according to Standing's relationships.

The pressure correction factor was neglected because all the measurements were done on dead oil samples under normal pressure. The reliability and accuracy of the data from the density measurements were checked by comparing the experimental values with the predicted values using:

- standing density model (Equation 4.7)
- the proposed density model (Equation 4.6).

The results were satisfactory with an R^2 of (0.98 and 0.99) and an average absolute error (ε) of 0.61% and 0.04%, respectively, as shown in Figure 4.2 and 4.3

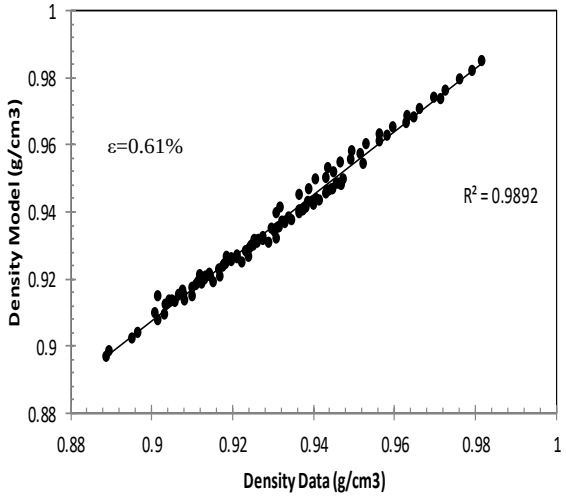

Figure 4.2: Relationship between experimental density and the Standing model

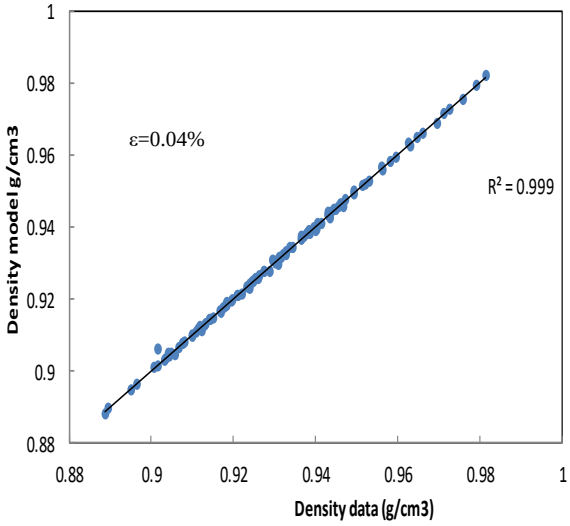

Figure 4.3: Relationship between experimental density and the proposed model

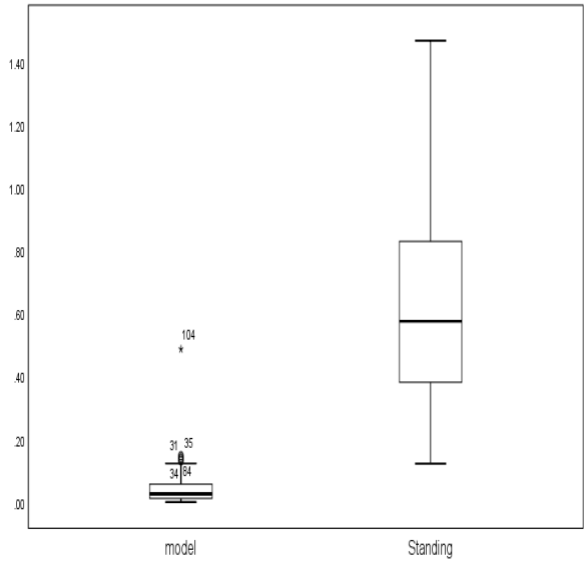

Figure 4.4: Error bars for calculated densisty once using the density model (equation 4.6) and using Standing model [96, 102] (euqation 4.7)

Another way of evaluating the density model is by applying the cubic equation of state that was developed by Peng and Robinson [103].

$$P = \frac{R_g T}{v-b} - \frac{a(T)}{v(v+b)+b(v-b)} \tag{4.10}$$

This equation can also be written using the compressibility factor (Z).

$$Z^3 - (1-B)Z^2 + (A - 3B^2 - 2B)Z - (AB - B^2 - B^3) = 0 \tag{4.11}$$

The parameters (a) and (b) in Equation 4.10 are calculated by applying the equation at the critical point.

$$a(T_c) = \alpha \frac{R_g{}^2 T_c{}^2}{P_c} \tag{4.12}$$

$$b(T_c) = \beta \frac{R_g T_c}{P_c} \tag{4.13}$$

$$a(T) = a(T_c)\left(1 + m\left(1 - T_r^{1/2}\right)\right)^2 \tag{4.14}$$

$$b(T) = b(T_c) \tag{4.15}$$

$$m = 0.37464 + 1.54226\omega + 0.26992\omega^2 \tag{4.16}$$

The value of α is 0.45724, and the value of β is 0.0778, and these values can be empirically tuned for better results. The values of critical parameters (P_c, T_c, and ω) are calculated using the correlations developed in the literature [104]. The average of the pseudo-component for each group of hydrocarbons in each distillation range was calculated. Besides, the sample mid-true boiling points at 20, 50 and 80% distilled were determined (Tb), as shown in Table 4.2. After calculating the compressibility factor (Z), the molar volume was calculated, and this value was then converted to density using the molecular weight. After tuning the EoS parameters, the average error was successfully dropped to 2.3%, compared with 22.5% before tuning.

4.4.2 Viscosity Model

Several correlations for predicting dead oil viscosity are available in the literature. Some of these models are discussed in this section, such as the Beggs and Robinson [105] model for temperatures ranging from 21 to 146 °C and the Elsharkawy and Alikhan [106] model based on crude oil samples from the Middle East for temperatures ranging from 38 to 150 °C. Naseri et al.[107] presented a model for temperatures ranging from 40 to 146 °C. Other authors suggest that the variation in compositions is why correlating the viscosity of heavy crude with high accuracy is

improbable (Beal [108]). Beal created a chart that described the viscosities of 655 dead oil samples at 38 °C, representing 492 oil fields around the world and covering viscosities ranging from 0.8 to 155 cP, gravities ranging from 10.1 to 52.5 °API and temperatures from 38 to 105°C. Besides, Kartoatmdjo and Schmidt [109] developed an empirical correlation to predict the viscosity of dead oil with 3588 data points from 661 dead oil samples that covered gravities ranging from 14.4 to 58.9 °API, viscosities ranging from 0.5 to 682 cP and temperatures ranging from 75 to 320°F. Labedi [110] also correlated the dead oil viscosity in the range of 0.66 to 4.79 cP and gravity in the range from 32.2 to 48.0 °API as a function of API gravity and temperature covering the range from 38 to 152 °C. Using 91 data points, Labedi [110] claimed that his equation was more accurate than previous efforts [108] and [105], which might have been correct for this tight viscosity range; however, significant errors were observed when this model was applied outside of these temperature, viscosity, or °API ranges. Hossain et al. [111] statistically analyzed a data bank covering the dead oil viscosity range of 22 to 415 cP and the temperature range of 51 to 93°F for oil samples with gravities in the range of 15.8 to 22.3 °API.

Before developing the new viscosity model, understanding the relationship between the input and output variables is essential; specifically, identifying which parameters are insignificant and can be eliminated from the final model and the parameters that are highly correlated with the output. A sensitivity analysis was performed for the main parameters (viscosity μ, density ρ, and temperature T) for all the experimental data. The negative correlation coefficient between the dynamic viscosity and temperature shows that whenever the temperature is increased, the viscosity decreases, indicating an inverse correlation between them. The relationship between the viscosity and temperature could be described by equation 4.17. The positive value of the correlation factor

between the density and the viscosity indicates a direct correlation, and the equation for these variables follows the form of equation 4.18.

$$\mu_{od}\ \alpha \left(\frac{1}{T^{b}}\right) \tag{4.17}$$

$$\mu_{od}\ \alpha\ c \ln \rho_{od} \tag{4.18}$$

Consequently, the dead oil viscosity (μ_{od}) is a function of the absolute value of reservoir temperature (T) and the crude oil density (ρ). After multiple regression analysis of all the experimental viscosity data, the results show that the following functional form can predict the dead oil viscosity data with an average absolute error of 8% and an R^2 of 0.97:

$$\ln\left(\mu_{od}\right) = a + \frac{b}{T^{2}} + c\left(\rho_{od}{}^{2}\right)\ln \rho_{od} \tag{4.19}$$

The correlation parameters for the normal and high-temperature ranges must be re-evaluated to generalize the prediction ability of the model to represent the whole set of crude oil viscosity data. The data was divided into two sets based on the temperature range. The first set was used with the model for the normal temperature range (20 to 100 °C), and the second set was used for the high-temperature range above 100 °C. The values were evaluated and tested using different techniques, such as curve fitting, nonlinear regression, and the square method. Table 4.8 shows the values for a, b, and c for each section of the data set, where the viscosity is in cP, the temperature is in °C, and the density is in $g \cdot cm^{-3}$.

Table 4.8: Values of the correlation parameters.

Designation	Low temperature (20 to 100°C)	High temperature above 100°C
a	10.8	7.9
b	275.3	309.6
c	107.8	61.5

To check the ability of the proposed viscosity model to present all experimental data, cross plots of the measured and predicted viscosity values were used. The results for the low-temperature region were in good agreement, with the average relative absolute error approximately 8.5%. The training and testing parts also had the same error, as depicted in Figure 4.5. For the high-temperature region, the average relative error was 7% for the training part and 8% for the testing part, as shown in Figure 4.6. The relationship between viscosity and temperature for randomly selected samples with different API values (high, medium, and low) at normal and high temperatures is shown in Figure 4.7.

One of the main challenges in this study is that most of the existing models in the literature are limited to specific ranges of temperature, API value, and viscosity. Some of the data points had viscosity values higher than 10000 cP, whereas the maximum limit for the other models is approximately 600 cP. Ten different models[105-114] were used to determine the capability of these models to predict the experimental viscosity data. Some results showed good agreement with the data, whereas other models had poor predictive capabilities. The primary source of error in each model predictions is perhaps individual limitations and/or the availability of accurate experimental data. Table 4.9 shows a summary of the ten evaluated models with all their data ranges. All the models were used to reproduce the data points regardless of their viscosity, temperature, or API limitations. The model created by Standing in 1947 gave the most acceptable

results among the ten published models. Several approaches were used to compare these models with the proposed model of the data under study. These approaches were (A) squaring the Pearson product moment correlation coefficient, (B) relative error, (C) standard deviation, and (D) cross plots.

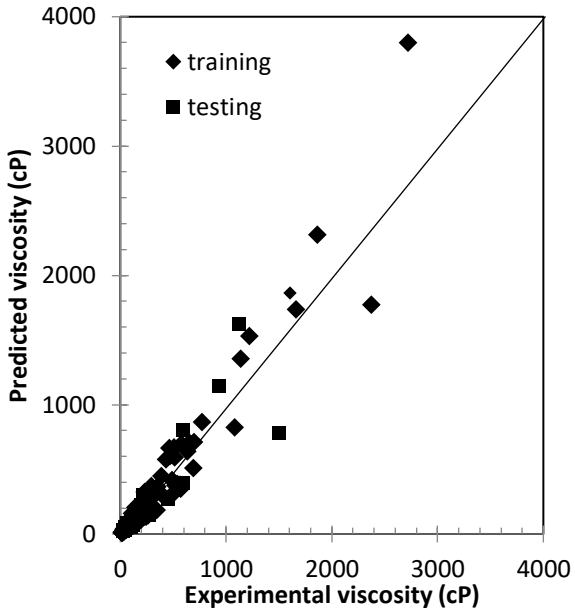

Figure 4.5: Comparison of the predicted and measured viscosities using the low-temperature model (20 °C < T < 100 °C).

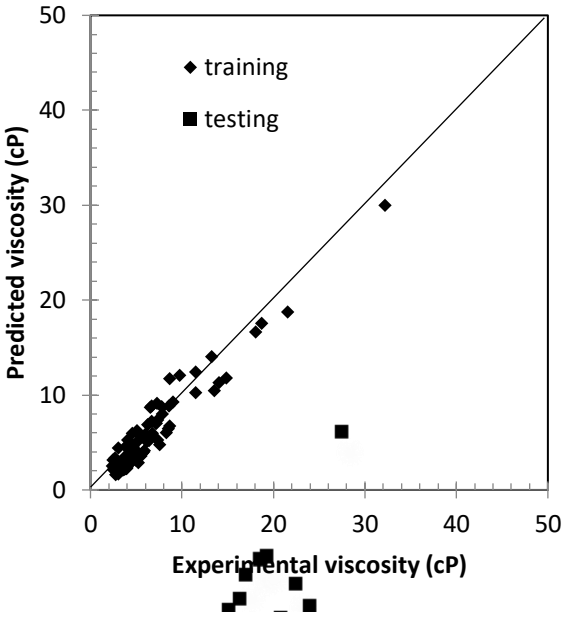

Figure 4.6: Deviation of the experimental from the predictive values using the high-temperature model (T >100 °C).

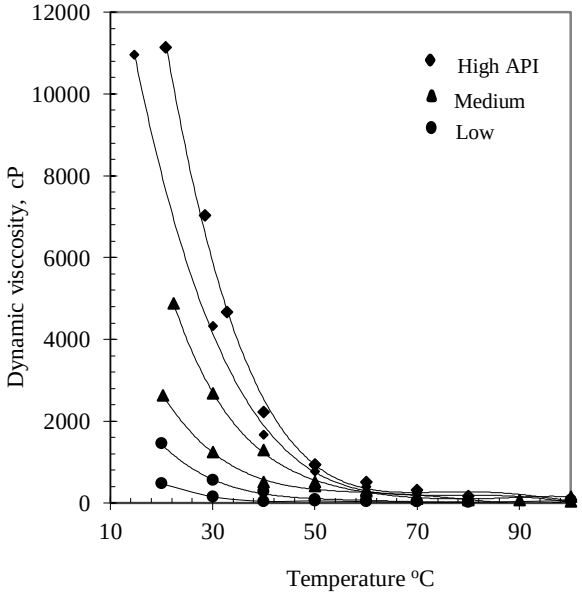

Figure 4.7: Assessment of the measured viscosity data with the proposed models on randomly selected samples with different API values

Table 4.9: Summary of the evaluated models, including the API, temperature, and viscosity limits.

	API $_{60°F}$		Temp. (°C)		μ /(cP)	
Author	low	high	low	high	low	high
This work 2014	11.7	18.8	20.0	160.0	1.7	11322
Naseri, Nikazar et al., 2005	17	44	40.6	146.1	0.75	54
Labedi, 1992	32	48	37.8	152.2	0.6	4.8
Elsharkawy and Alikhan, 1999	20	48	37.8	148.9	0.6	33.7
Beggs and Robinson, 1975	16	58	21.1	146.1	-	-
Beal, 1946	10	52	37.8	104.4	0.8	188
Standing, 1977	10.1	52.5	37.8	104.4	0.86	1550
Gaslo, 1980	20	48	10.0	148.9	0.6	39
kartoatmodj Schmidt, 1994	14	59	26.7	160.0	0.5	586
Petrosky Farshad, 1995	25.4	46.1	45.6	142.2	0.72	10.2
Hossain Sarica 2005	15.8	22.3	51.1	93.3	22	415

In addition, the viscosity was calculated using a transport model that is based on Enskog's theory [115]. The viscosity was calculated as follow:

$$\mu = \mu_0 b'\rho\left[\frac{1}{b'\rho\chi} + 0.8 + 0.7614\left(b'\rho\chi\right)\right] \tag{4.20}$$

where

$$b'\rho\chi = \frac{v}{R_g}\left[\frac{R_g}{v-b} - \frac{1}{v\left(v+b\right)+b\left(v-b\right)}\left(\frac{\partial a\left(T\right)}{\partial T}\right)\right] \tag{4.21}$$

$$b'\rho = \frac{1}{v}\left[b - \frac{1}{R_g}\left(\frac{\partial a\left(T\right)}{\partial T}\right)\right] \tag{4.22}$$

$$\frac{\partial a(T)}{\partial T} = -a(T_c)\left[\frac{m + m^2\left(1 - T_r^{0.5}\right)}{\left(TT_c\right)^{0.5}}\right] \tag{4.23}$$

$$\mu_0 = 0.1\frac{Nh}{v}\exp\left(3.8\frac{T_b}{T}\right) \tag{4.24}$$

Where μ_0 is the dilute gas viscosity, ρ is the molar density, b' is the co-volume, and χ is the value of the equilibrium radial distribution function at a distance equal to the molecular diameter from the center of an individual molecule. The original values of the parameters α and β gave an average error of density more than 90%, but after tuning the parameters and using new values of 0.009, 0.0058 respectively the average error was 80.3%. Another application of the EoS was made, but this time using the Pederson corresponding state with the Peng-Robinson EoS this trial also gave us a very high absolute error with the value of 126%. Consequently, the published EoS theories are not suitable to represent our experimental viscosity data. Figure 4.8 shows a cross plot between the experimental viscosity data and the predicted viscosity using EOS.

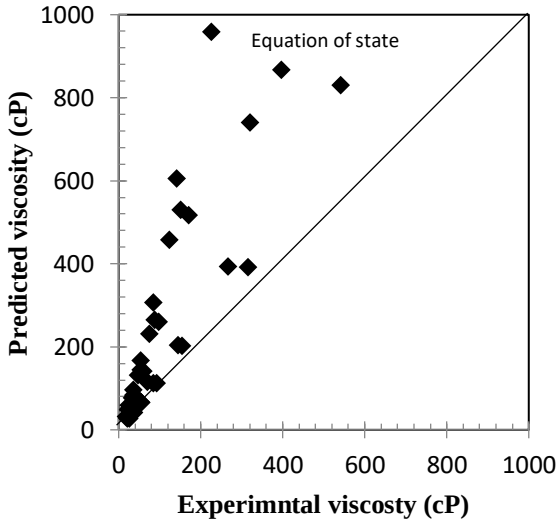

Figure 4.8: Deviation of experimental viscosity data from predictive values

4.4.3 Assessment of Empirical Models for Density and Viscosity

A. First Approach: squaring the Pearson product moment correlation coefficient

Figure 4.9 is a bar chart showing the measured values of the linear regression correlation coefficient, R^2, for all the models. This chart shows the R^2 value of the proposed model with the 10 tested models. The proposed model has the highest R^2 value (0.97), followed by the model proposed by [112] (0.95). Two other models by [111] and [106] have correlation coefficients of (0.91) and (0.89), respectively. The lowest R^2 value, 0.19, is for the model by Labedi [110].

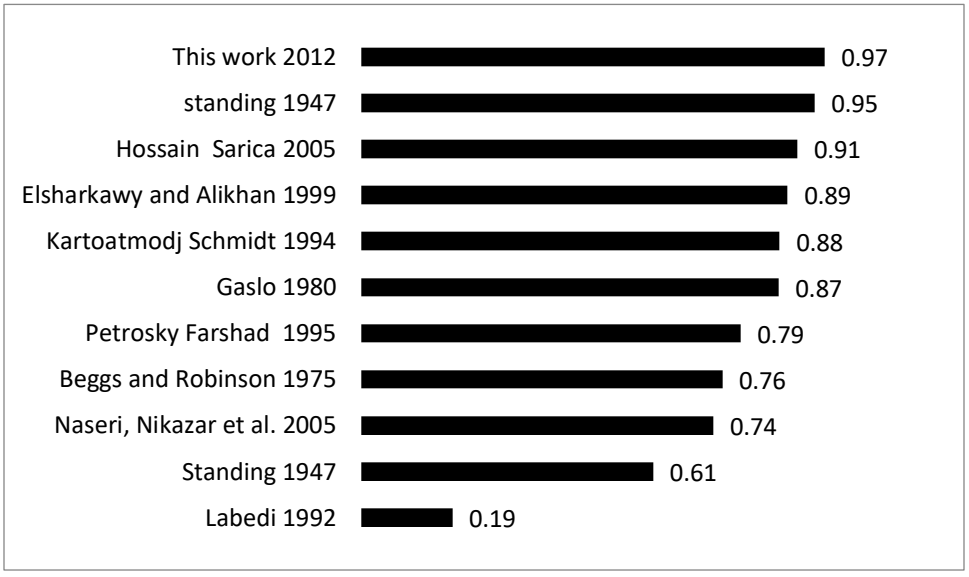

Figure 4.9: Bar chart for the R^2 values for each of the models when applied on our data.

B. Second Approach: relative error

The relative average error test was performed by calculating the absolute percent error between the calculated and the measured value using the following expression.

$$\varepsilon = \left| \frac{Measured - calculated}{Measured} \right| \times 100 \qquad (4.25)$$

The average values of the absolute errors are shown in Table 4.10 and the distribution of the errors for all the models is shown in Figure 4.10. This distribution shows how this work is the best representative of the studied data with the tightest error distribution. By contrast, the other models have a very wide distribution, which indicates that these models can be applied to these data only within the limitations of each model.

C. Third Approach: standard deviation

Another statistical test was performed on the data and the models; a measure of the standard deviation (SD) was performed between the experimental and calculated data with Equation 4.26:

$$SD = \sqrt{\frac{\sum_{i=1}^{n} \left(\hat{\mu}_i - \mu_i \right)^2}{n - p}} \quad , \tag{4.26}$$

where $\hat{\mu}_i$, μ_i, n, and p are the experimental, predicted values of dynamic viscosity, the number of data points, and the number of parameters, respectively. Table 4.10 shows that the proposed model has the lowest mean absolute percentage error (MAPE) and standard deviation (SD), while the results of the other models were not acceptable, especially when the viscosity was above 1000 cP.

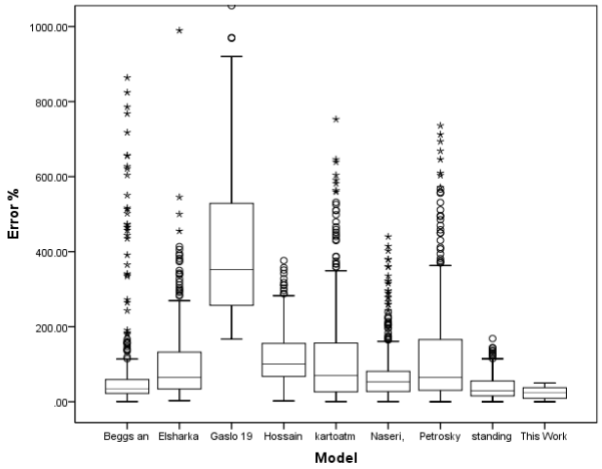

Figure 4.10: Percentage error distribution on all the data points. Beal and Labedi were excluded from this figure due to the high error values.

Table 4.10: Mean absolute percentage error (MAPE) and standard deviation (SD)

Model designation	MAPE	SD
(Standing, 1947)	39.8	220.0
(Naseri, Nikazar et al., 2005)	76.0	219.5
(Beggs and Robinson, 1975)	76.8	2158
(Elsharkawy and Alikhan, 1999)	99.5	1043
(Hossain Sarica, 2005)	119.0	1058
(kartoatmodj Schmidt, 1994)	123.0	1073
(Petrosky Farshad, 1995)	125.4	932
(Gaslo, 1980)	458.8	220.7
(Beal, 1946)	6420.6	666.4
(Labedi, 1992)	2883.6	908.9
(This work, 2014)	8.0	203.7

Although Crude oils of widely varying compositions can have the same gravity, significant errors may be introduced when the viscosities of heavy oils are estimated from general viscosity trends and the API gravity. This viscosity model is a function of the absolute value of reservoir temperature (T) and the crude oil density (ρ) which are more valuable and simpler to use. Good

results of the proposed density model at normal and elevated temperatures could be observed with the average absolute error (ε) of 0.04% and the coefficient of determination R^2 of (0.99). Several empirical models for estimating the viscosity of dead oils were evaluated using dynamic viscosity data of crude oils from the reservoirs of the Middle East. Most of the published models for predicting the dynamic viscosity dead oils are unreliable in a wide temperature range. The assessment of the agreement between the experimental viscosity data and the predicted values indicates that the proposed model successfully represents the experimental data with an average absolute relative error of less than 8% and coefficients of determination R^2 of 0.97 and 0.92 at normal and high temperature, respectively. From statistical analysis, the proposed model was demonstrated as one of the best models in comparison with other models published in the literature. The overall result shows that it is tough to generalize a viscosity model using only API and temperature as an input for that model. This new model is easy to use, provides fair accuracy and precision over a wide range of oil gravities, and could be used to predict better outcomes in future works.

4.5 Estimation of Asphaltene Properties

Most of the crudes under study, the true boiling point, and density were measured. Therefore, the crude critical properties were estimated base on these two factors. The correlation for these properties is as follows [116]:

$$\xi = \xi_{\infty} - \exp(a - bM^{C}) \qquad (4.27)$$

where ξ can be any one of the properties mentioned in Table 4.11. M is the molecular weight and ξ_{∞} is the limiting value for any property as $M \rightarrow \infty$. This generalized equation can be used to calculate the following properties given the molecular weight. The properties are:

- T_b, the mean average boiling point, K
- SG, the specific gravity.
- d_{20} , the liquid density at 20 °C or 68 °F
- I, the Huang characterization parameter
- $T_{br} = T_b/T_c$, the reduced boiling point which is used to calculate the critical temperature in degrees K.
- P_c , the critical pressure in bars
- d_c , the critical density in g/cm^3
- ω , the acentric factor.
- σ , the surface tension in dynes/cm.
- δ , the solubility parameter, in (cal/cm^3)^2

For most of the crudes under study, the asphaltene molecular weight was measured. Riazi and Al-Sahhaf [116] presented a method for the calculation of different properties such as the normal boiling point, density, refractive index, critical temperature, pressure and density, acentric factor, solubility parameter and surface tension given only the molecular weight and using the following general equation

The constants a, b, and c for each property are given in Table 4.11. This method was used to determine the whole crude critical properties knowing only its molecular weight as shown in Table 4.12.

Table 4.11: Constants for the Riazi-Al-Sahhaf equation 4.26

θ	θ_∞	A	b	c
T_b	1080	6.97996	0.01964	0.67
SG	1.07	3.56073	2.93886	0.1
d_{20}	1.05	3.80258	3.12287	0.1
I	0.34	2.30884	2.96508	0.1
T_{br}	1.20	-0.34742	0.02327	0.55
$-P_c$	0	6.34492	0.72390	0.3
$-d_c$	-0.22	-3.2201	0.00090	1
$-\omega$	0.30	-6.2520	-3.64457	0.1
σ	30.3	17.45018	9.70188	0.1
δ	8.60	2.29195	0.54907	0.3

Table 4.12: Critical properties and acentric factors of the different samples of the crude oil.

Sample	T_c °C	P_c Pa x10^{-6}	ω	Mw
1	536.42	1.92	0.71	248
2	551.80	1.80	0.75	267
3	567.64	1.57	0.84	299
4	566.13	1.65	0.81	290
5	586.06	1.61	0.84	307
6	570.69	1.57	0.84	301
7	587.95	1.58	0.85	312
8	562.25	1.74	0.78	278
9	585.17	1.67	0.82	299
10	574.56	1.84	0.75	276

In case, the asphaltene molecular weight is not known, elemental analysis can be used for critical properties estimation especially for asphaltene. Therefore, we are going to use a group contribution method to calculate the critical constants which in turn are used in the estimation of other properties required later in modeling either for the bulk crude or asphaltene. Joback Group Contribution method [117] is used to find the groups' frequencies constituting the crude molecules using elemental analysis along with measured molecular weight and density. Four groups of Joback group contribution method are assumed to exist each with frequency number c1 to c4 representing how many times each group is repeated in the molecule (Table 4.13)

Choosing four groups in the Joback group contribution method was restricted by the number of equations obtained from the measured data. The four equations are solved simultaneously to get the four unknowns. The Joback group contribution estimates the critical properties. The calculation of the critical properties was checked by estimating the molar volumes of the crude oil using the PR-EOS and comparing these values with the experimental results (molecular weight divided by density). The comparison was quite favorable.

For the crude oil the following equations are used to estimate the frequency of Joback group contribution:

$$MW_c = 13c_1 + 32c_2 + 14c_3 + 17c_4 + 14c_5 \tag{4.28}$$

$$\left(H/C\right)_c = \frac{c_1 + 2c_5}{12c_1 + 12c_5} \tag{4.29}$$

$$\left(N/C\right)_c = \frac{14c_3}{12c_1 + 12c_5} \tag{4.30}$$

$$\left(S/C\right)_c = \frac{32c_2}{12c_1 + 12c_5} \tag{4.31}$$

$$n_{Ac} = 2c_1 + c_2 + c_3 + 2c_4 + 3c_5 \tag{4.32}$$

Where N,C,S and H are wt% of nitrogen, carbon, sulfur and nitrogen.

The elemental analysis data and molecular weight experimental data shown in Table 4.13 are used to calculate the group frequency numbers. With the aid of these groups formulation, the critical properties are estimated by the group contribution method of Joback.

$$T_c = T_b[0.584 + 0.965\sum\Delta_T - \sum(\Delta_T)^2]^{-1} \tag{4.33}$$

$$P_c = [0.113 + 0.0032n_A - \sum\Delta_P]^{-2} \tag{4.34}$$

$$V_c = 17.5 + \sum \Delta_V \quad (4.35)$$

$$T_b = 198 + \sum \Delta_b \quad (4.36)$$

Table 4.13: Joback Group Contribution for Critical Properties Estimation for a typical crude

Group	No. of group repetition	Properties				
		Tb	Tc	Pc	Vc	MW
=C-H ring	12.63	26.73	0.0082	0.0011	41	13
>CH2	18.34	22.88	0.0189	0	56	14
-S-	0.40	52.10	0.0019	0.0051	38	32
=N-	0.37	57.55	0.0085	0.0076	34	14
Measured Elemental Analysis			C%		83.86%	
			H%		11.19%	
			S%		1.17%	
			N%		2.908%	
Estimated Critical Properties			Tc (K)		902	
			Pc(atm)		7.6	
			w		0.68	

The same can be done for asphaltene knowing its elemental analysis. If the asphaltene structure is known, as in some cases in this study, the group contribution method will be used to estimate critical properties. For asphaltene, the proposed model structure described earlier in section 2.1 was used to set Joback groups and frequencies as shown in Table 4.14. Joback and Fedros group contribution method was used to estimate asphaltene critical temperature and volume. Asphaltene acentric factor was calculated from Riazi and Al-Sahhaf utilizing the formulated molecular weight of asphaltene. Critical pressure for asphaltene was calculated as a function of critical: temperature,

volume and compressibility factor. Table 4.15 listed the calculated critical properties for typical asphaltene.

$$T_c = 535 \log \sum \Delta_T \quad (4.37)$$

$$V_c = 17.5 + \sum \Delta_V \quad (4.38)$$

$$w = 0.6684(0.5837 \ln M - 2.5389) \quad (4.39)$$

$$zc = 0.291 - 0.08w \quad (4.40)$$

$$P_c = zcRTc / Vc \quad (4.41)$$

Table 4.14: Asphaltene Joback groups count

Group	Number
N-H ring	1
-N= ring	3
-S- ring	13
-O- ring	3
OH- phenol	3
CH3	37
CH2	74
CH	3
=CH- ring	35
=C- ring	142
CH2 ring	14
CH ring	30

Table 4.15: Typical asphaltene critical properties knowing the structure

Component	M	Tc (K)	Pc (bar)	Vc (cm^3/mol)	ω
Asphaltene	4952	1457	1.28	15069.5	1.622

4.6 Diffusion Coefficient for Asphaltenes in Bulk Crude

Diffusion of asphaltene in bulk crude will be diffusion for dilute system since asphaltene weight fraction is low in most of bulk crudes under study. The crudes that have asphaltene weight percent higher than 5 wt% will be discarded. Wilke-Method will be used here as a function of temperature:

$$D_{AB} = 7.4*10^{-4}(\varphi_B M_B)^{0.5} T/(\mu v_A^{0.6}) \quad (4.42)$$

Where

A is solute (asphaltene)

B is solvent (crude)

φ_B is 1.0 for hydrocarbons.

M_B crude molecular weight (290 g/gmol for a typical crude)

μ crude viscosity (282.2 cp as an)

v_A asphaltene molar volume (1266.7 cm^3/gmol)

The calculated diffusion coefficient will be $1.84*10^{-8}$ m^2/s at 25°C (which is comparable to the value listed in Bayat et al [77] which will be used later in asphaltene fouling model).

4.7 Thermal Conductivity

At moderate pressures, up to 50 to 60 bar, the effect of pressure on the thermal conductivity (k) of liquids is usually neglected, except near the critical point, where the liquid behaves more like a dense gas than a liquid. At lower temperatures, k increases with pressure.

Missenard has proposed a simple correlation n for k_L that extends to much higher pressures. In analytical form[118]

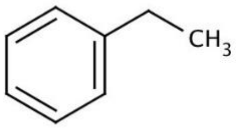

$$\frac{k_L(P_r)}{k_L(low\ pressure)} = 1 + QP_r^{0.7} \quad (4.43)$$

Where k_L(Pr) and k_L(low pressure) refer to liquid thermal conductivities at high and low (near saturation) pressure at the same temperature. Q is a parameter given in Table 4.16.

Table 4.16: Values of Q in Equation 4.43

	Reduced pressure					
T_r	1	5	10	50	100	200
0.8	0.036	0.038	0.038	(0.038)	(0.038)	(0.038)
0.7	0.018	0.025	0.027	0.031	0.032	0.032
0.6	0.015	0.020	0.022	0.024	0.025)	0.025
0.5	0.012	0.0165	0.017	0.019	0.020	0.020

Case study to estimate thermal conductivity of ethylbenzene. Same method will be used to estimate asphaltene thermal conductivity and crude oil [119].

Compound Ethylbenzene

Number of carbon atoms 8

Number of heavy atoms 8

T_b=409.3K, T=353.15K

Group	Atoms	Frequency	ΔA	ΔB	OH correction	ΔA total	ΔB total
1	1	1	16.16	-2.59	N	16.16	-2.59
4	1	1	2.33	-0.636	N	2.33	-0.636
16	4,5,6,7,8	5	6.17	-1.22	N	30.85	-6.10
17	3	1	-11	0.73	N	-11	0.73
						38.34	-8.60

$$B = \exp\left(\frac{\ln(8)}{8} \times -8.06\right) = 0.107 W.m^{-1}K^{-1}$$

$$k = \frac{A}{T_B}\left(1 - \frac{T}{T_B}\right) + B = \frac{38.34}{409.3} \times \left(1 - \frac{353.15}{409.3}\right) + 0.107 = 0.12 W.m^{-1}K^{-1}$$

At the end of this chapter all properties of asphaltene and crudes are either measured or estimated to be ready for modeling in the next chapter

Chapter 5: Results and Discussion

This chapter presents the results from the computational fluid dynamics model described in Chapter 3. The model was solved in three stages. The first stage involved solving the conservation of momentum equation on the tube side of the heat exchanger without the effect of temperature change on the fluid properties. The second stage included heat transfer from the shell side into the tube. After that, species transport was coupled with the momentum and heat transfer equations to elucidate the concentration profile of asphaltenes in the tube. The rate of fouling of asphaltenes on the inner wall of the tube was calculated by using the Ebert Panchal model [47]. The third stage was adding the element of time to the system taking into consideration the change in tube inner diameter and fluid velocity. The model was tested against the Exxon mobile fouling rate data from the original works of Ebert and Panchal [47] as well as fouling deposition thickness data from local refinery in the state of Kuwait.

5.1 Momentum balance

The process of solving the Momentum balance differential equation (equation 3.21) for the flow inside the tube requires an initial condition, two boundary conditions for the axial direction, and two boundary conditions for the radial direction. The initial condition is the inlet velocity. For the z direction the first boundary condition is also the inlet velocity at the inlet of the tube (u_z= inlet velocity at $z = 0$). The second boundary condition is fully developed flow at the end of the tube ($\frac{du_z}{dz} = 0$ at $z = \infty$). The no-slip boundary condition is applied to the tube wall.

Figure 5.1 shows the flow development along the tube side in the heat exchanger where the maximum velocity in the middle (centerline velocity) is higher than the velocity in any other

location in the tube. This finding agrees with the maximum velocity condition at the center of the tube.

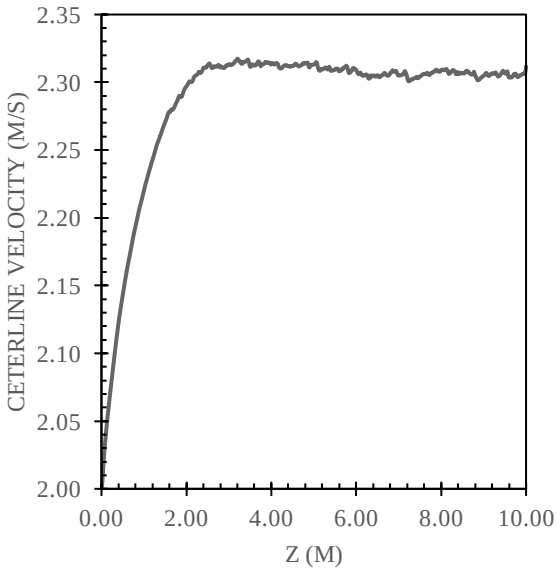

Figure 5.1: Crude oil flow development in the tube side along the (z-axis) before fouling starts (crude oil inlet velocity 2 m/s, tube radius 0.05 m, tube length 10 m)

The velocity profile in the fully developed section of the tube is shown in Figure 5.2. The previous figures explain the movement of the bulk crude oil in the tube side before the fouling starts. Figure 5.3 shows a surface plot for the turbulent kinetic energy in the tube side. The kinetic energy near the tube wall is zero due to the no-slip conditions and it increases when the flow is far away from the wall until it reaches the maximum value at the end of the turbulent boundary layer and it starts to decrease until it reaches a constant value near the tube center. This finding agrees with previous work that was found in the literature [120] (Figure 5.4).

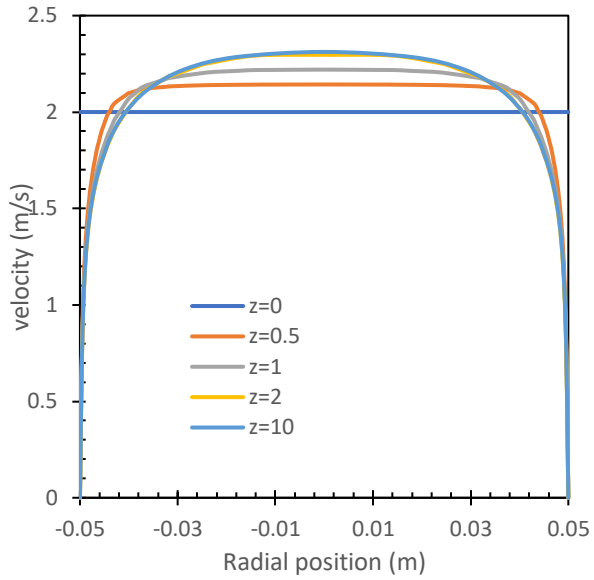

Figure 5.2: Crude oil velocity profile, after 2 m flow becomes Fully developed and all follows the same profile to the tube outlet, (inlet velocity 2 m/s, tube radius 5 cm, tube length 10 m)

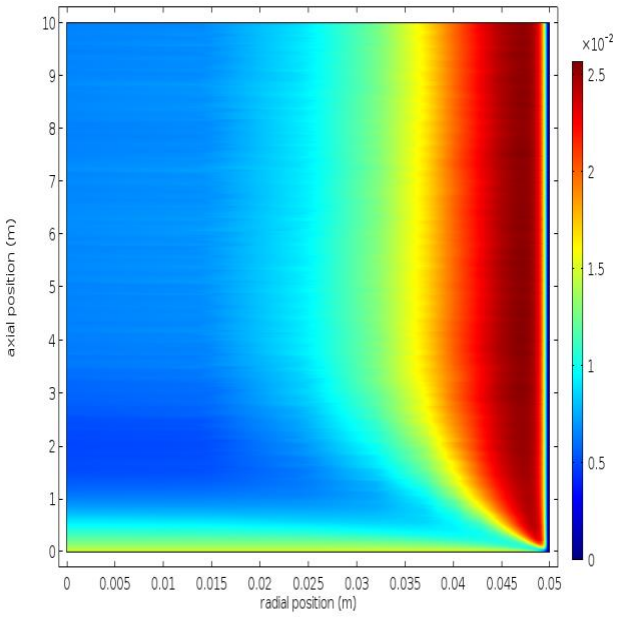

Figure 5.3: surface plot for turbulent kinetic energy in the tube side of the heat exchanger (inlet velocity 2 m/s, tube radius 5 cm, tube length 10 m)

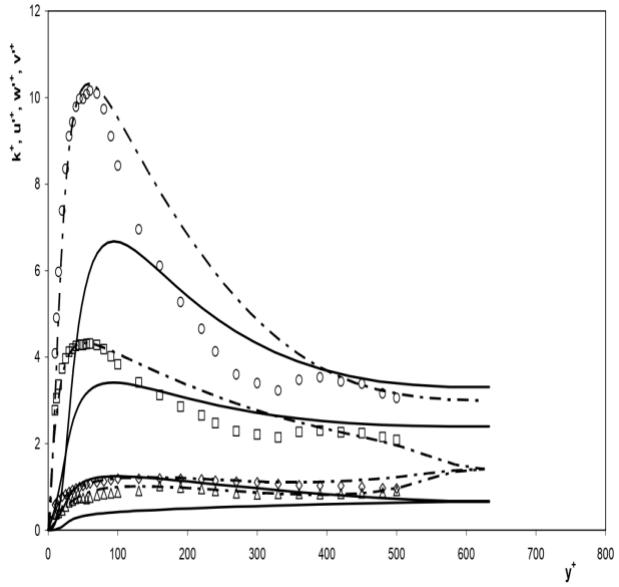

Figure 5.4: Comparison between the predicted and the measured profiles of normalized turbulent kinetic energy and Reynolds normal stresses for fully developed turbulent pipe fluid at Re=42900 in wall coordinates: ○ k, □ u, ◊ w, and Δ v [120].

5.2 Energy Balance

The energy equation (equation 3.42) requires an initial condition, two boundary conditions for the z direction, and two boundary conditions for the r direction. The initial condition is the inlet temperature. For the z direction the first boundary condition is the inlet temperature at z=0, the second boundary condition is for $z = \infty$, $\frac{\delta T}{\delta z} = 0$, At the tube wall r = R, $\frac{\delta T}{\delta z} = f(t, z)$. where f(t,z) is going to be the function of time and temperature due to change of the overall heat transfer coefficient because of the asphaltenes precipitation process. Also, at r=0, $\frac{\delta T}{\delta r} = 0$.

Introducing the temperature changes into the package will affect the physical properties of the fluid such as thermal conductivity, which is essential for equation 3.42, as well as the viscosity and density of the crude oil, which is essential for equation 3.21.

The simulation results are shown in the following Figures (5.5, 5.6, 5.7). They show that the temperature is very high at the heat transfer surface. But due to the bulk movement, high heat capacity, and low thermal conductivity of the crude, the temperature change in the crude oil is not high when compared to the calculated wall temperature. Figure 5.5 shows isothermal contours in the tube.

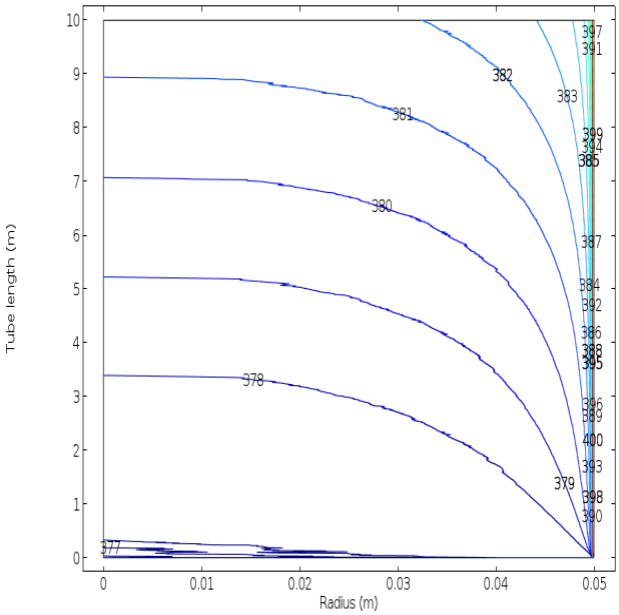

Figure 5.5: Isothermal contour (T in Celsius) (tube radius 5 cm, tube length 10 m, inlet temperature 377 °C)

Figures 5.6 and 5.7 show the temperate profile in the r direction and in the z direction, respectively. It is noticeable that in Figure 5.6 the temperature increases drastically at the tube wall this represents the metallic wall temperature. Figure 5.7 shows the average temperature in each position along the tube. Total temperature difference between inlet and outlet is 4.54 °C before fouling. It is noticeable that the temperature increase is lagging at the inlet part of the tube. This phenomenon is occurring because the crude flow is not fully developed in this section. The lag distance in Figure 5.7 is matching the fluid flow developing section in Figure 5.1.

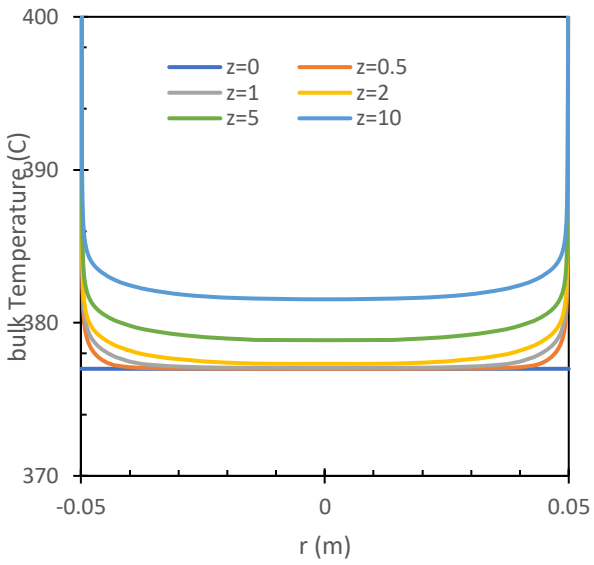

Figure 5.6: Temperature profile at different position in the z-axis (inlet: z = 0 m, midway: z = 5 m, outlet: z = 10 m) (tube radius 5 cm, tube length 10 m, inlet temperature 377 °C)

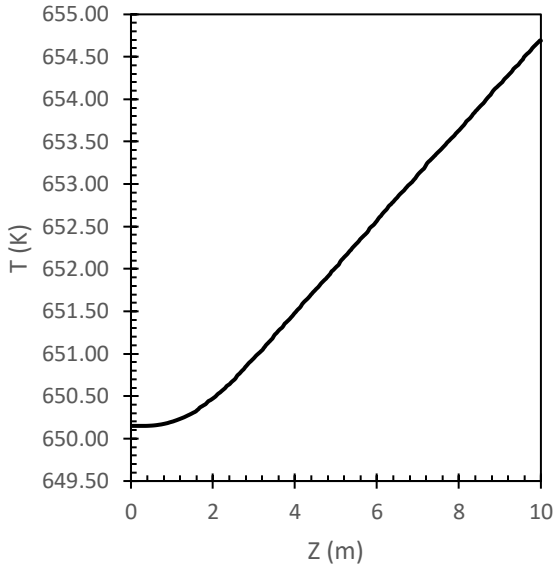

Figure 5.7: Center line temperature development in the tube side along the (z-axis) (before fouling) (tube radius 5 cm, tube length 10 m, inlet temperature 377 °C)

5.3 Ebert Panchal Equation

As found in chapter 2, fouling threshold models are the most effective for fouling prediction. Ebert and Panchal proposed the following form to fit data collected in a flow loop for crude oil fouling [47]:

$$\frac{dR_f}{dt} = \alpha Re^{\beta} \exp\left(\frac{-E}{R_g T_f}\right) - \gamma\tau \qquad (5.1)$$

where the deposition term ($\alpha Re^{\beta} \exp\left(\frac{-E}{RT_f}\right)$) is a function of film temperature, T_f and the Reynolds number, Re. The suppression term ($\gamma\tau$) depends on the wall shear stress τ. Parameters below were determined via regression to experimental data and are expected to vary between different crudes.

- A = 8.3 $K.m^2.W^{-1}$ s^{-1},
- β = -0.88,
- E_f = 68 $kJ.mol^{-1}$,
- $\gamma = 4.03x10^{-11}$ $m^4.N.K^{-1}.s^{-1}$

These parameters were used to verify the model in using the same data from the original work of Ebert and Panchal on the Exxon mobile crude. The crude used was a light crude and those parameters will need tuning for the application on heavier crudes.

The strength of Ebert and Panchal Equation is it depends on the two major fluid flow properties (viscosity and density) to predict fouling, these properties are dependent of crude composition (e.g. asphaltenes and foulants contents) and temperature. It also includes a removal terms that depends on the sheer stress at the wall of tube which is the main effective criteria for removal.

The model was developed after experimental evidence of the existence of a threshold for given operating conditions below which fouling would not occur. Since the threshold is given by the balance of the rate of deposition with the rate of suppression, its condition can be determined by setting the fouling rate to zero, equating the two terms, and solving for T_f, τ, and Re. As seen in the following sections, significance of these variables in Equation (5.1) can be applied in a relatively simple way to the design of heat exchangers by determining a fouling threshold curve and changing design parameters so that the operating conditions of the units are below the threshold value (Figure 5.8).

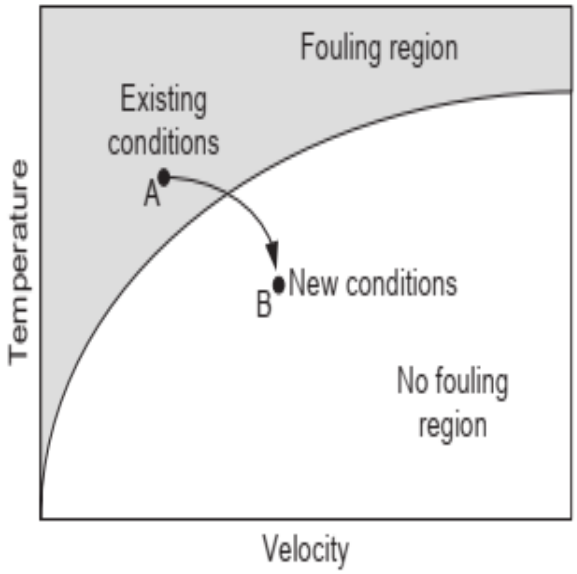

Figure 5.8: Fouling threshold concept in heat exchanger design. If operating conditions are changed from A to B, the unit moves from a fouling to a no-fouling region [121].

5.4 Mass balance results fouling deposition

Throughout series of simulations in using the combination of the COMSOL package and the Ebert and Panchal model, it was found that increasing the inlet velocity of the crude will result in less fouling as shown in Figure 5.9. It also shows that tubes with larger diameters have less fouling for

the same inlet velocities. This finding agrees with the literature reviews for different kinds of fouling models [33, 45, 56, 77, 122, 123].

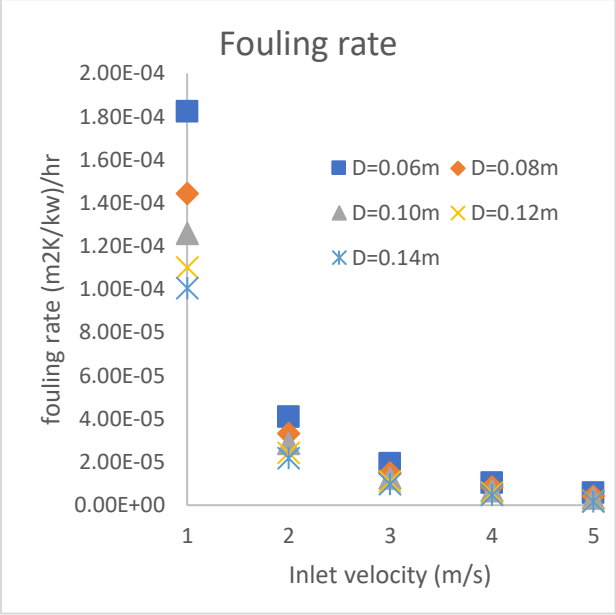

Figure 5.9: Effect of velocity change and on the fouling rate for different tube diameters.

Figure 5.10 shows that increasing the film temperature increases the fouling rate for different inlet velocities of the feed. which agrees with the findings of Ebert and Panchal work [47] as shown in Figure 5.11 and also agrees with Rodriguez and Smith work in Figure 5.8 [121]. In Figure 5.10 at higher velocity and lower temperatures the calculated removal rates are higher than the deposition rates. This will indicate an negative values of the fouling rate which means the foulants goes back to the bulk flow as an inwards flux (negative values for equation 5.1).

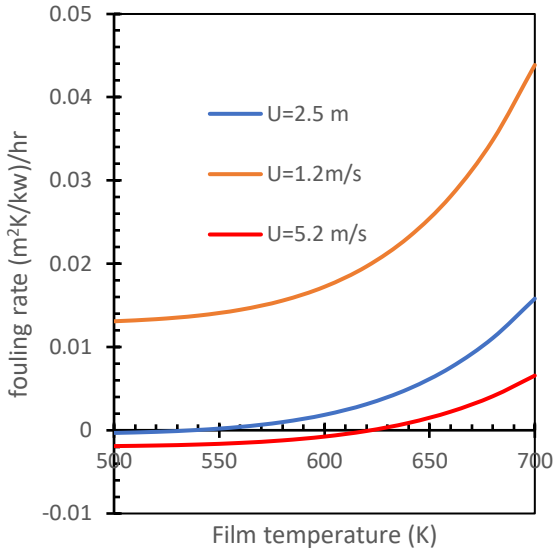

Figure 5.10: Effect of film temperature on fouling rate.

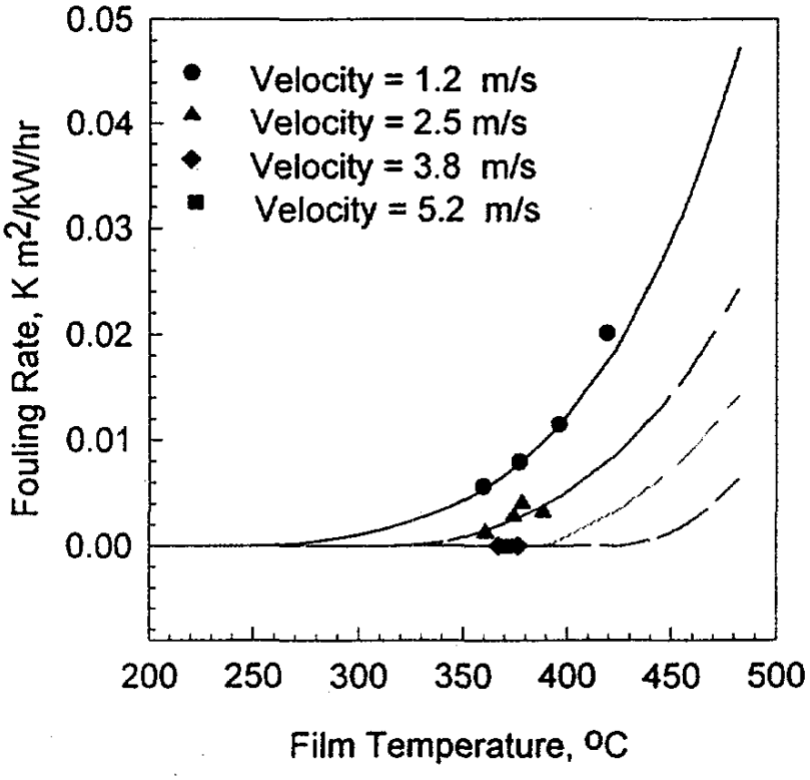

Figure 5.11: comparison of experimental and model fouling rates (Exxon Mobile data) [47]

Figure 5.12 shows the change of the fouling rate as a function of tube radius change and the inlet velocity of the tube. It is clear that the higher velocities and the bigger tube radius show a low fouling rate; a negative value of the fouling rate was calculated by the model which indicates either a no-fouling or fouling-removal cases. With larger Reynolds number the deposition term, in the Ebert and Panchal model (equation 5.1), increases. But what is happening is at the condition of higher fluid velocity and bigger diameter (maximum Reynolds number) the fouling rate is minimum; this happens due to the higher sheer stress at these conditions. This means that the removal term is becoming more significant and fouling rate is reduced. And at the low velocity and smaller diameters the deposition term is more significant than the removal term although Reynolds number is smaller. It can be concluded from this graph that in order to increase the heat transfer surface area per unit volume of the heat exchanger, it is subjecting the process to higher fouling rates. On the other hand, in order to terminate the fouling rates, the system must be redesigned with smaller heat transfer efficiency due to reduction in the heat transfer area per unit volume, or using elevated speed which requires more pumping power due to increase of pressure drop.

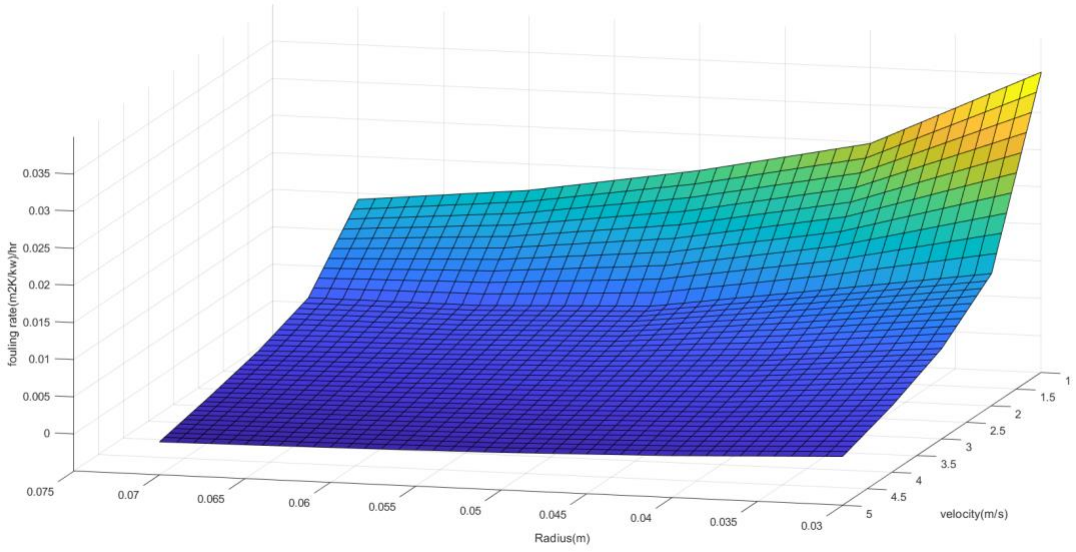

Figure 5.12: Fouling rate changes based on different diameter and velocity changes in the tube. (tube length 10 m, inlet temperature 377 °C)

5.5 Numerical Model Verification

The aim of this section is to merge Ebert and Panchal model/work with the numerical model that is used and applied to fouling data (Table 5.1) to reproduce the Fouling Rate $\frac{dR_f}{dt}$ and compare it with the test results from the original work of Ebert and Panchal on Exxon Mobile crudes [47]. The relation between fouling mass flux (N_a) outside of the boundary of the fluid and deposition of the wall was calculated as follows:

$$N_a = k_a \rho_a \frac{dR_f}{dt} \qquad (3.8)$$

where k_a and ρ_a are thermal conductivity and density of the foulant, respectively. N_a was put as a boundary condition for the mass balance equation. In this case $\frac{dR_f}{dt}$ was taken from Ebert and Panchal's Equation (equation 5.1) or it can be replaced with any other model.

In this study, there was tuning of the original Ebert and Panchal's Equation model. The parameters of the equations α, β, E, and γ were the same as the published by Ebert and Panchal [47]. The inputs of the equation were Re (Reynolds number), T_f (film temperature) and τ (shear stress), which were all taken from the material and energy balance in the Numerical Model. The input that is specified to the package are fluid properties (viscosity, density, heat capacity and thermal conductivity), inlet velocity, pressure, inlet temperature, and wall temperature. Table 5.1 shows the data and series of experimental test runs that were conducted to come up with equation 5.1. Table 5.2 shows the operating conditions of the experiment and the physical properties of the crude that were used.

Table 5.1: Summary for Exxon coking tests [47]

Test	1	2	3	4	5	6	7	8	9	10	11
t (hr)	93	132	40	402	314	402	142	191	406	392	406
T_i C (inlet temperature)	352	349	343	346	343	341	338	338	336	340	338
T_o C (outlet temperature)	366	377	399	358	358	362	382	367	353	365	352
T_w C (average wall temperature)	394	414	467	382	386	397	432	401	374	404	376
V m/s (inlet velocity)	5.2	2.5	1.2	5.2	3.7	2.5	1.2	1.2	1.3	2.5	2.5
dRf/dt (m^2K/kw)/hr	0	0.0033	0.02	0	0	0.0028	0.0115	0.0079	0.056	0.0041	0.0013

Table 5.2: Crude Oil Properties for the Cases Study Presented in Table 5.1 [47]

Pressure	41.5	bar
Temperature	354	C
Density	560	kg/m3
Heat capacity	3.35	kj/kg.k
Thermal conductivity	0.1	w/mk
viscosity	0.0024	pa.s

The Exxon Mobile data were used to test the numerical model and the results are shown in table 5.3. In the Case of zero fouling rate which are reported by the data, the model always returns a negative value for the fouling rates. This indicates that the fouling removal is higher than the fouling deposition and this explains the non-occurrence of the fouling in tests 1, 4, and 5.

Table 5.3: Model Verification Process

	Data	Model	
	dRf/dt (m2K/kw)/hr	dRf/dt (m2K/kw)/hr	error%
test 1	0	-5.03×10^{-05}	Negligible
test 2	3.30×10^{-03}	3.05×10^{-03}	7.64
test 3	2.00×10^{-02}	2.64×10^{-02}	32.06
test 4	0	-4.95×10^{-05}	Negligible
test 5	0	-2.04×10^{-05}	Negligible
test 6	2.80×10^{-03}	2.79×10^{-03}	0.50
test 7	1.15×10^{-02}	1.20×10^{-02}	4.46
test 8	7.90×10^{-03}	6.17×10^{-03}	21.93
test 9	5.60×10^{-02}	5.40×10^{-02}	3.56
test 10	4.10×10^{-03}	4.46×10^{-03}	8.78
test 11	1.30×10^{-03}	1.38×10^{-03}	6.02

The error between the fouling rate data and the calculated values is acceptable for most of the cases. Regarding tests number 3 and 8, fouling error is noticeably higher than the rest of the other cases this is due to two reasons in particular. The first reason is extreme fouling case (very high fouling rate) which makes it harder to predict the fouling process accurately. The second reason is the long test run which give a chance for the aging process. Combing the aging with the extreme fouling cases will make the process unpredictable and harder to simulate correctly.

5.6 Effects of Fouling on Heat Exchanger Performance

The combination between numerical and Ebert and Panchal equation is ready to be used in a set of predictions for changing certain conditions such as inlet velocity, flow diameter and film temperature. In this case the temperature effect on shear stress is ignored, hence Ebert and Panchal used constant viscosity and density of the crude for their data and model, which means that the shear rate (velocity gradient) is independent of temperature as well as the shear stress. Figure 5.13 shows an application of the numerical model to a test run where the tube is 10 cm in diameter and the inlet velocity of the crude oil is 2 $m.s^{-1}$. The simulation was run over a period of 350 days and

the final fouling thickness found at the end of the simulation was about 1.6 cm. This predicts that the fouling occurs continuously but the rate of fouling decreasing as shown in figure 5.14

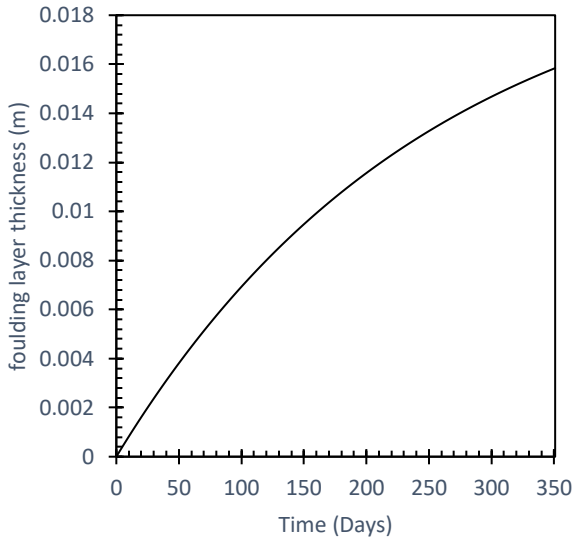

Figure 5.13: Fouling layer thickness progression with time (tube radius 5 cm, tube length 10 m, inlet velocity 2m/s inlet temperature 377 °C)

The fouling layer increases the thermal resistance on the system over time and accordingly this will affect the performance of the heat exchanger as shown in figure 5.15.

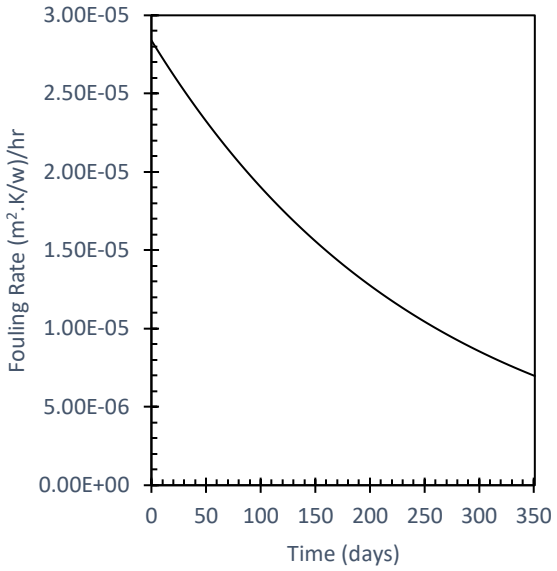

Figure 5.14: fouling rate progression with time (tube radius 5 cm, tube length 10 m, inlet velocity 2m/s inlet temperature 377 °C)

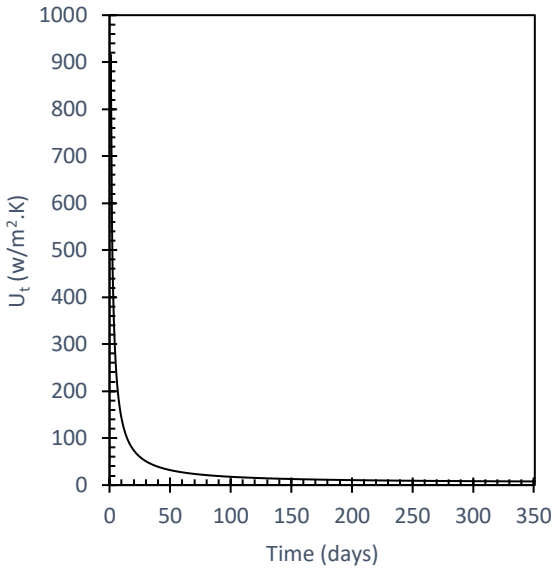

Figure 5.15: Heat exchanger performance in terms of overall heat transfer coefficient U_t over time (tube radius 5 cm, tube length 10 m, inlet velocity 2m/s inlet temperature 377 °C)

The effect of the fouling layer on the tube side average velocity, pressure drop, the velocity profile, and feed temperature change is shown in Figures 5.16, 5.17, 5.18, and 5.19, respectively. This changes account for the change in the fouling layer only, without changing the overall mass flow rate nor the shell side temperature.

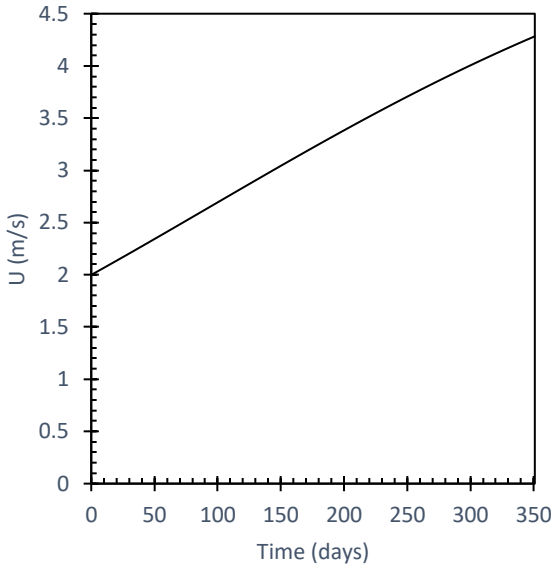

Figure 5.16: average velocity change over time (tube radius 5 cm, tube length 10 m, inlet velocity 2m/s inlet temperature 377 °C)

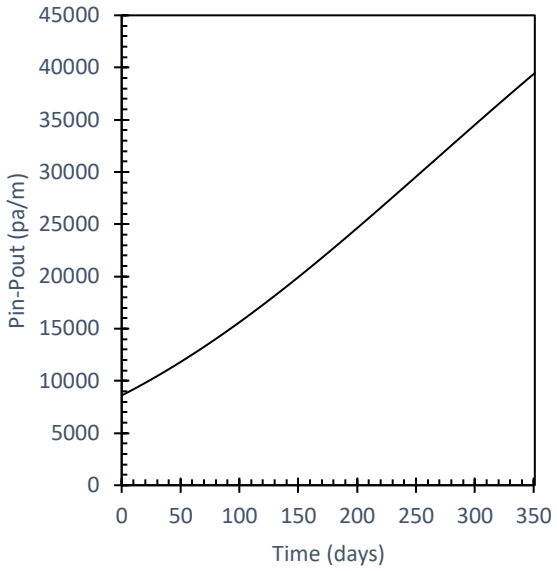

Figure 5.17: Pressure drop change over time (tube radius 5 cm, tube length 10 m, inlet velocity 2m/s inlet temperature 377 °C)

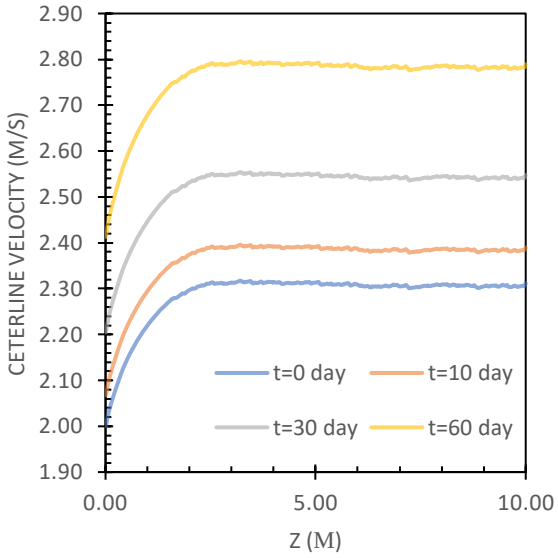

Figure 5.18: Velocity profile change over time (tube radius 5 cm, tube length 10 m, inlet velocity 2m/s inlet temperature 377 °C)

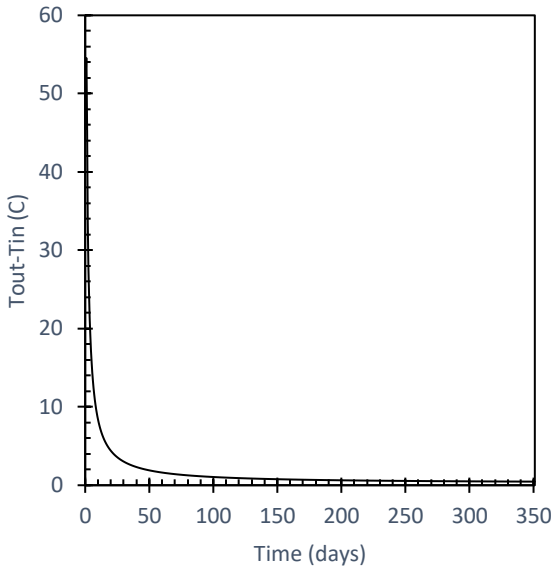

Figure 5.19: Temperature difference (T_{out}-T_{in}) change over time (tube radius 5 cm, tube length 10 m, inlet velocity 2m/s inlet temperature 377 °C)

Figure 5.20 shows the fouling deposition rate profile along the tube for different diameters and different average velocities. In all cases the model shows that the fouling rate is always greater at the tube outlet than the tube inlet.

The fouling effect on the temperature is very high, this happens very quick although the fouling rates are very small, this happens due to the very low thermal conductivity of asphaltenes and other foulants. The pressure drop increase over time, this happens due to increase in pumping power in order to maintain the targeted mass flow rate of crude while the flow cross section areas of the tubes are getting smaller due to the fouling. These findings also agrees with the findings of literature in chapter 2 [33, 45, 47, 56, 77, 122, 123].

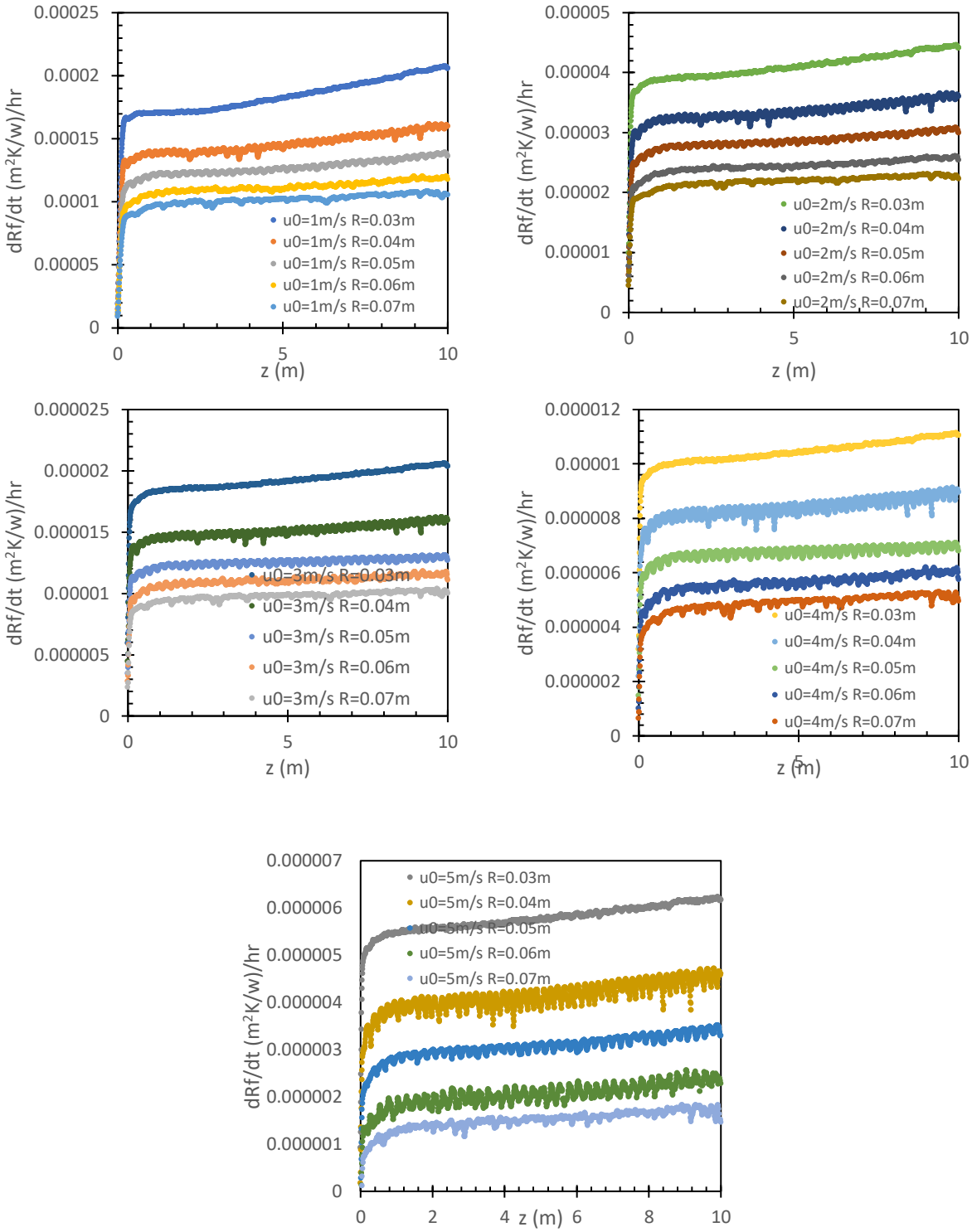

Figure 5.20: Fouling rates along the tube for different tube diameters and inlet velocities

5.7 Fouling Data from Kuwait National Petroleum Company (KNPC)

Mina Al-Ahmadi Refinery (MAA) was built in 1949 as a simple refinery with a refining capacity of exceeding 25,000 barrels per day (BPD) to supply the local market with its needs of different kinds of fuel products. The refinery is located 45 km to the South of Kuwait City on the Arabian Gulf shore. The refinery has two crude oil distillation units with capacity of current capacity of 466,000 BPD. They receive crude feed from local oil fields such as Burgan, Ratawi and other oil fields in Kuwait [124]. The Kuwaiti crudes are known for its low API values, and rich sulfur, asphaltenes and foulant contents [1, 13, 53, 125].

During the period from January 2020 to March 2020 fouling thickness data were collected from heat exchanger cleaning station inside Mina Al-Ahmadi refinery (MAA). The data is shown in two tables. Table 5.4 shows the different design, size, and operating conditions of 4 sets of tubes in different heat exchangers. Table 5.5 consists of fouling layer thickness at the tube inlet and the tube outlet of different selected tubes of each set. The data shows on pattern which is the fouling layer thickness at the tube inlet is always less than its thickness at the end of the tube. This indicates that the fouling rate is always higher at the tube's outlet than at the tube's inlet. This agrees with the finding in Figure 5.18.

The Pre-heat train (PHT) in MAA operates at constant feed and utility flow rates. And the deciding factor on the shutdown of an exchanger and cleaning it is the increase in pressure drop regardless of the heat exchanger performance.

Table 5.4: Operating conditions for selected 4 sets of tubes from MAA refinery

Set	Tube length (m)	Tube radius (m)	$T_{tube,in}$ C		$T_{shell,in}$ C		Shell size		flow rates kg/s		Cleaning intervals
			low	high	low	high	number of tubes per shell	Shell radius (m)	crude	utility	
1	7.5	0.025	300	310	450	455	618	0.8	2000	2000	5 months
2	5	0.02	250	255	350	360	740	0.7	2000	2000	2 months
3	9	0.03	250	255	290	310	650	0.95	2000	2000	1 month
4	10	0.04	30	55	180	190	400	1	4000	2000	6 months

Table 5.5: Tube side fouling layer thickness measurements at the inlet and outlet in the tube side (MAA data)

Tube	Radius (m)	length (m)	fouling thickness at the **outlet** of the tube (m)	fouling thickness at the **inlet** of the tube (m)	set
Tube 1	0.025	7.5	0.018	0.007	Set number 1
Tube 2	0.025	7.5	0.019	0.008	
Tube 3	0.025	7.5	0.018	0.007	
Tube 4	0.025	7.5	0.018	0.008	
Tube 5	0.025	7.5	0.018	0.008	
Tube 6	0.025	7.5	0.019	0.008	
Tube 7	0.025	7.5	0.020	0.007	
Tube 8	0.025	7.5	0.020	0.006	
Tube 9	0.025	7.5	0.017	0.007	
Tube 10	0.025	7.5	0.018	0.006	
Tube 11	0.02	5	0.014	0.006	Set number 2
Tube 12	0.02	5	0.014	0.006	
Tube 13	0.02	5	0.014	0.007	
Tube 14	0.02	5	0.014	0.006	
Tube 15	0.02	5	0.014	0.006	
Tube 16	0.02	5	0.014	0.007	
Tube 17	0.02	5	0.015	0.006	
Tube 18	0.02	5	0.015	0.006	
Tube 19	0.02	5	0.016	0.005	
Tube 20	0.02	5	0.014	0.005	
Tube 21	0.03	9	0.021	0.010	Set number 3
Tube 22	0.03	9	0.022	0.010	
Tube 23	0.03	9	0.022	0.012	
Tube 24	0.03	9	0.023	0.011	
Tube 25	0.03	9	0.021	0.010	
Tube 26	0.03	9	0.023	0.008	
Tube 27	0.03	9	0.019	0.009	
Tube 28	0.03	9	0.018	0.008	
Tube 29	0.03	9	0.019	0.008	
Tube 30	0.03	9	0.010	0.009	
Tube 31	0.04	10	0.025	0.012	Set number 4
Tube 32	0.04	10	0.026	0.012	
Tube 33	0.04	10	0.029	0.012	
Tube 34	0.04	10	0.030	0.012	
Tube 35	0.04	10	0.028	0.013	

The above cases were simulated using the combination between Numerical model and Elbert and Panchal equation each case separately to study. Each Case consist of different operating conditions (feed flow rate, utility flow rate, temperatures) and different heat exchanger size (tube radius and length). The target from these simulations is to calculate the fouling rates using the numerical model. Table 5.6 shows the simulated fouling rates results of each case.

Table 5. 6: Calculated fouling rate for MAA cases

Case	dRf/dt ($(m^2K/w)/hr$)
1	$3.80x10^{-05}$
2	$6.00\ x10^{-05}$
3	$1.91\ x10^{-04}$
4	$3.34\ x10^{-05}$

The calculated results show that case 2 and 3 has higher fouling rates, which explains the shorter cleaning periods of time (2 months for case 2, and 1 month of case 3). On the other hand, the calculated low fouling rates in cases 1 and 4 explains their longer cleaning periods in table 5.4.

These fouling rates cannot be assumed constant due to the continuous change in the fouling thickness which will affect the flow pattern and the temperature of the system. To solve this problem the simulation was split into times steps to cover the period between cleaning for each case and based on that the fouling thickness for each case was calculated and compared to the actual fouling thickness in table 5.7

Table 5.7: Measured and calculated fouling thickness comparison

Case	Fouling thickness (m)				Average Error
	High	Low	average	model	
1	0.019	0.007	0.013	0.013	1.38%
2	0.014	0.006	0.010	0.009	6.81%
3	0.020	0.009	0.015	0.016	9.60%
4	0.027	0.012	0.020	0.013	35.8%

The high error in case number 4 is happening because at longer periods of time gives a chance for the fouling material to age and becomes harder to remove, this is called the aging process. The aging process makes it harder to correctly predict what is happening inside the tube. And hence the higher error is shown only for case number 4.

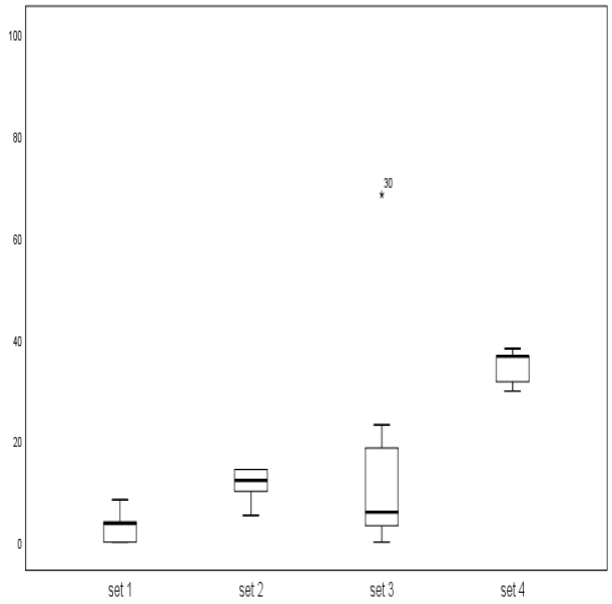

Figure 5.21: absolute error calculation for each tube fouling thickness with the model calculaled value for each set of tubes.

Figures 5.21, 5.22, 5.23, and 5.24 show the performance of the heat exchanger over time between the cleanings. They show the change of average fouling thickness, fouling rate, pressure drop increase, and heat exchanger performance over time.

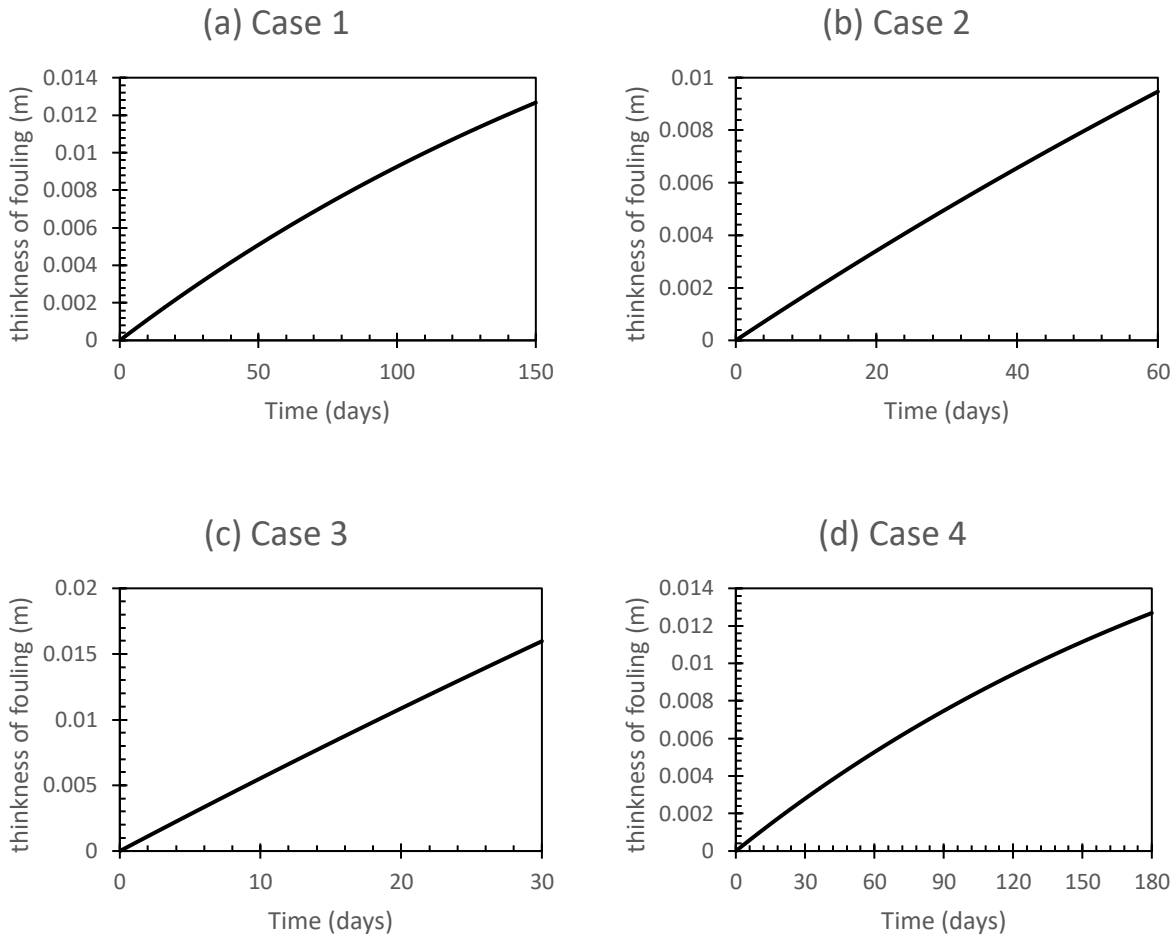

Figure 5.22: Fouling layer thickness progression over the running period of the heat exchanger between cleaning cycles. (a) Case 1: tube length 7.5 m, tube radius 2.5 cm, crude inlet temperature 300 C, cleaning period 5 months. (b) Case 2: tube length 5 m, tube radius 2 cm, crude inlet temperature 250 C, cleaning period 2 months. (c) Case 3: tube length 9 m, tube radius 3 cm, crude inlet temperature 250 C, cleaning period 1 month. (d) Case 4: tube length 10 m, tube radius 4 cm, crude inlet temperature 30 C, cleaning period 6 month

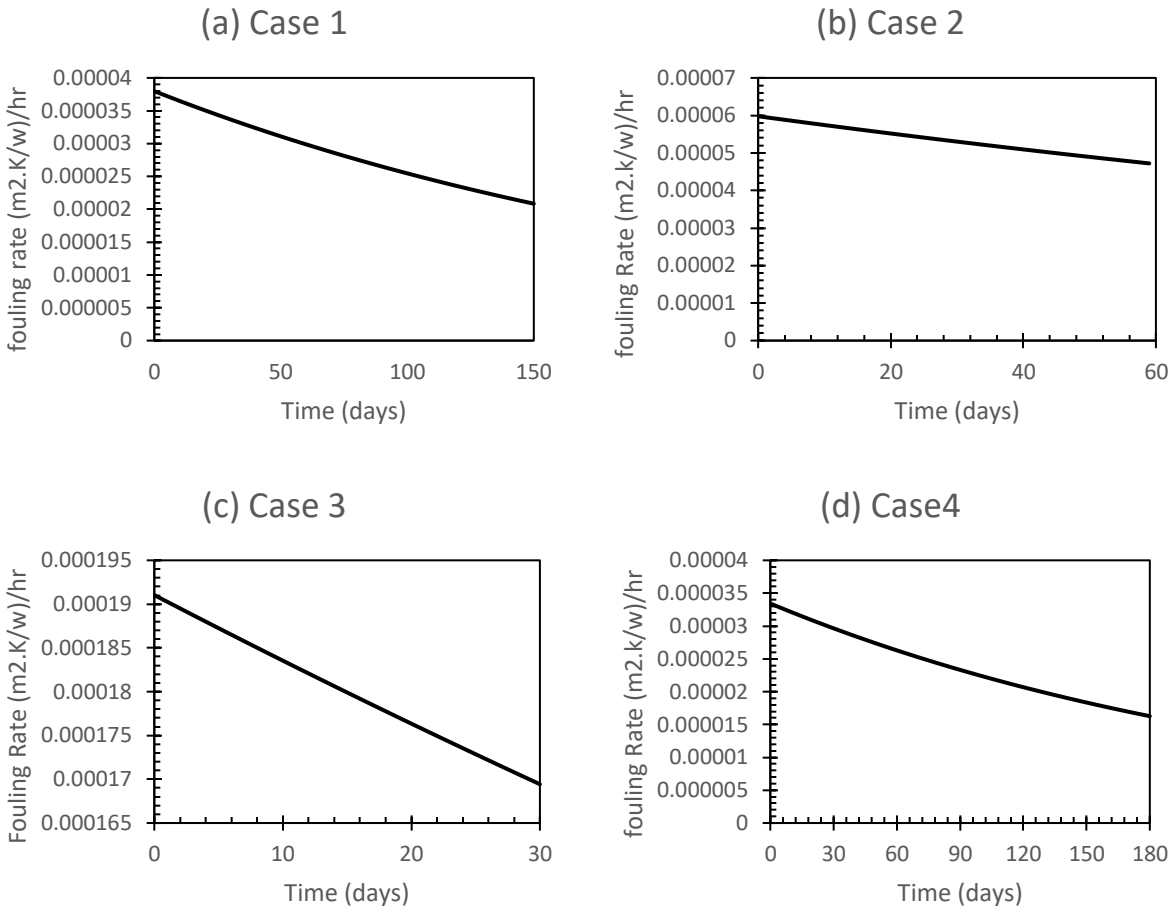

Figure 5.23: Fouling Rate decrease over time (a) Case 1: tube length 7.5 m, tube radius 2.5 cm, crude inlet temperature 300 C, cleaning period 5 months. (b) Case 2: tube length 5 m, tube radius 2 cm, crude inlet temperature 250 C, cleaning period 2 months. (c) Case 3: tube length 9 m, tube radius 3 cm, crude inlet temperature 250 C, cleaning period 1 month. (d) Case 4: tube length 10 m, tube radius 4 cm, crude inlet temperature 30 C, cleaning period 6 month

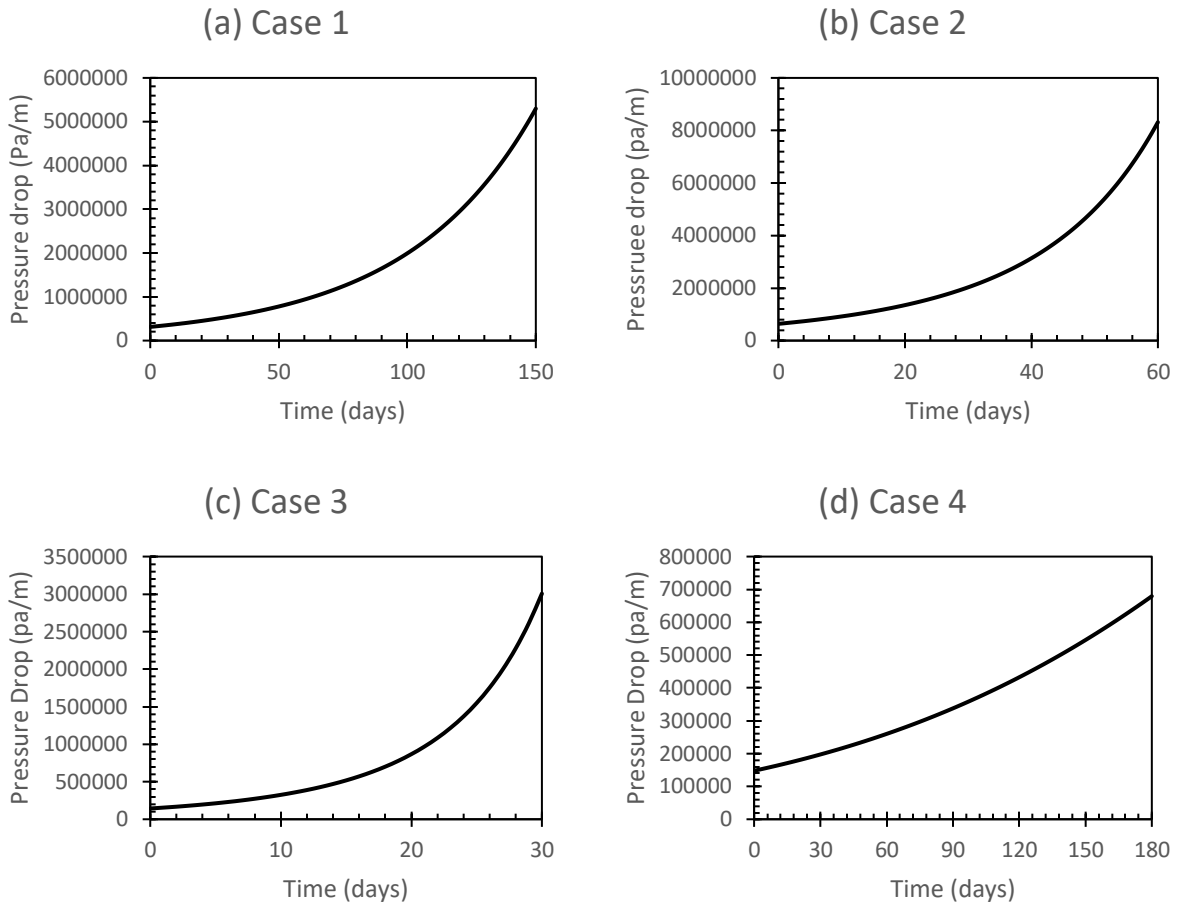

Figure 5.24: Pressure drop increase over time (a) Case 1: tube length 7.5 m, tube radius 2.5 cm, crude inlet temperature 300 C, cleaning period 5 months. (b) Case 2: tube length 5 m, tube radius 2 cm, crude inlet temperature 250 C, cleaning period 2 months. (c) Case 3: tube length 9 m, tube radius 3 cm, crude inlet temperature 250 C, cleaning period 1 month. (d) Case 4: tube length 10 m, tube radius 4 cm, crude inlet temperature 30 C, cleaning period 6 month

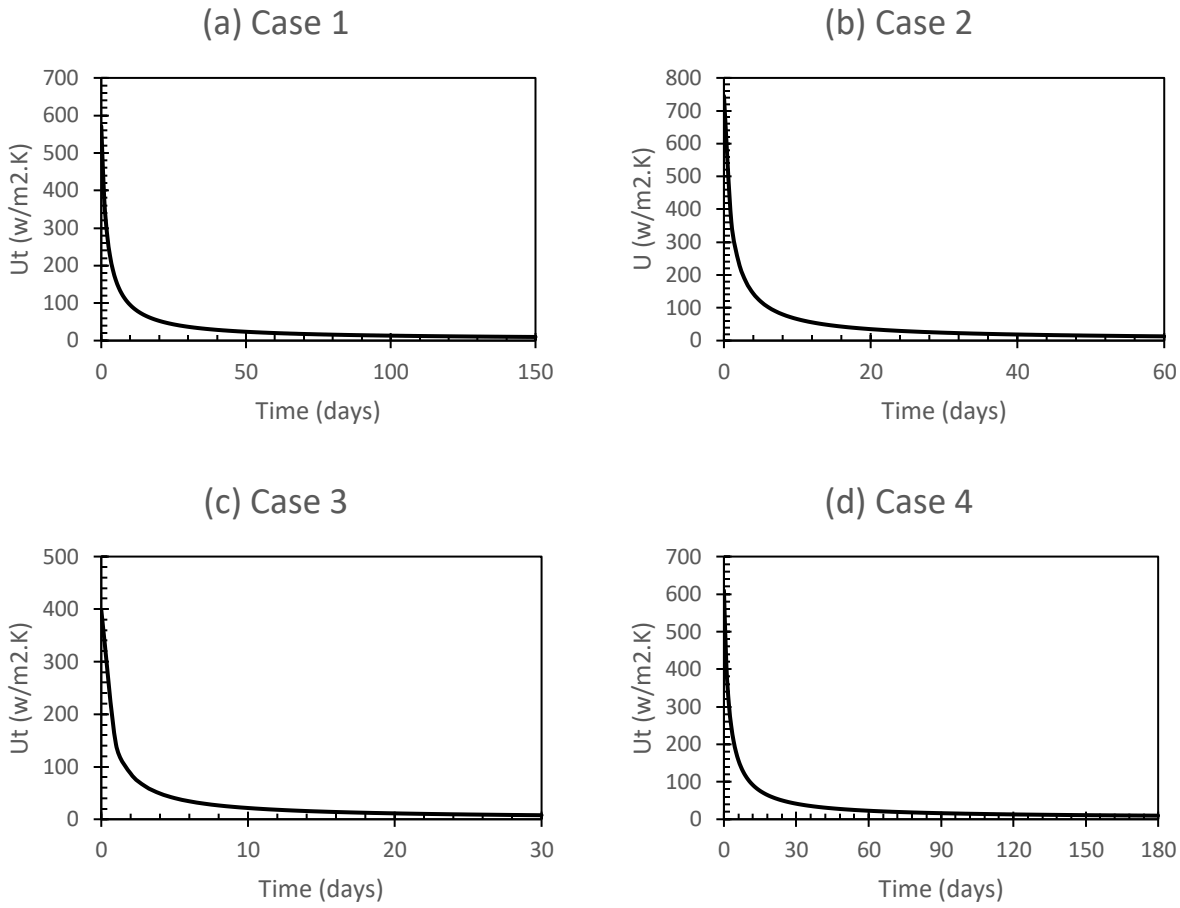

Figure 5.25: Heat exchanger performance changes over time (a) Case 1: tube length 7.5 m, tube radius 2.5 cm, crude inlet temperature 300 C, cleaning period 5 months. (b) Case 2: tube length 5 m, tube radius 2 cm, crude inlet temperature 250 C, cleaning period 2 months. (c) Case 3: tube length 9 m, tube radius 3 cm, crude inlet temperature 250 C, cleaning period 1 month. (d) Case 4: tube length 10 m, tube radius 4 cm, crude inlet temperature 30 C, cleaning period 6 month

Figure 5.24 shows that the heat exchanger performance is closing to on zero at the end of each run. This affects heat recovery periods and also requires more fuel in the furnace unit. Table 5.8 shows the pressure drop changes in the beginning and the end of each run. This explains why the operators

use this factor to decide when to stop the operation of the heat exchanger to do the cleaning process. The facts concluded from Figure 5.24 and table 5.7 explains in detail the source of the high cost of fouling in refineries. It is highly recommended to reduce the cleaning periods to one third of the current periods. This will reduce the energy cost used for pumping and heat recovery.

Table 5. 8: Comparison between pressure drops at the end and the start of each run

	ΔPf/ΔPi
Case 1	16.91
Case 2	13.02
Case 3	20.93
Case 4	4.60

The numerical model can also be used to find the fouling thickness at each point of the tube over time and at the end of each run (periods between cleaning) Figures 5.25 and 5.26 show the fouling rates and the fouling thickness at each point of the tube.

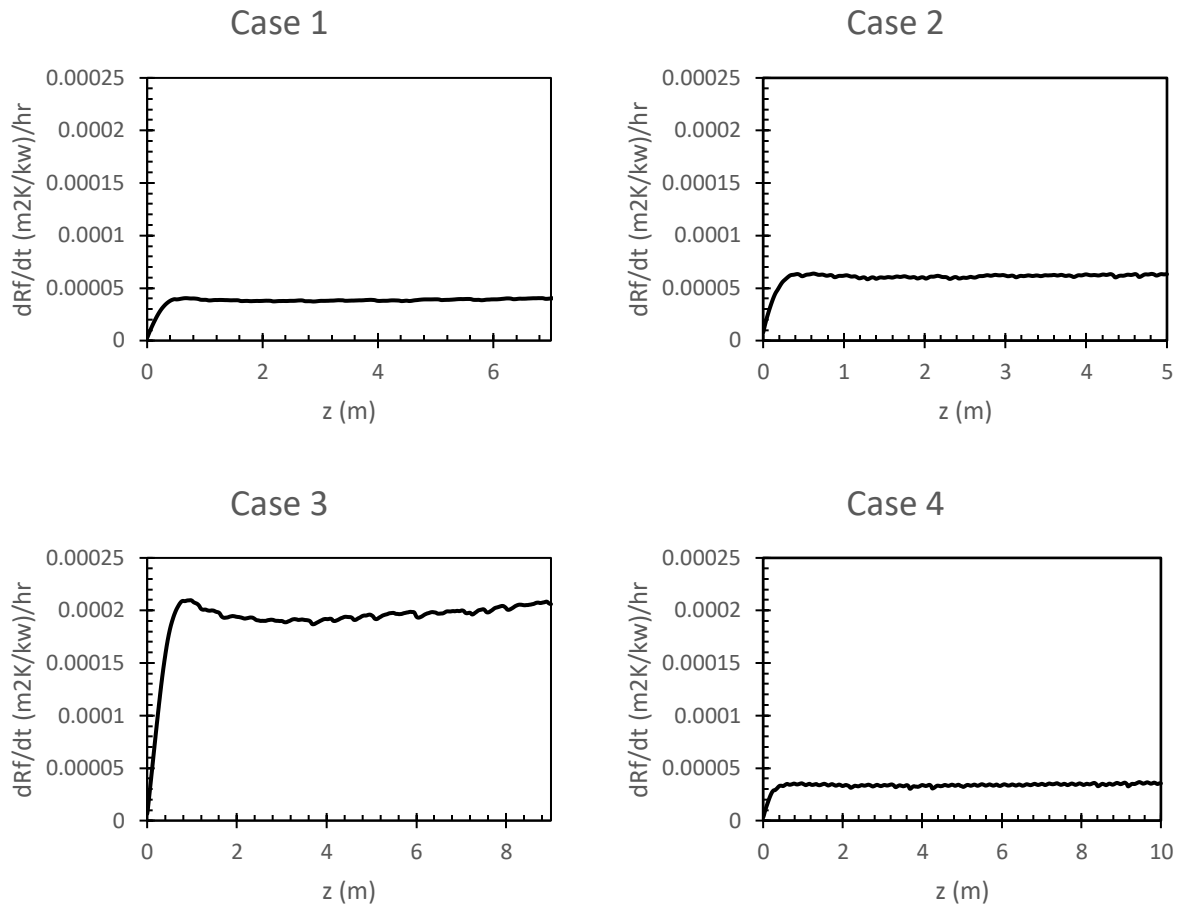

Figure 5.26: fouling rate values along the tube (Case 1: tube length 7.5 m, tube radius 2.5 cm, crude inlet temperature 300 C, cleaning period 5 months)(Case 2: tube length 5 m, tube radius 2 cm, crude inlet temperature 250 C, cleaning period 2 months)(Case 3: tube length 9 m, tube radius 3 cm, crude inlet temperature 250 C, cleaning period 1 month)(Case 4: tube length 10 m, tube radius 4 cm, crude inlet temperature 30 C, cleaning period 6 month)

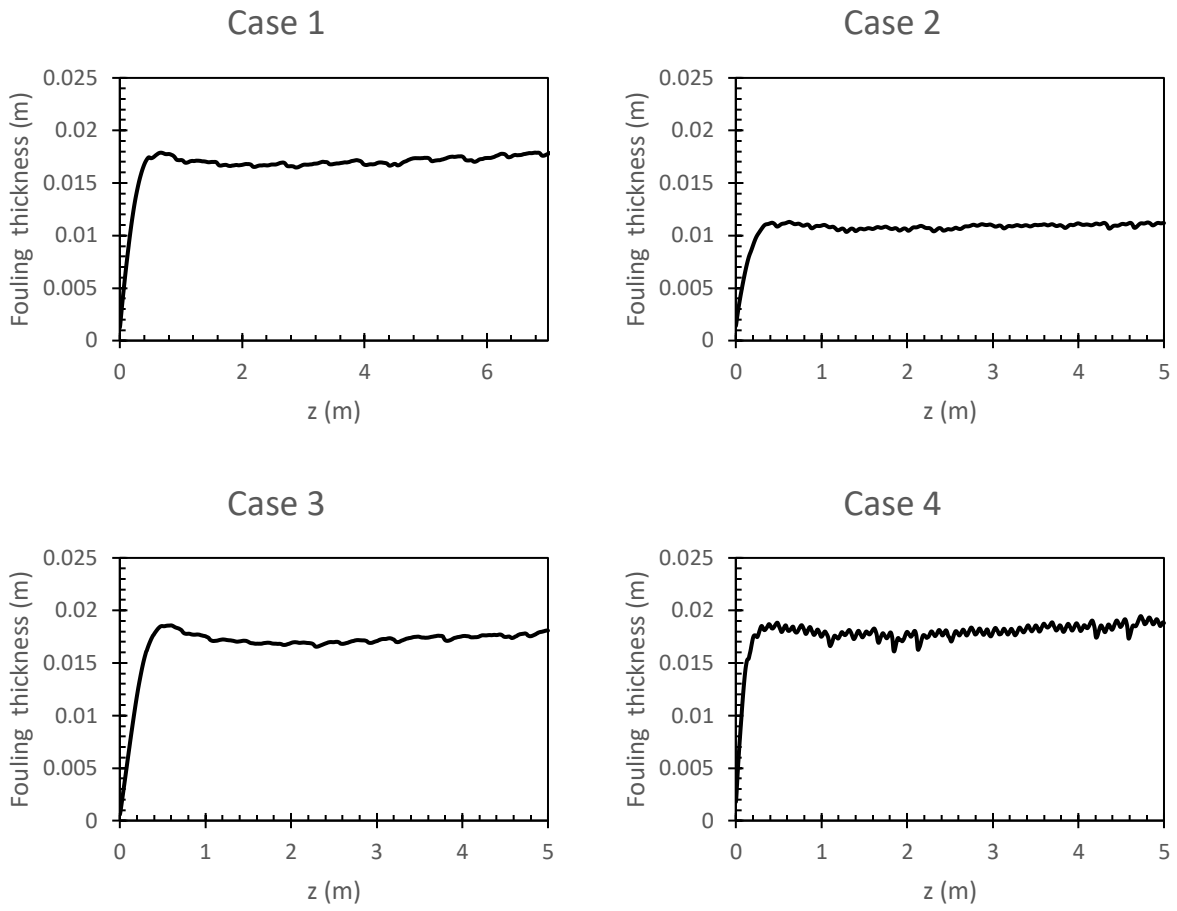

Figure 5.27: Fouling thickness at each position of the tube (Case 1: tube length 7.5 m, tube radius 2.5 cm, crude inlet temperature 300 C, cleaning period 5 months)(Case 2: tube length 5 m, tube radius 2 cm, crude inlet temperature 250 C, cleaning period 2 months)(Case 3: tube length 9 m, tube radius 3 cm, crude inlet temperature 250 C, cleaning period 1 month)(Case 4: tube length 10 m, tube radius 4 cm, crude inlet temperature 30 C, cleaning period 6 month)

These figures explain what is happening inside the tube during the fouling process. Although it cannot be measured experimentally due to the plant conditions, but model was successfully verified by other factors.

5.8 Summary

In this chapter the model was built in three stages. First stage's objective was to test momentum balance of the turbulent flow of the system without the effect of temperature on the fluid properties. The second stage's objective was to introduce the effect of temperature change on the fluid properties without the effect of the fouling on the heat transfer. The third stage introduced the species balance through the Elbert and Panchal threshold model. The objectives of this stage were to calculate the fouling rate and to test its effect on the fluid flow and the temperature change on bulk flow. The model was verified using Exxon mobile data from the original work of Elbert and Panchal and then was tested against data from local petroleum refinery in Kuwait.

Chapter 6: Conclusion and Recommendations

6.1 Conclusion

Asphaltenes are very complicated hydrocarbon compounds with deviated molecular structures with wide range of properties. Asphaltenes have a range of molecular weights from 400 to 1500. This wide range of molecular weights complicates the process of asphaltenes characterization, and its results are usually hard to predict. There was good agreement between the elution order of aromatics relative to n-alkanes on a nonpolar GC stationary phase and the boiling order during TBP distillation.

6.1.1 Previous Work Description

The phenomena/process of asphaltenes fouling can be described in a seven-points phase transition process:

1. Saturates-cloud point (SCP)
2. Saturates-pour point (SPP)
3. Asphaltene precipitation onset (APO)
4. Asphaltene and resin-flocculation (colloid formation) onset (ARFO)
5. Asphaltene and resin-deposition onset (ARDO)
6. Asphaltene-micellization onset (AMO)
7. Asphaltene-coacervation onset (ACO)

The literature has different kinds of fouling models which can be categized to 6 main groups:

1. Fouling Threshold Model
2. Solubility Models
3. Artificial Neural Network (ANN) Models

4. Equation of State Models
5. Experimentally Correlated Models
6. CFD Models

Each group has its strength and weaknesses. The existing threshold fouling models can predict that there will be an increase in initial fouling rates with an increase in bulk temperature. This is applicable for some crude oils in different conditions but also has limited application since some literature data do not agree with this finding. Solubility models are very powerful in explaining how asphaltenes behave in crude oil and how it dissolves back into it during the plant operation, which will help significantly to explain the removal stage of the fouling process. On the other hand, these models are at a major disadvantage in predicting the fouling accurately when the conditions around the bulk flow of crude oil are changing, such as when surface roughness changes during the fouling.

Artificial neural network (ANN) models are a fancy way of regression and curve fitting. Its strength is that it can take so many input factors at the same time (such as flow patterns, velocity, composition, temperature, etc.) and give a proper prediction of fouling. The major disadvantage of ANN is that it needs an enormous amount of data to train the computer package to come up with a proper regression formula. Such an amount of data is very hard to find and, as mentioned before, very expensive to obtain. Also, the regression formula is very powerful with interpolation but if the model inputs are outside the range of the training data, the extrapolation will be far from reality.

Modes based on EOS are very powerful for explaining fluid behavior from the thermodynamic point of view. However, asphaltenes do not behave as a fluid during fouling. This fact is a major

disadvantage for the EOS model. Experimental models are very powerful for explaining particular cases. Their major disadvantage is that most of the designed experiments are just an approximation of reality, and their data are not real-time plant data. The most reliable kind of experimental data are the data collected from pilot plants because real data are very difficult and expensive to obtain.

CFD modeling techinques give the ability to analyze different problems whose experiments are very difficult and expensive, which is the exact case of asphaltenes fouling. The CFD techniques offer the capacity for studying a system under conditions over its limits, which solves the problem for obtaining more and more data to do proper regression, interpolation and extrapolation. CFD uses real physics phenomena (e.g. the transport model for this research) which makes CFD very flexible and can have a high level of details that can be added or removed based on the proper assumptions. This, of course, will give more accurate description of the case under study. This flexibility of details makes the CFD approach an accurate prediction of fouling. The disadvantage of CFD is that it takes so much time for simulation, and it needs a strong machine to simulate. This time issue can be solved with the proper assumptions to simplify the mathematics behind the model. CFD is the most powerful in explaining the macro scheme of events. However, threshold models are better in explaining the micro scheme of events. The most proper approach for work is to combine the CFD approach with a threshold model. This will enable the package to simulate the bulk motion of the fluid in the tube side of the heat exchanger and the threshold model will serve as a boundary condition for the asphaltenes fouling phenomena.

6.1.2 Current Work Findings

Regularly, the problem for the heat exchanger is about heat and momentum transport. However, for the case of fouling, it is essential to consider a species balance to be able to model and acceptably simulate the problem. The primary objective of the momentum balance is to describe

the velocity and pressure profiles in the tube side and calculate shear rate and shear stress and any other factors the fouling model and the mass balance require. The importance of temperature profile is to make it handy to estimate the fluid properties such as viscosity and density, which are important for momentum equations, as well as diffusivity and in the species conservation equations and fouling models.

The mass balance is very essential hence it shows the transport of asphaltene form the bulk phase (liquid) to the foulant (solid). Mass balance enables the user to monitor the reduction in asphaltenes' concentration in the system. This reduction means that asphaltenes are precipitating on the inner walls of the pipe creating fouling and adding to the heat resistance. However, the fouling rate is very slow compared the asphaltenes mass flow in the bulk the concentration difference in the bulk system is negligible.

The best way to simulate a complicated transport problem is to use computational fluid dynamics. In order to be able to describe the fouling process CFD simulation was coupled with a the threshold fouling model of Ebert and Panchal. For this fouling problem in the tube side of heat exchanger, space dimension was selected to be 2D axisymmetric; hence all the changes in the tube are in z and r dimensions and no changes in the θ dimension. This is a problem where 3D geometry can be constructed by revolving a cross section about an axis, and no variations in any variable occur when going around the axis of revolution.

In order to start the modeling process, a huge task was conducted before model application which was crude oil and asphaltenes foulant properties estimation as function of temperature and pressure. For momentum balance, bulk viscosity and density were correlated as functions of temperature and crude API. For energy balance, bulk asphaltenes foulants thermal conductivities

was calculated. For mass/species balance, asphaltenes foulant diffusivity in the bulk was calculated. Based on the accuracy of properties' estimation the model succeeds.

Throughout the series of simulations in using the combination of the COMSOL package and the Elbert and Panchal model, it was found that increasing the inlet velocity of the crude will result in less fouling as shown in Figure 5.12. It also shows that tubes with larger diameters have less fouling for the same inlet velocities. This finding highly agrees with the literatures reviews for different kinds of fouling models [33, 45, 56, 77, 122, 123].

The model was tested using two sets of data. The first set contained fouling rates from the Exxon mobile works of Ebert and Panchal. The second set contained fouling deposition thickness and heat exchanger cleaning schedule from a local refinery in the state of Kuwait. The results showed that the combined numerical model explained the fouling satisfactory in terms of fouling thickness and fouling rates hence it was used to reproduce these data sets successfully as well as providing extra information about the temperature and velocity profile, and most importantly fouling thickness profiles along the length of tube side in the heat exchanger.

The model in this thesis work is ready to be used in a set of predictions for changing certain conditions such as inlet velocity, flow diameter and film temperature. In this case the temperature effect on shear stress is ignored, hence Ebert and Panchal's use of constant viscosity and density of the crude for their data and model, which means the shear rate (velocity gradient) is independent of temperature as well as the shear stress.

6.2 Recommendation and Future Work

More development in sampling technologies is required to collect more real fouling data from oil fields and refineries to test all models and ideas in the literature. Foulant thickness shall be

collected from different positions along the tube axis to compare with the fouling thickness profile given in this work.

Fouling samples should be collected from different positions in the tube side to undergo compositional and elemental analysis in the lab. These information will help researchers to reach a better understanding to the fouling removal process knowing what kind of bonds that may occur between the foulants and surface and the foulants themselves. This will help identifying the role of each foulant in the process of fouling.

New property models can be developed as functions of crude oil cut suede components' concentrations along with temperature and pressure would give the crude oil properties more accurately which would make the modeling/simulation processes more realistic.

The model can be used for an optimization process to estimate the physical properties that can minimize the fouling rates in the PHT. This can be combines with mixing compatibility studies to reach the optimum properties set which can be performed through different crude blends to reach the optimum point for certain operating conditions.

This blending process can also be performed with industrial solvents of refinery crude products such as diesel or gas oil. This process should be done with feasibility study for solvent recovery or product recovery.

Sensitivity studies can be done using the model in this thesis for varying operating condition to optimize the best condition which hinder fouling or increase the scheduled time for shutdown and cleaning. The model can also estimate and suggest the best time of shutdown and cleaning.

Future researches can explore the coupling of more threshold models with CFD. This can reliably give a clearer picture of which model can be applied successfully on an industrial scale. Another

future research idea is to couple CFD with other kinds of models such as Solubility Models or Equation of State Models.

The model can be extended to be applied on shell side of the heat exchanger. This will require a major change the geometry and the boundary conditions. Another expansion would be to apply the fouling models in other units in the refinery such as reactors, separation towers, absorbers, and flash drums. Studying the effect of fouling on the performance of each of these units will cause a drastic reduction on the energy required for operation and will enhance their performance.

Chapter 7: References

1. Fahim MA, Al-Sahhaf TA, Elkilani A: **Fundamentals of Petroleum Refining**, 1st edn: Elsevier 2009.

2. Speight JG: **Fouling in refineries**: Elsevier; 2015.

3. Panchal CB: **Fouling mitigation in the petroleum industry: where do we go from here?** In: *engineering foundation conference on fouling mitigation in industrial heat exchangers; San Luis Obispo, California*. 1995.

4. Heat-Exchanger: **A Global Strategic Business Report Global Industry Analysts**: Inc., San Jose, CA; 2008.

5. Garrett-Price BA, Smith SA, Watts RL, Knudsen JG, Marner WJ, Suitor JW: **Fouling of Heat Exchangers: Characteristics, Costs, Prevention, Control and Removal**. New Jersey: Noyes Publications; 1985.

6. Bott TR: **Fouling Notebook**. Rugby: Institution of Chemical Engineers; 1990.

7. Steinhagen R, Müller-Steinhagen H, Maani K: **Problems and costs due to heat exchanger fouling in New Zealand industries**. *Heat Transfer Engineering* 1992, **14**:19-30.

8. Müller-Steinhagen H, Malayeri MR, Watkinson AP: **Heat exchanger fouling: environmental Impacts**. *Heat Transfer Engineering* 2009, **30**:773-776.

9. David C. Podgorski, Yuri E. Corilo, Leonard Nyadong, Vladislav V. Lobodin, Benjamin J. Bythell, Winston K. Robbins, Amy M. McKenna, Alan G. Marshall, Rodgers RP: **Heavy Petroleum Composition. 5. Compositional and Structural Continuum of Petroleum Revealed**. *Energy Fuels* 2013, **27**(3):1268–1276.

10. Evdokimov IN: **Bifurcated correlations of the properties of crude oils with their asphaltene content**. *Fuel* 2005, **84**:13 -28.

11. Roenningsen HP, Skjevrak P: **Characterization of North Sea petroleum fractions: aromatic ring class distribution**. *Energy & Fuels* 1990, **4**(5):608–626.

12. Silva SL, Silva AMS, Ribeiro JC, Martins FG, Da-Silva FA, Silva CM: **Chromatographic and spectroscopic analysis of heavy crude oil mixtures with emphasis in nuclear magnetic resonance spectroscopy: A review**. *Analytica Chimica Acta* 2011, **707**(1 - 2):18 - 37.

13. Al-Sahhaf TA, Fahim MA, Elkilani AS: **Retardation of asphaltene precipitation by addition of toluene, resins, deasphalted oil and surfactants**. *Fluid Phase Equilibria* 2002, **194–197**:1045–1057.

14. Victorov AI, Firoozabadi A: **Thermodynamic micellizatin model of asphaltene precipitation from petroleum fluids**. *AIChE Journal* 1996, **42**:1753.

15. V DZ, A MM, M ZN: **Oils of the USSR. Reference book,**, vol. 1–4. Moscow: Khimija; 1971.

16. Shirdel M, Paes D, Ribeiro P, Sepehrnoori K: **Evaluation and comparison of different models for asphaltene particle deposition in flow streams**. *Journal of Petroleum Science and Engineering* 2012, **84-58**:57-71.

17. Mousavi-Dehghani SA, Riazi MR, Vafaie-Sefti M, Mansoori GA: **An analysis of methods for determination of onsets of asphaltene phase separations**. *Journal of Petroleum Science and Engineering* 2004, **42**:145-156.

18. Fuhr BJ, Klein LL, Reichert C: **Measurement Of Asphaltene Flocculation In Bitumen Solutions**. *Journal of Canadian Petroleum Technology* 1986, **25**(5):33-37.

19. Fotland P, Anfidsen H, Fadnes FH: **Detection of asphaltene precipitation and amounts precipitated by measurement of electrical conductivity**. *Fluid Phase Equilibria* 1993, **82**.

20. Fuhr BJ, Cathrea L, Coates H, Kalra H, Majeed AI: **Properties of asphaltenes from a waxy crude**. *Fuel* 1991, **70**.

21. Burke NE, Hobbs RE, Kashou SF: **Measurement and modeling of asphaltene precipitation**. *Journal of Petroleum Technology* 1990, **42**(11):1440– 1447.

22. Buckley JS: **Microscopic investigation of the onset of asphaltene precipitation**. *Fuel Science and Technology International* 1996, **14**(1-2):55-74.

23. Beal SK: **Deposition of Particles in Turbulent Flow on Channel or Pipe Walls**. *Nuclear Science and Engineering* 1970, **40**(1):1-11.

24. Escobedo J, Mansoori GA: **Asphaltene and other heavy-organic particle deposition during transfer and production operation**. In: *Production Operation Symposium; Oklahoma City, Oklahoma, U.S.A.* SPE 1995.

25. J.W.Cleaver, B.Yates: **A sub layer model for the deposition of particles from a turbulent flow**. In: *Chemical Engineering Science.* vol. 30; 1975: 983-992.

26. Herz A, Malayeri MR, Müller-Steinhagen H: **Fouling of roughened stainless steel surfaces during convective heat transfer to aqueous solutions**. *Energy Conversion and Management* 2008, **49**(3381–6).

27. Mozdianfard MR, Behranvand E: **A field study of fouling in CDU preheaters at Esfahan refinery**. *Applied Thermal Engineering* 2013, **50**:908 - 917.

28. Belmar-Beiny MT, Gotham SM, Peterson WR, Fryer PJ, Pritchard AM: **The effect of Reynolds number and fluid temperature in whey protein fouling**. *Journal of Food Engineering* 1993, **19**:119 - 139.

29. Belmar-Beiny MT, Fryer PJ: **Preliminary stages of fouling from whey protein solutions**. *Journal of Dairy Research* 1993, **60**(467 - 483).

30. Geddert T, Bialuch I, Augustin W, Scholl S: **Extending the induction period of crystallization fouling through surface coating**. *Heat Transfer Engineering* 2009, **30**(10 - 11):868 - 875.

31. Augustin W, Geddert T, Scholl S: **Surface treatment for the mitigation of whey protein fouling**. In: *the 7th International conference of Heat Exchanger Fouling and Cleaning: 2000; New York,*. Engineering Conferences International.

32. Vahdat AA, Ghaebi H, Amidpour M: **Novel graphical approach as fouling pinch for increasing fouling formation period in heat exchanger network (HEN) state of the art**. *Energy Conversion and Management* 2011, **52**:117–124.

33. Nasr MRJ, Givi MM: **Modeling of crude oil fouling in preheat exchangers of refinery distillation units**. *Applied Thermal Engineering* 2006, **26**:1572–1577.

34. Filho LOdO, Liporace FS, Queiroz EM, Costa ALH: **Investigation of an alternative operating procedure for fouling management in refinery crude preheat trains**. *Applied Thermal Engineering* 2009, **29**:3073–3080.

35. Filho LOO: **A Matricial Approach for Modeling and Simulation of Heat Exchanger Networks with Application for Fouling Management**. Rio de Janeiro State University; 2007.

36. Ishiyama EM, Paterson WR, Wilson DI: **Thermo-hydraulic channelling in parallel heat exchangers subject to fouling**. *Chemical Engineering Science* 2008, **63**(13):3400–3410.

37. Panuganti SR, Vargas FM, Gonzalez DL, Kurup AS, Chapman WG: **PC-SAFT characterization of crude oils and modeling of asphaltene phase behavior**. *Fuel* 2012, **93**:658–669.

38. Jamialahmadi M, Soltani B, Müller-Steinhagen H, Rashtchian D: **Measurement and prediction of the rate of deposition of flocculated asphaltene particles from oil**. *International Journal of Heat and Mass Transfer* 2009, **52**:4624–4634.

39. Tuladhar TR, Paterson WR, Wilson DI: **Dynamic gaugingin duct flows**. *Canadian Journal of Chemical Engineering* 2003, **81**:279–284.

40. Markowski M, Trafczynski M, Urbaniec K: **Validation of the method for determination of the thermal resistance of fouling in shell and tube heat exchangers**. *Energy Conversion and Management* 2013, **76**:307–313.

41. Knudsen JG, Dahcheng L, Ebert WA: **The determination of the threshold fouling curve for a crude oil, in: T.R. Bott, et al. (Eds.),** . In: *Understanding Heat Exchanger Fouling and its Mitigation; Begell House, New York*. 1999: 265–272.

42. Polley GT, Wilson DI, Yeap BL, Pugh SJ: **Use of crude oil fouling threshold data in heat exchanger design**. *Applied Thermal Engineering* 2002, **22**:763–776.

43. POLLEY GT, WILSON DI, YEAP BL, PUGH SJ: **Evaluation of laboratory crude oil threshold fouling data nfor application to refinery pre-heat trains**. *Applied Thermal Engineering* 2002, **22**:777–788.

44. Panchal CB, Kuru WC, Liao CF, Ebert WA, Palen JW: **Threshold conditions for crude oil fouling, in: T.R. Bott, L.F. Melo, C.B. Panchal, E.F.C. Somerscales (Eds.)**. In: *Understanding Heat Exchanger Fouling and Mitigation; Begell House, New York*. 1999: 273-279.

45. YEAP BL, WILSON DI, POLLEY GT, PUGH SJ: **Mitigation of Crude Oil Refinery Heat Exchanger Fouling Through Retrofits Based on Thermo-Hydraulic Fouling Models**. *Chemical Engineering Research and Design* 2004, **82**(A1):53–71.

46. EPSTEIN N: **Thinking about Heat Transfer Fouling: A 5 × 5 Matrix**. *Heat Transfer Engineering* 1983, **4**(1):43-56.

47. Ebert WA, Panchal CB: **Analysis of Exxon crude-oil slip stream coking data**. In: *Fouling Mitigation of Industrial Heat Exchange Equipment; Begell House, New York, USA*. Panchal, C.B. Bott, T.R. Somerscales, E.F.C. Toyama, S. 1997: 43–56.

48. Panchal CB, Huang-Fu EP: **Effects of mitigating fouling on the energy efficiency of crude-oil distillation**. *Heat Transfer Engineering* 2000, **21**:3-9.

49. Hirschberg A, deJong L, Schipper B, Meijer J: **Influence of Temperature and Pressure on Asphaltene Flocculation**. *Society of Petroleum Engineers* 1984, **24**(3).

50. Leontaritis K, Mansoori G: **Asphaltene Flocculation During Oil Recovery and Processing: A Thermodynamic Colloidal Model**. In: *SPE International Sypmposium on Oil Field Chemistry; San Antonio TX*. Society of Petroleum Engineers 1987: 16258.

51. Flory PJ: **Thermodynamics of High Polymer Solutions**. *The Journal of Chemical Physics* 1941, **9**.

52. Huggins ML: **Solutions of Long Chain Compounds**. *the Journal of Chemical Physics* 1941, **9**:440.

53. Fahim MA, Al-Sahhaf TA, Elkilani AS: **Prediction of Asphaltene Precipitation for Kuwaiti Crude Using Thermodynamic Micellization Model**. *Industrial & Engineering Chemistry Research* 2001, **40**:2748-2756.

54. Victorov AI, Smirnova NA: **Thermodynamic Model of Petroleum Fluids Containing Polydisperse Asphaltene Aggregates**. *Industrial & Engineering Chemistry Research* 1998, **37**(8):3242-3251.

55. Kashani MN, Aminian J, Shahhosseini S, Farrokhi M: **Dynamic crude oil fouling prediction in industrial preheaters using optimized ANN based moving window technique**. *Chemical Engineering Research and Design* 2012, **90**:938–949.

56. Aminian J, Shahhosseini S: **Evaluation of ANN modeling for prediction of crude oil fouling behavior**. *Applied Thermal Engineering* 2008, **28**:668-674.

57. Mena-Cervantes VY, Hernández-Altamirano R, Buenrostro-González E, Beltrán HI, Zamudio-Rivera LS: **Development of oxazolidines derived from polyisobutylene succinimides as multifunctional stabilizers of asphaltenes in oil industry**. *Fuel* 2013, **111**:293-301.

58. Zahedi G, Fazlali AR, Hosseini SM, Pazuki GR, a LS: **Prediction of asphaltene precipitation in crude oil**. *Journal of Petroleum Science and Engineering* 2009, **68**:218-222.

59. Shirani B, Nikazar M, Mousavi-Dehghani SA: **Prediction of asphaltene phase behavior in live oil with CPA equation of state**. *Fuel* 2012, **97**:89-96.

60. Shirani B, Nikazar M, Naseri A, Mousavi-Dehghani SA: **Modeling of asphaltene precipitation utilizing Association Equation of State**. *Fuel* 2012, **93**:59-66.

61. Alcazar-Vara LA, Buenrostro-Gonzalez E: **Characterization of the wax precipitation in Mexican crude oils**. *Fuel Processing Technology* 2011, **92**:2366–2374.

62. ASTM: **Standard Test Method for Pour Point of Petroleum Products**. In., vol. ASTM D97 - 17b.

63. Yang M, Young A, Niyetkaliyev A, Crittenden B: **Modelling fouling induction periods**. *International Journal of Thermal Sciences* 2012, **51**:175-183.

64. Trejoa F, Centenoa G, Ancheyta J: **Precipitation, fractionation and characterization of asphaltenes from heavy and light crude oils**. *Fuel* 2004, **83**:2169–2175.

65. International A: **Standard Test Method for n-Heptane Insolubles**. In. West Conshohocken: PA; 2012.

66. Okhotnikova ES, Ganeeva YM, Yusupova TN, Morozov VI, Frolov IN, Romano GV: **High-molecular-mass asphaltene fraction and its effect on the structure and stability of oxidized bitumens**. *Petroleum Chemistry* 2011, **51**(3):187–191.

67. Kaminski TJ, Fogler HS, Wolf N, Wattana P, Mairal A: **Classification of Asphaltenes via Fractionation and the Effect of Heteroatom Content on Dissolution Kinetics**. *Energy Fuels* 2000, **14**(1):25-30.

68. Biyanto TR, Ramasamy M, Jameran AB, Fibrianto HY: **Thermal and hydraulic impacts consideration in refinery crude preheat train cleaning scheduling using**

recent stochastic optimization methods. *Applied Thermal Engineering* 2016, **108**:1436–1450.

69. Mozdianfard MR, Behranvand E: **Fouling at post desalter and preflash drum heat exchangers of CDU preheat train**. *Applied Thermal Engineering* 2015, **89**:783-794.

70. Lambourn GA, Durrieu M: **Fouling in Crude Oil Preheat Trains**. In: *Advanced Course in Heat Exchangers: Theory and Practice ICHMT Symposium; Dubrovnik, Croatia*. 1983: 841-852.

71. Gonçalves CdO, Queiroz EM, Pessoa FLP, Liporace FS, Oliveira SG, Costa ALH: **Heuristic optimization of the cleaning schedule of crude preheat trains**. *Applied Thermal Engineering* 2015, **73**:3-14.

72. Liporace FdS, Oliveira SGd: **REAL TIME FOULING DIAGNOSIS AND HEAT EXCHANGER PERFORMANCE**. *Heat Transfer Engineering* 2007, **28**(3):193-201.

73. Costa ALH, Tavares VBG, Borges JL, Queiroz EM, Pessoa FLP, Liporace FdS, Oliveira SGd: **Parameter Estimation of Fouling Models in Crude Preheat Trains**. *Heat Transfer Engineering* 2013, **34**(8-9):683-691.

74. Behbahani TJ, Ghotbi C, Taghikhani V, Shahrabadi A: **A modified scaling equation based on properties of bottom hole live oil for asphaltene precipitation estimation under pressure depletion and gas injection conditions**. *Fluid Phase Equilibria* 2013, **358**:212– 219.

75. McNeil DA, Burnside BM, Miller KM, Tarrad AH: **A comparison between HIGHFLUX and plain tubes, boiling pentane in a horizontal kettle reboiler**. *Applied Thermal Engineering* 2002, **22**:803–814.

76. Yang M, Young A, Niyetkaliyev A, Crittenden B: **Modelling fouling induction periods**. *International Journal of Thermal Sciences* 2012, **51**:175 - 183.

77. Bayat M, Aminian J, Bazmi M, Shahhosseini S, Sharifi K: **CFD modeling of fouling in crude oil pre-heaters**. *Energy Conversion and Management* 2012, **64**:344–350.

78. Wang Y, Zhan S, Feng X: **Optimization of velocity for energy saving and mitigating fouling in a crude oil preheat train with fixed network structure**. *Energy* 2015, **93**:1478-1488.

79. Yang M, Crittenden B: **Fouling Thresholds in Bare Tubes and Tubes Fitted with Inserts**. *Applied Energy* 2012, **89**:67-73.

80. Crittenden BD, Kolaczkowski ST, Takemoto T, Phillips DZ: **Crude oil fouling in a pilot-scale parallel tube apparatus**. *Heat Transfer Engineering* 2009, **30**:777-785.

81. Krueger AW, Pouponnot F: **Heat exchanger performance enhancement through the use of tube inserts in refineries and chemical plants – successful application examples: Spirelf, Turbotal and Fixotal systems**. In: *Eurotherm Conference on Fouling and Cleaning in Heat Exchangers; Schladming, Austria*. 2009: 400-406.

82. Gu T, Y.M.J.Chew, W.R.Paterson, D.I.Wilson: **Experimental andCFDstudiesoffluiddynamicgaugininductflows**. *Chemical EngineeringScience* 2009, **64**:219--227.

83. Yang M, Wood Z, Rickard B, Crittenden B, Gough M, Droegemueller P, Higley T: **Mitigation of crude oil fouling by turbulence enhancement in a batch stirred cell**. *Applied Thermal Engineering* 2013, **54**:516-520.

84. Butterworth D: **Design of shell-and-tube heat exchangers when the fouling depends on local temperature and velocity**. *Applied Thermal Engineering* 2002, **22**:789–801.

85. Hosseini-Dastgerdi Z, Tabatabaei-Nejad SAR, Khodapanah E, Sahraei E: **A comprehensive study on mechanism of formation and techniques to diagnose asphaltene structure; molecular and aggregates: a review**. *ASIA-PACIFIC JOURNAL OF CHEMICAL ENGINEERING* 2015, **10**:1-14.

86. Bird RB, Stewart WE, Lightfoot EN: **Transport Phenomena**: John Wiley & Sons; 2001.

87. Glasgow LA: **Transport Phenomena: An Introduction to Advanced Topics**, 1st edn: Wiley; 2010.

88. Leal LG: **Advanced Transport Phenomena: Fluid Mechanics and Convective Transport Processes**: Cambridge University Press; 2012.

89. Slattery JC: **Advanced Transport Phenomena**: Cambridge University Press; 1999.

90. Menter F, Esch T, Kubacki S: **Transition modeling based on local variables**. In: *5th International symposium of engineering turbulence modeling and measurements; Mallora, Spain;*. 2002.

91. Menter F: **Zonal Two Equation k-w Turbulence Models For Aerodynamic Flows**. In: *American Institute of Aeronautics and Astronautics 23rd Fluid Dynamics, Plasmadynamics, and Lasers Conference; Orlando,FL,U.S.A*. American Institute of Aeronautics and Astronautics 1993.

92. Menter F: **Two-equation eddy-viscosity turbulence models for engineering applications**. *The American Institute of Aeronautics and Astronautics* 1994, **32**(8):1598-1605.

93. Alomair O, Jumaa M, Alkoriem A, Hamed M: **Heavy oil viscosity and density prediction at normal and elevated temperatures**. *Journal of Petroleum Exploration and Production Technology* 2016, **6**(2):253–263.

94. Ahrabi F, Ashcroft SJ, Shearn RB: **High pressure volumetric phase composition and viscosity data for a North Sea crude oil and NGL mixtures**. *Chem Eng Res* 1987, **67**:329– 334.

95. Miller K, Erno B: **Use the Misuse of hevy oil and Bituman Viscosity Data**. In: *46th Annual Technical Meating of the petroleum socity of CIM: May 14-17,1995; Banff, Alberta, Canada*. CIM 1995: 93-95.

96. Sattarin M, Modarresi H, Bayat M, Teymori M: **New Viscosity Correlations for Dead Crude Oils**. *Petroleum & Coal* 2007, **49**(2):33-39.

97. Lifesciences E: **EV1000 Clinical Platform NI**. In.; 2015.

98. Michael G, Al-Siri M, Khan ZH, Ali FA: **Differences in Average Chemical Structures of Asphaltene Fractions Separated from Feed and Product Oils of a Mild Thermal Processing Reaction**. *Energy & Fuels* 2005, **19**:1598-1605.

99. Lohrenz J, Bray BC, Clark CR: **Calculating viscosities of reservoir fluids from their composition**. *JPT* 1964, **10**:1170– 1176.

100. Little JE, Kennedy HT: **Calculating the viscosity of hydrocarbon systems with pressure temperature and composition.** *Soc Pet Eng J* 1968, **6**:157– 162.

101. Standing MB, Katz DL: **Density of Natural Gases** *Transactions of the AIME* 1942, **146**(1):140-149.

102. Standing MB: **Drilling and Production Practice**: API; 1957.

103. Peng DY, Robinson DB: **A new two-constant equation of state**. *Ind Eng Chem Fundam* 1976, **15**:59– 63.

104. Kesler MG, Lee BI: **Improve Prediction of Enthalpy of Fractions**. *Hydrocarbon Process* 1976, **55**(3):153–158.

105. Beggs HD, Robinson JR: **Estimating the viscosity of crude oil systems**. *JPT* 1975, **sept 1975**:1440.

106. Elsharkawy AM, Alikhan AA: **Model for predicting the viscosity of Middle East crude oils**. *Fuel* 1999, **78**:891-903.

107. Naseri A, Nikazar M, Mousavi-dehghani SA: **A correlation approach for prediction of crude oil viscosity**. *Journal of Petroleum Science and Engineering* 2005, **47**:163 - 174.

108. Beal C: **Viscosity of air, water, natural gas, crude oil and its associated gases at oil field temperature and pressures**. *Trans AIME* 1946, **165**(114– 127).

109. Kartoatmodjo T, Schmidt Z: **Large data bank improves crude physical property correlation**. *Oil and Gas Journal* 1994 **92**(27):51-55.

110. Labedi R: **Improved correlations for predicting the viscosity of light crudes**. *Journal of Petroleum Science and Engineering* 1992, **8**:221 - 234.

111. Hossain MS, Sarica C, Zhang HQ: **Assessment and Development of Heavy Oil Viscosity Correlations**. In: *International Thermal Operations and Heavy Oil Symposium; Calgary, Alberta, Canada*. Society of Petroleum Engineers 2005.

112. Standing MB: **A Pressure-Volume-Temperature Correlation for Mixtures of California Oils and Gases**. *Drilling and Production Practice* 1947:275-284.

113. Glaso O: **Generalized pressure–volume–temperature correlation for crude oil system**. *Journal of Petroleum Technology* 1980, **2**:785– 795.

114. Petrosky JGE, Farshad FF: **Viscosity Correlations for Gulf of Mexico Crude Oils**. In: *SPE Production Operations Symposium; Oklahoma City, Oklahoma*. Society of Petroleum Engineers 1995.

115. Chapman S, Gowling TG: **The Mathematical Theory of Nonuniform Gases: An Account of the Kinetic Theory of Viscosity, Thermal Conduction and Diffusion in Gases**, 3rd edn. Cambridge, U.K.: Cambridge University Press; 1970.

116. Riazi MR, Al-Sahhaf TA: **Physical properties of heavy petroleum fractions and crude oils**. *Fluid Phase Equilibria* 1996, **117**(1-2):217–224.

117. Reid RC, Prausnitz JM, Poling BE: **The properties of gases and liquids**, 4th ed edn: McGraw-Hill; 1987.

118. A MF: **conductive thermique des liquides organiques d'un serie ou d'un "groupe de liquides"** *Rev Gen Thermodyn* 1970, **101**(5):649-660.

119. Govender O: **A New Group Contribution Method for the Estimation of Thermal Conductivity of Non-Electrolyte Organic Compounds**. University of KwaZulu-Natal Durban; 2011.

120. Resende PR, Pinho FT, Cruz DO: **A Reynolds stress model for turbulent flows of viscoelastic fluids**. *Journal of Turbulence* 2013, **14**(12):1 - 36.

121. Smith CRR: **Optimization of Operating Conditions for Mitigating Fouling in Heat Exchanger Networks**. *Chemical Engineering Research and Design* 2007, **85**(6):839—851.

122. D. S, K. S, H. D, K. MO: **Mathematical modelling of asphaltenes deposition and removal in crude distilation units**. In: *Heat Exchanger fouling and cleaning VIII; Schadming, Austria*: Edited by H. M-s, Malayeri MR, Watkinson AP. 2009.

123. Crittenden BD, A. HS, J. AN: **Model Experiments of chemical reaction fouling**. *Chemical Engineering Research and Design* 1987, **65**:165-170.

124. **Information Center Alahmadi refinery** [https://www.kpc.com.kw/InformationCenter/Pages/Alahmadi-refinery.aspx]

125. A. A-ST, A. FM, S. EA: **Retardation of asphaltene precipitation by addition of toluene, resins, deasphalted oil and surfactants**. *Fluid Phase Equilibria* 2002, **194–197**:1045–1057.

Appendix A: Data Used for Properties Estimation

Table A.1 Samples used to estimate priorities in chapter 4

Sample ID	Molecular weight	density g/cm^3 @25C	Specific gravity @25C	API @25C
HAMMA 06	240	0.86	0.87	31.96
R 153	279	0.89	0.90	26.19
R 162 T	263	0.88	0.89	28.28
R 179 T	283	0.90	0.90	25.63
R 185 TS	262	0.90	0.90	25.79
R 187 TS	300	0.91	0.91	24.29
RA 181 T	297	0.91	0.91	23.61
S 144 TL	299	0.91	0.91	23.41
SA 102 T	293	0.94	0.94	19.33
SA 104 TS	303	0.93	0.93	20.93
SA 110TL	309	0.93	0.93	20.17
SA 120 TS	294	0.90	0.91	24.43
SA 133 TS	317	0.92	0.93	21.07
SA 145	248	0.87	0.87	30.24
SA 190 TS	304	0.92	0.92	22.25
SA 30 T	310	0.88	0.88	28.54
SA 89T	304	0.91	0.91	23.35
SN 1	361	0.97	0.97	14.58
SN 10	394	0.97	0.97	14.59
SN 11	343	0.94	0.95	17.81
SN 12	363	0.96	0.96	15.75
SN 13	343	0.95	0.96	16.50
SN 14	346	0.95	0.96	16.64
SN 15	370	0.96	0.96	15.79
SN 16	350	0.97	0.97	14.65
SN 17	334	0.94	0.94	18.49
SN 18	325	0.94	0.94	18.46
SN 19	367	0.96	0.96	16.19
SN 2	358	0.97	0.97	14.31
SN 20	333	0.95	0.95	17.44
SN 21	344	0.94	0.95	17.82
SN 22	383	0.98	0.98	13.19
SN 4	364	0.96	0.97	14.75
SN 5	372	0.96	0.97	14.76
SN 6	350	0.97	0.97	14.16
SN 8	328	0.96	0.96	15.65
SN 9	433	0.98	0.98	12.76

SP 804 B	359	0.95	0.95	17.24
SP 805	335	0.94	0.95	17.81
SP 806 B	357	0.95	0.95	16.87
SP 807 B	359	0.95	0.95	17.21
SP 809	335	0.94	0.95	17.81
SP 813 B	363	0.95	0.95	16.82
SP 814	341	0.95	0.95	17.46
UG 112	342	0.95	0.95	17.73
UG 117	326	0.93	0.94	19.76
UG 145	379	0.96	0.96	16.06
UG 186	328	0.93	0.94	19.42
UG 61	342	0.95	0.95	16.88

Table A.2 SARA analysis of samples used to estimate priorities in chapter 4

	Asphaltenes wt%	Polar resins wt%	Aromatics wt%	Saturates wt%
R 162 T	1.74	24.22	44.67	29.37
R 185 TS	8.27	27.51	22.42	41.80
R 187 TS	7.59	31.95	36.45	24.00
RA 181 T	6.67	28.09	46.77	18.46
S 144 TL	10.28	25.44	41.75	22.53
SA 102 T	8.06	35.23	39.05	17.67
SA 104 TS	11.28	27.94	43.86	16.92
SA 110TL	11.60	31.22	41.13	16.05
SA 120 TS	6.81	30.21	41.81	21.17
SA 133 TS	9.63	28.76	41.52	20.09
SA 145	4.84	27.90	32.20	35.06
SA 190 TS	10.19	33.84	11.84	44.13
SA 30 T	12.57	25.14	43.96	18.33
SA 89T	9.75	27.75	43.66	18.84
SN 1	12.89	20.03	54.58	12.50
SN 10	8.42	20.39	60.08	11.10
SN 11	11.22	18.54	58.67	11.57
SN 12	9.68	36.07	30.00	24.24
SN 13	6.81	26.52	51.44	15.23
SN 14	7.29	31.68	22.94	38.09
SN 15	12.72	31.51	39.65	16.11
SN 16	11.80	25.49	48.88	13.83
SN 17	8.12	35.38	30.71	25.79
SN 18	10.19	26.05	49.88	13.88
SN 19	10.31	21.99	54.96	12.74
SN 2	10.51	20.46	58.40	10.63

SN 22	11.11	19.60	58.14	11.16
SN 5	13.10	20.20	54.84	11.85
SN 6	10.78	21.96	56.62	10.64
SN 8	12.54	19.96	57.10	10.39
SN 9	6.10	32.89	47.97	13.04
SP 804 B	10.38	13.95	60.05	15.62
SP 805	19.81	21.41	45.16	13.61
SP 806 B	12.69	16.85	53.53	16.94
SP 807 B	12.30	16.95	55.10	15.65
SP 809	12.59	15.18	56.00	16.22
SP 813 B	13.49	13.75	57.63	15.13
SP 814	22.26	18.72	46.68	12.33
UG 112	25.49	21.27	41.03	12.21
UG 117	18.82	27.16	18.48	35.54
UG 145	24.74	27.14	35.73	12.39
UG 186	22.06	26.30	40.04	11.60
UG 61	23.56	20.36	26.27	29.82

Table A.3 Viscosity at different temperature temperature data

SP- 803		SN - 9		Hamma - 06	
T (°C)	Viscosity (cp)	T (°C)	Viscosity (cp)	T (°C)	Viscosity (cp)
21	*11136*	*21*	*2414*	*24*	*10*
26	*7020*	*30*	*1137*	*30*	*8*
30	*4660*	*40*	*508*	*40*	*6*
40	*1862*	*50*	*248*	*60*	*3*
50	*928*	*60*	*136*	*80*	*2*
60	*511*	*70*	*79*	*100*	*2*
70	*311*	*80*	*52*	*110*	1
80	*170*	*100*	*26*	*120*	*1*
100	*66*	*120*	*14*	*130*	1
121	*32*	*140*	*8*	*141*	*1*
140	*18*	*150*	*7*	*150*	*1*
159	*11*	*160*	*6*	*160*	*1*
SP- 814 C		SP- 820 C		SA - 30 T	
T (°C)	Viscosity (cp)	T (°C)	Viscosity (cp)	T (°C)	Viscosity (cp)
22	*4867*	*20*	*3164*	*23*	*83*
30	*2375*	*30*	*1218*	*31*	*48*
40	*1080*	*40*	*695*	*50*	*22*
50	*486*	*50*	*353*	*60*	*16*

60	*256*	*60*	*188*	*80*	*9*
70	*145*	*70*	*116*	*99*	*5*
80	*90*	*81*	*69*	*121*	*4*
101	*40*	*100*	*34*	*130*	*3*
120	*22*	*120*	*19*	*140*	*3*
141	*5*	*140*	*6*	*150*	*2*
157	*2*	*160*	*4*	*160*	*2*
SP- 815 C		SN - 6		R- 162 T	
T (°C)	Viscosity (cp)	T (°C)	Viscosity (cp)	T (°C)	Viscosity (cp)
20	*2722*	*30*	*495*	*23*	*22*
30	*1137*	*40*	*228*	*30*	*15*
40	*632*	*50*	*115*	*40*	*10*
50	*317*	*60*	*73*	*60*	*6*
60	*165*	*70*	*46*	*70*	*4*
70	*92*	*80*	*32*	*80*	*3*
80	*63*	*100*	*16*	*100*	*2*
90	*42*	*120*	*9*	*119*	*2*
100	*30*	*130*	*7*	*120*	2
120	*11*	*140*	*6*	*140*	*1*
143	*7*	*150*	*5*	*150*	*1*
155	*5*	*160*	*4*	*160*	*1*
SN - 2		SN - 10		R- 185 TS	
T (°C)	Viscosity (cp)	T (°C)	Viscosity (cp)	T (°C)	Viscosity (cp)
21	*1063*	*20*	*1609*	*23*	*34*
30	*504*	*30*	*650*	*30*	*25*
40	*262*	*40*	*315*	*40*	*15*
50	*142*	*50*	*175*	*50*	*10*
60	*79*	*60*	*101*	*70*	*6*
80	*34*	*70*	*58*	*80*	*5*
90	26	*80*	*38*	*90*	*4*
100	*17*	*100*	*21*	*100*	*3*
120	*6*	*120*	*11*	*120*	*2*
130	5	*130*	*9*	*130*	*2*
140	*4*	*140*	*7*	*140*	*1*
150	*3*	*150*	*6*	*150*	*1*
160	*3*	*160*	*5*	*160*	*1*
SN - 16		SN - 4		R- 153 T	
T (°C)	Viscosity (cp)	T (°C)	Viscosity (cp)	T (°C)	Viscosity (cp)

21	*1121*	*21*	*843*	*22*	*32*
30	*462*	*30*	*412*	*30*	*20*
40	*232*	*40*	*211*	*40*	*13*
50	*125*	*50*	*113*	*50*	*11*
60	*79*	*60*	*67*	*60*	*7*
70	*51*	*70*	*44*	*80*	*4*
80	*34*	*80*	*30*	*100*	*3*
100	*17*	*100*	*15*	*110*	2
120	*10*	*120*	*9*	*120*	*2*
130	8	*130*	7	*130*	2
140	*6*	*140*	*5*	*140*	*2*
150	5	*150*	5	*150*	*1*
160	*4*	*160*	*4*	*160*	*1*
SN - 5		SN - 8		R- 125 T	
T (°C)	Viscosity (cp)	T (°C)	Viscosity (cp)	T (°C)	Viscosity (cp)
23	*764*	*25*	*430*	*20*	---
30	*389*	*30*	*294*	*30*	*23*
40	*188*	*40*	*144*	*40*	*15*
50	*102*	*50*	*81*	*50*	*11*
60	*68*	*60*	*51*	*60*	*7*
70	*41*	*70*	*34*	*74*	*5*
80	*28*	*80*	*24*	*80*	*4*
100	*15*	*100*	*14*	*100*	*3*
120	*9*	*120*	*7*	*120*	*2*
130	*7*	*130*	*5*	*130*	2
140	*4*	*140*	*4*	*140*	*2*
150	*3*	150	3	*150*	2
160	*3*	*160*	*2*	*160*	*1*
SN - 12		SN - 15		R- 179 T	
T (°C)	Viscosity (cp)	T (°C)	Viscosity (cp)	T (°C)	Viscosity (cp)
20	*609*	*21*	*597*	*31*	*21*
30	*287*	*30*	*294*	*40*	*14*
40	*146*	*40*	*146*	*50*	*10*
50	*83*	*50*	*84*	*60*	*7*
60	*53*	*60*	*53*	*70*	*5*
70	*35*	*70*	*36*	*80*	*4*
80	*25*	*80*	*26*	*100*	*3*
100	*15*	*100*	*13*	*120*	*2*

120	*9*	*120*	*8*	*130*	*2*
140	*5*	*140*	*5*	*140*	*2*
151	*4*	150	4	*150*	*1*
160	*4*	*160*	*4*	*160*	*1*
UG - 145		SN - 7		SA - 120 TS	
T (°C)	Viscosity (cp)	T (°C)	Viscosity (cp)	T (°C)	Viscosity (cp)
20	*1504*	*21*	*509*	*27*	*37*
30	*609*	*31*	*253*	*30*	*31*
40	*286*	*40*	*144*	*50*	*13*
50	*150*	*50*	*82*	*59*	*10*
60	*93*	*60*	*52*	*70*	*9*
70	*57*	70	38	*80*	*6*
80	*39*	*80*	*25*	*100*	*4*
100	*20*	*100*	*14*	*110*	*3*
120	*12*	*120*	*4*	*122*	*3*
140	*8*	*140*	*2*	*130*	*2*
150	6	*150*	2	*139*	*2*
160	*5*	*160*	*2*	*159*	*2*
SN - 19		SN - 13		R- 187 TS	
T (°C)	Viscosity (cp)	T (°C)	Viscosity (cp)	T (°C)	Viscosity (cp)
21	*580*	*20*	*470*	*25*	*42*
30	*277*	*30*	*201*	*40*	*21*
40	*135*	*40*	*109*	*50*	*15*
50	*81*	*50*	*63*	*60*	*11*
60	*53*	*60*	*41*	*80*	*6*
70	*36*	*70*	*29*	*100*	*4*
80	*25*	*80*	*20*	*110*	*3*
100	*13*	*100*	*11*	*120*	*3*
120	*8*	*120*	*7*	*130*	2
140	*5*	*140*	*5*	*140*	*2*
150	5	*150*	*4*	*151*	*2*
158	*4*	*160*	*3*	*160*	*2*
SN - 14		SP- 813		SA - 89 TS	
T (°C)	Viscosity (cp)	T (°C)	Viscosity (cp)	T (°C)	Viscosity (cp)
25	*316*	*20*	*692*	*24*	*121*
30	*211*	*30*	*307*	*30*	*86*
40	*110*	*40*	*158*	*40*	*49*
50	*62*	*50*	*95*	*50*	*28*

60	*40*	*60*	*58*	*60*	*19*
70	*28*	*70*	*40*	*70*	*13*
80	*20*	*80*	*29*	*80*	*10*
100	*12*	*100*	*15*	*100*	*6*
110	10	*110*	12	*110*	*5*
120	*7*	*120*	*9*	*120*	*4*
140	*5*	*140*	*6*	*140*	*3*
150	4	*150*	5	*150*	*2*
160	*2*	*160*	*4*	*160*	*2*
SP- 809		SP- 808		S - 144 TL	
T (°C)	Viscosity (cp)	T (°C)	Viscosity (cp)	T (°C)	Viscosity (cp)
22	*571*	*24*	*453*	*25*	*66*
30	*316*	*30*	*281*	*30*	*43*
40	*155*	*40*	*139*	*40*	*24*
50	*92*	*50*	*83*	*50*	*17*
60	*55*	*60*	*51*	*60*	*12*
70	*37*	*70*	*34*	*70*	*9*
80	*26*	*80*	*24*	*80*	*7*
100	*14*	*100*	*13*	*101*	*4*
110	11	*110*	10	*120*	*3*
120	*9*	*120*	*7*	*130*	3
140	*6*	*140*	*5*	*143*	*2*
150	5	*150*	5	*150*	*2*
160	*4*	*160*	*4*	*160*	*2*
SP- 804		SP- 812		SA - 104 T	
T (°C)	Viscosity (cp)	T (°C)	Viscosity (cp)	T (°C)	Viscosity (cp)
20	*587*	*20*	*541*	*24*	*142*
30	*268*	*30*	*250*	*30*	*92*
40	*134*	*40*	*124*	*40*	*53*
50	*81*	*50*	*84*	*50*	*34*
60	*50*	*60*	*51*	*60*	*23*
70	*34*	*70*	*36*	*70*	*16*
80	*24*	*80*	*25*	*80*	*12*
100	*14*	*90*	*17*	*100*	*7*
120	*8*	*100*	*13*	*120*	*4*
140	*5*	*120*	*7*	*141*	*3*
150	5	*140*	*4*	*150*	3
159	*4*	*160*	*4*	*160*	*2*

SP- 807		SP- 806		SA - 133 TS	
T (°C)	Viscosity (cp)	T (°C)	Viscosity (cp)	T (°C)	Viscosity (cp)
20	*565*	*20*	*520*	*33*	*52*
30	*260*	*31*	*225*	*40*	*37*
40	*131*	*40*	*123*	*50*	*25*
50	*75*	*50*	*75*	*60*	*18*
60	*48*	*60*	*48*	*80*	*9*
80	*24*	*70*	*33*	*100*	*6*
100	*10*	*80*	*23*	*110*	*5*
121	*6*	*100*	*11*	*120*	*4*
130	*5*	*120*	*6*	*135*	*3*
140	*4*	*140*	*4*	*140*	*3*
150	3	*150*	3	*156*	*2*
160	*3*	*160*	*3*	*160*	*2*
SP- 814		SP- 805		SA - 131 TL	
T (°C)	Viscosity (cp)	T (°C)	Viscosity (cp)	T (°C)	Viscosity (cp)
21	*483*	*20*	*415*	*31*	*207*
30	*245*	*31*	*195*	*40*	*116*
40	*125*	*40*	*103*	*50*	*62*
50	*76*	*50*	*69*	*60*	*40*
60	*50*	*60*	*44*	*80*	*19*
70	*34*	*70*	*31*	*100*	*10*
80	*23*	*80*	*22*	*110*	9
100	*9*	*90*	*16*	*120*	*7*
125	*3*	*100*	*12*	*130*	*5*
130	*3*	*120*	*7*	*140*	*4*
140	*3*	*140*	*5*	*150*	*3*
160	*2*	*160*	---	*160*	*3*
SN - 11		SN - 21		SA - 110 TL	
T (°C)	Viscosity (cp)	T (°C)	Viscosity (cp)	T (°C)	Viscosity (cp)
25	*247*	*20*	*289*	*30*	*128*
30	*180*	*25*	*209*	*45*	*52*
41	*79*	*30*	*153*	*60*	*27*
50	*59*	*40*	*83*	*80*	*13*
60	*39*	*50*	*51*	90	11
70	*27*	*60*	*33*	*100*	*8*
80	*20*	*70*	*23*	*110*	*7*

100	*11*	*80*	*18*	*119*	*5*
120	*6*	*100*	*10*	*130*	5
140	*4*	*120*	*6*	*139*	*4*
151	*4*	*140*	*4*	*147*	*3*
160	*3*	*160*	*3*	*165*	*3*
SN - 20		SN - 17			
T (°C)	Viscosity (cp)	T (°C)	Viscosity (cp)		
20	*343*	*20*	*253*		
30	*168*	*30*	*130*		
40	*93*	*40*	*72*		
50	*54*	*50*	*44*		
60	*36*	*60*	*31*		
70	*25*	*70*	*21*		
80	*18*	*80*	*15*		
101	*10*	*100*	*7*		
123	*6*	*110*	*5*		
130	*5*	*121*	*4*		
140	*4*	*140*	*3*		
150	*4*	150	3		
160	*3*	*160*	*3*		

Appendix B: Models Derivation

B-1: momentum balance

$\vec{u} = u_r\hat{r} + u_\theta\hat{\theta} + u_z\hat{z}$

$assume: u_\theta = u_r = 0$

$\vec{u} = u_z\hat{z}$

$assume: axial, syemetery$

$\frac{\partial}{\partial\theta} = 0\ for, all$

$\nabla\vec{u} = \frac{1}{r}\frac{\partial ru_z}{\partial r}\hat{r}\hat{z} + \frac{\partial u_z}{\partial z}\hat{z}\hat{z}$

$\nabla.\vec{u} = \frac{\partial u_z}{\partial z}$

$$\tau^T = \begin{bmatrix} \tau_{rr}\hat{r}\hat{r} + \tau_{\theta r}\hat{\theta}\hat{r} + \tau_{zr}\hat{z}\hat{r} + \\ \tau_{r\theta}\hat{r}\hat{\theta} + \tau_{\theta\theta}\hat{\theta}\hat{\theta} + \tau_{z\theta}\hat{z}\hat{\theta} \\ +\tau_{rz}\hat{r}\hat{z} + \tau_{\theta z}\hat{\theta}\hat{z} + \tau_{zz}\hat{z}\hat{z} \end{bmatrix}, \because u_\theta = u_r = 0, \frac{\partial}{\partial\theta} = 0\ for, all\ \therefore \tau^T = \left[\tau_{rz}\hat{r}\hat{z} + \tau_{zz}\hat{z}\hat{z}\right]$$

$$\rho\frac{\partial\vec{u}}{\partial t} + \rho\left(\vec{u}.\nabla\right)\vec{u} = \nabla.\left[-p\tau + \left(\mu + \mu_T\right)\left(\nabla\vec{u}\right)^T - \frac{2}{3}\left(\mu + \mu_T\right)\left(\nabla.\vec{u}\right)\tau - \frac{2}{3}\rho k\tau\right] + F$$

$assume: F = 0$

$$\rho\frac{\partial u_z\hat{z}}{\partial t} + \rho\left(u_z\hat{z}.\frac{\partial}{\partial z}\hat{z}\right)u_z\hat{z} = \nabla.\begin{bmatrix} -p\left[\tau_{rz}\hat{r}\hat{z} + \tau_{zz}\hat{z}\hat{z}\right] + \left(\mu + \mu_T\right)\left(\frac{1}{r}\frac{\partial ru_z}{\partial r}\hat{r}\hat{z} + \frac{\partial u_z}{\partial z}\hat{z}\hat{z}\right)^T \\ -\frac{2}{3}\left(\mu + \mu_T\right)\left(\frac{\partial u_z}{\partial z}\right)\left[\tau_{rz}\hat{r}\hat{z} + \tau_{zz}\hat{z}\hat{z}\right] - \frac{2}{3}\rho k\left[\tau_{rz}\hat{r}\hat{z} + \tau_{zz}\hat{z}\hat{z}\right] \end{bmatrix}$$

$$\rho\frac{\partial u_z}{\partial t}\hat{z} + \rho u_z\frac{\partial u_z}{\partial z}\hat{z} = \nabla.\begin{bmatrix} -p\tau_{rz}\hat{r}\hat{z} - p\tau_{zz}\hat{z}\hat{z} + \frac{1}{r}\left(\mu + \mu_T\right)\frac{\partial ru_z}{\partial r}\hat{r}\hat{z} + \\ \left(\mu + \mu_T\right)\frac{\partial u_z}{\partial z}\hat{z}\hat{z} - \frac{2}{3}\left(\mu + \mu_T\right)\left(\frac{\partial u_z}{\partial z}\right)\tau_{rz}\hat{r}\hat{z} + \\ \frac{2}{3}\left(\mu + \mu_T\right)\left(\frac{\partial u_z}{\partial z}\right)\tau_{zz}\hat{z}\hat{z} - \frac{2}{3}\rho k\tau_{rz}\hat{r}\hat{z} + \frac{2}{3}\rho k\tau_{zz}\hat{z}\hat{z} \end{bmatrix}$$

$$\rho\frac{\partial u_z}{\partial t}+\rho u_z\frac{\partial u_z}{\partial z}=\left(\frac{1}{r}\frac{\partial}{\partial r}r\hat{r}+\frac{\partial}{\partial z}\hat{z}\right).\begin{bmatrix}-p\tau_{rz}\hat{r}-p\tau_{zz}\hat{z}+\frac{1}{r}(\mu+\mu_T)\frac{\partial ru_z}{\partial r}\hat{r}\\+(\mu+\mu_T)\frac{\partial u_z}{\partial z}\hat{z}-\frac{2}{3}(\mu+\mu_T)\left(\frac{\partial u_z}{\partial z}\right)\tau_{rz}\hat{r}\\+\frac{2}{3}(\mu+\mu_T)\left(\frac{\partial u_z}{\partial z}\right)\tau_{zz}\hat{z}-\frac{2}{3}\rho k\tau_{rz}\hat{r}+\frac{2}{3}\rho k\tau_{zz}\hat{z}\end{bmatrix}$$

$$\rho\frac{\partial u_z}{\partial t}+\rho u_z\frac{\partial u_z}{\partial z}=\begin{bmatrix}\frac{1}{r}\frac{\partial}{\partial r}(-rp\tau_{rz})-\frac{\partial}{\partial z}(p\tau_{zz})+\frac{1}{r}\frac{\partial}{\partial r}\left(r\frac{1}{r}(\mu+\mu_T)\frac{\partial ru_z}{\partial r}\right)\\+\frac{\partial}{\partial z}\left((\mu+\mu_T)\frac{\partial u_z}{\partial z}\right)-\frac{1}{r}\frac{\partial}{\partial r}\left(r\frac{2}{3}(\mu+\mu_T)\left(\frac{\partial u_z}{\partial z}\right)\tau_{rz}\right)\\+\frac{\partial}{\partial z}\left(\frac{2}{3}(\mu+\mu_T)\left(\frac{\partial u_z}{\partial z}\right)\tau_{zz}\right)-\frac{1}{r}\frac{\partial}{\partial r}\left(r\frac{2}{3}\rho k\tau_{rz}\right)+\frac{\partial}{\partial z}\left(\frac{2}{3}\rho k\tau_{zz}\right)\end{bmatrix}$$

$$\tau_{rz}=-\mu\frac{\partial u_z}{\partial r},\tau_{zz}=-\mu\left[2\frac{\partial uz}{\partial z}\right]+\left(\frac{2}{3}\mu-\mu_T\right)\left(\frac{\partial u_z}{\partial z}\right)$$

$$\frac{\partial\rho}{\partial t}+\nabla.(\rho\vec{u})=0$$

$$\frac{\partial\rho}{\partial t}+\frac{\partial\rho u_z}{\partial z}=0$$

$$\rho\frac{\partial k}{\partial t}+\rho(\vec{u}.\nabla)k=\nabla.\left[(\mu+\mu_T\sigma_k)\nabla k\right]+P-\beta_0^*\rho\omega k$$

$$\rho\frac{\partial k}{\partial t}+\rho u_z\frac{\partial k}{\partial z}=\nabla.\left[(\mu+\mu_T\sigma_k)\frac{1}{r}\frac{\partial rk}{\partial r}\hat{r}+(\mu+\mu_T\sigma_k)\frac{\partial k}{\partial z}\hat{z}\right]+P-\beta_0^*\rho\omega k$$

$$\rho\frac{\partial k}{\partial t}+\rho u_z\frac{\partial k}{\partial z}=\frac{1}{r}\frac{\partial}{\partial r}\left(r(\mu+\mu_T\sigma_k)\frac{1}{r}\frac{\partial rk}{\partial r}\right)+\frac{\partial}{\partial z}\left((\mu+\mu_T\sigma_k)\frac{\partial k}{\partial z}\right)+P-\beta_0^*\rho\omega k$$

$$\rho\frac{\partial\omega}{\partial t}+\rho(\vec{u}.\nabla)\omega=\nabla.\left[(\mu+\mu_T\sigma_\omega)\nabla\omega\right]+\frac{\gamma}{\mu_T}\rho P-\beta\rho\omega^2+2(1-f_{v1})\frac{\sigma_{\omega2}\rho}{\omega}\nabla k.\nabla\omega$$

$$\rho\frac{\partial\omega}{\partial t}+\rho u_z\frac{\partial\omega}{\partial z}=\begin{bmatrix}\nabla.\left[(\mu+\mu_T\sigma_\omega)\frac{1}{r}\frac{\partial r\omega}{\partial r}\hat{r}+(\mu+\mu_T\sigma_\omega)\frac{\partial\omega}{\partial z}\hat{z}\right]+\frac{\gamma}{\mu_T}\rho P-\\\beta\rho\omega^2+2(1-f_{v1})\frac{\sigma_{\omega2}\rho}{\omega}\left(\frac{1}{r}\frac{\partial rk}{\partial r}\hat{r}+\frac{\partial k}{\partial z}\hat{z}\right).\left(\frac{1}{r}\frac{\partial r\omega}{\partial r}\hat{r}+\frac{\partial\omega}{\partial z}\hat{z}\right)\end{bmatrix}$$

$$\rho\frac{\partial\omega}{\partial t}+\rho u_z\frac{\partial\omega}{\partial z}=\begin{bmatrix}\frac{1}{r}\frac{\partial}{\partial r}\left(r\left(\mu+\mu_T\sigma_\omega\right)\frac{1}{r}\frac{\partial r\omega}{\partial r}\right)\\+\frac{\partial}{\partial z}\left(\left(\mu+\mu_T\sigma_\omega\right)\frac{\partial\omega}{\partial z}\right)\end{bmatrix}+\frac{\gamma}{\mu_T}\rho P-\beta\rho\omega^2+2\left(1-f_{v1}\right)\frac{\sigma_{\omega2}\rho}{\omega}\left(\frac{1}{r^2}\frac{\partial rk}{\partial r}\frac{\partial r\omega}{\partial r}+\frac{\partial k}{\partial z}\frac{\partial\omega}{\partial z}\right)$$

$$\nabla G.\nabla G+\sigma_\omega G\left(\nabla.\nabla G\right)=\left(1+2\sigma_\omega\right)G^4$$

$$\left(\frac{1}{r}\frac{\partial rG}{\partial r}\hat{r}+\frac{\partial G}{\partial z}\hat{z}\right).\left(\frac{1}{r}\frac{\partial rG}{\partial r}\hat{r}+\frac{\partial G}{\partial z}\hat{z}\right)+\sigma_\omega G\left(\nabla.\left(\frac{1}{r}\frac{\partial rG}{\partial r}\hat{r}+\frac{\partial G}{\partial z}\hat{z}\right)\right)=\left(1+2\sigma_\omega\right)G^4$$

$$\left(\frac{1}{r}\frac{\partial rG}{\partial r}\right)^2+\left(\frac{\partial G}{\partial z}\right)^2+\sigma_\omega G\left(\frac{1}{r}\frac{\partial}{\partial r}\left(r\frac{1}{r}\frac{\partial rG}{\partial r}\right)+\frac{\partial}{\partial z}\left(\frac{\partial G}{\partial z}\right)\right)=\left(1+2\sigma_\omega\right)G^4$$

$$\left(\frac{1}{r}\frac{\partial rG}{\partial r}\right)^2+\left(\frac{\partial G}{\partial z}\right)^2+\sigma_\omega G\frac{1}{r}\frac{\partial^2 rG}{\partial r^2}+\frac{\partial^2 G}{\partial z^2}=\left(1+2\sigma_\omega\right)G^4$$

$$I_\omega=\frac{1}{G}-\frac{I_{ref}}{2}$$

$$\mu_T=\rho\frac{k}{\omega}$$

$$P=\min\left(P_k,10\beta_0^*\rho\omega k\right)$$

$$P_k=\mu_T\left[\left[\frac{1}{r}\frac{\partial ru_z}{\partial r}\hat{r}\hat{z}+\frac{\partial u_z}{\partial z}\hat{z}\hat{z}\right]:2\left(\frac{1}{r}\frac{\partial ru_z}{\partial r}\hat{r}\hat{z}+\frac{\partial u_z}{\partial z}\hat{z}\hat{z}\right)-\frac{2}{3}\frac{\partial u_z}{\partial z}\right]-\frac{2}{3}\rho k\frac{\partial u_z}{\partial z}$$

$$\phi=f_{v1}\phi_1+\left(1-f_{v1}\right)\phi_2:\phi=\beta,\gamma,\sigma_k,\sigma_\omega$$

B-2: Energy balance

$$\nabla T=\frac{1}{r}\frac{\partial rT}{\partial r}\hat{r}+\frac{\partial T}{\partial z}\hat{z}$$

$$\rho C_p\frac{\partial T}{\partial t}+\rho C_p\vec{u}.\nabla T=\nabla.\left(k\nabla T\right)+Q+Q_{vh}+W_p$$

$$\rho C_p\frac{\partial T}{\partial t}+\rho C_p\vec{u}.\left(\frac{1}{r}\frac{\partial rT}{\partial r}\hat{r}+\frac{\partial T}{\partial z}\hat{z}\right)=\nabla.\left(\frac{1}{r}k\frac{\partial rT}{\partial r}\hat{r}+k\frac{\partial T}{\partial z}\hat{z}\right)+Q+Q_{vh}+W_p$$

$$\rho C_p\frac{\partial T}{\partial t}+\rho C_p u_z\frac{\partial T}{\partial z}=\frac{1}{r}\frac{\partial}{\partial r}\left(k\frac{\partial rT}{\partial r}\right)+\frac{\partial}{\partial z}\left(k\frac{\partial T}{\partial z}\right)+Q+Q_{vh}+W$$

$$\rho\frac{\partial\omega_a}{\partial t}+\nabla.\vec{j}_a+\rho\left(\vec{u}.\nabla\right)\omega_a=R_a$$

B-3 Mass Balance

$$\vec{N}_a = \vec{j}_a + \rho \vec{u} \omega_a$$

$$\vec{j}_a = -\left(\rho D_a^f \left(\frac{1}{r} \frac{\partial r \omega_a}{\partial r} \hat{r} + \frac{\partial \omega_a}{\partial z} \hat{z} \right) + \rho \omega_a D_a^f \frac{\frac{1}{r} \frac{\partial r M_n}{\partial r} \hat{r} + \frac{\partial M_n}{\partial z} \hat{z}}{M_n} + D_a^T \frac{\frac{1}{r} \frac{\partial r T}{\partial r} \hat{r} + \frac{\partial T}{\partial z} \hat{z}}{T} \right)$$

$$M_n - \left(\sum_i \frac{\omega_i}{M_i} \right)^{-1}$$

$$assume: M_n = const, D_a^T = 0$$

$$\vec{j}_a = -\rho D_a^f \frac{1}{r} \frac{\partial r \omega_a}{\partial r} \hat{r} - \rho D_a^f \frac{\partial \omega_a}{\partial z} \hat{z}$$

$$\rho \frac{\partial \omega_a}{\partial t} + \nabla . \left(-\rho D_a^f \frac{1}{r} \frac{\partial r \omega_a}{\partial r} \hat{r} - \rho D_a^f \frac{\partial \omega_a}{\partial z} \hat{z} \right) + \rho \left(\vec{u} . \nabla \right) \omega_a = R_a$$

$$\rho \frac{\partial \omega_a}{\partial t} + \frac{1}{r} \frac{\partial}{\partial r} \left(-\rho D_a^f \frac{\partial r \omega_a}{\partial r} \right) + \frac{\partial}{\partial z} \left(-\rho D_a^f \frac{\partial \omega_a}{\partial z} \right) + \rho u_z \frac{\partial \omega_a}{\partial z} = R_a$$